POLITECNICO
MILANO 1863

SCUOLA DI INGEGNERIA INDUSTRIALE
E DELL'INFORMAZIONE

PEMFC catalyst layer degradation - an experimental study of voltage limits effect in realistic cycling to develop a platinum dissolution model

TESI DI LAUREA MAGISTRALE IN
ENERGY ENGINEERING
INGEGNERIA ENERGETICA

Author: **Chiara Artini**

Student ID: 10746863
Advisor: Prof. Andrea Baricci
Co-advisor: Dr. Elena Colombo, Prof. Andrea Casalegno
Academic Year: 2020-21

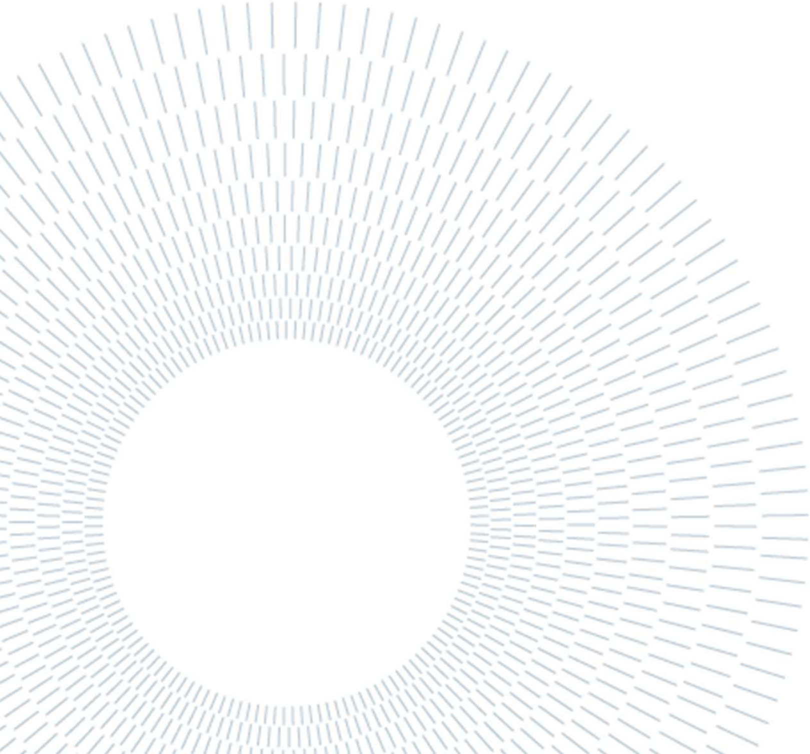

Abstract

Polymer Electrolyte Membrane Fuel Cells (PEMFCs) are a promising technology to decarbonize the automotive sector, thanks to their zero CO2 emissions. Nonetheless, they still present important durability issues. The catalyst layer is one of the most critical components for lifetime, where platinum dissolution is a relevant mechanism that implies the loss of catalyst active area (ECSA) under operation.

The goal of this work is to investigate catalyst degradation during voltage cycling, particularly focusing on the effect of different potential values and profiles. To this aim, a zero-dimensional physics-based platinum dissolution model was developed, including platinum oxidation, anodic dissolution, oxide chemical dissolution and platinum loss into the membrane. Model predictions were compared with experimental results to provide insight into the degradation process and improve model formulation.

An experimental analysis was made, performing several Accelerated Stress Tests (ASTs) in hydrogen/air with different voltage profiles, under conditions that mimic realistic automotive dynamic power operation, including also short stops when no power is produced and a system shut down is performed. It emerged that a square wave potential profile ranging between 0.7 V and 0.85 V has a low impact on degradation, resulting in a 17% ECSA loss in 1500 equivalent operating hours. Lower minimum potential values leaded to a stronger degradation, which was not investigated in the literature before. The strongest degradation was observed when alternating a square wave potential profile ranging between 0.7 V and 0.85 V with periodic potential reductions to nearly 0 V, resembling the short stop. This leaded to a 35% ECSA loss after 900 equivalent operating hours. The current trends detected during the ageing tests suggested the presence of an oxide which needs very low voltage to be reduced (< 0.4 V).

The model in its first version was not able to reproduce experimental results. Therefore, it was further developed by adding the place exchange reaction (a further form of oxidation, that leads to more stable species) and cathodic dissolution (i.e. transient dissolution of platinum from an oxide under a cathodic scan), the role of which is still not clarified in literature. These mechanisms can indeed provide a better explanation of experimental results. Parameters were calibrated by means of a sensitivity analysis. Simulations performed with the newly developed model show a better agreement with the experimental results, suggesting the key role played by these phenomena in realistic operations.

Key-words: Polymer electrolyte membrane fuel cell, catalyst degradation, Platinum oxidation and dissolution, modeling

Sommario

Le celle a combustibile a membrana polimerica (note con l'acronimo inglese PEMFCs) possono giocare un ruolo importante nella decarbonizzazione del settore automobilistico. La loro diffusione è però ancora limitata a causa dell'elevato costo specifico e della limitata vita utile, dovuta alla degradazione dei componenti. Tra questi uno dei più critici è il catalyst layer. La dissoluzione del platino che avviene in esso durante il funzionamento della cella porta infatti a una perdita di area attiva (ECSA) del catalizzatore, e a una diminuzione delle performance della cella.

L'obiettivo di questo lavoro è approfondire il degrado del catalyst layer dovuto alle variazioni del potenziale, con particolare attenzione all'effetto dei valori limite adottati. A questo scopo è stato sviluppato un modello zero-dimensionale, che descrive la dissoluzione del platino attraverso i seguenti meccanismi: ossidazione, dissoluzione anodica, dissoluzione chimica dell'ossido e flusso di platino in membrana.

Inoltre è stata fatta un'analisi sperimentale, eseguendo test di degrado accelerati basati su diversi profili di potenziale che simulano condizioni operative reali. È emerso che utilizzando un'onda quadra tra 0.7 V e 0.85 V la perdita di ECSA è molto limitata (17% in 1500 ore di funzionamento equivalenti). Una diminuzione del potenziale minimo ha portato a una degradazione più spinta. La perdita più importante (35% dopo 900 ore di funzionamento equivalenti) è stata osservata alternando all'onda quadra periodiche diminuzioni del potenziale a 0 V, che riproducono brevi interruzioni del funzionamento della cella, durante le quali non viene prodotta corrente. I profili di corrente rilevati durante i test suggeriscono la presenza di un ossido che si riduce solo con valori di potenziale molto bassi (< 0.4 V).

La prima versione del modello non riusciva a riprodurre i risultati sperimentali. Sono state quindi aggiunte due reazioni, il cui ruolo è ancora dibattuto in letteratura: il place exchange (un'ulteriore reazione di ossidazione, che porta alla formazione di un ossido più resistente) e la dissoluzione catodica (associata alla dissoluzione dell'ossido durante rampe di potenziali decrescenti). Questi meccanismi possono fornire una migliore spiegazione dei risultati sperimentali ottenuti. I parametri sono stati calibrati con un'analisi di sensibilità. Le simulazioni fatte con il modello aggiornato mostrano un maggiore accordo con i dati sperimentali. Questo suggerisce che le due reazioni introdotte abbiano un ruolo importante nel degrado che avviene durante il funzionamento reale.

Parole chiave: Celle a combustibile a membrana polimerica, degradazione del catalizzatore, dissoluzione ed ossidazione del platino, modeling

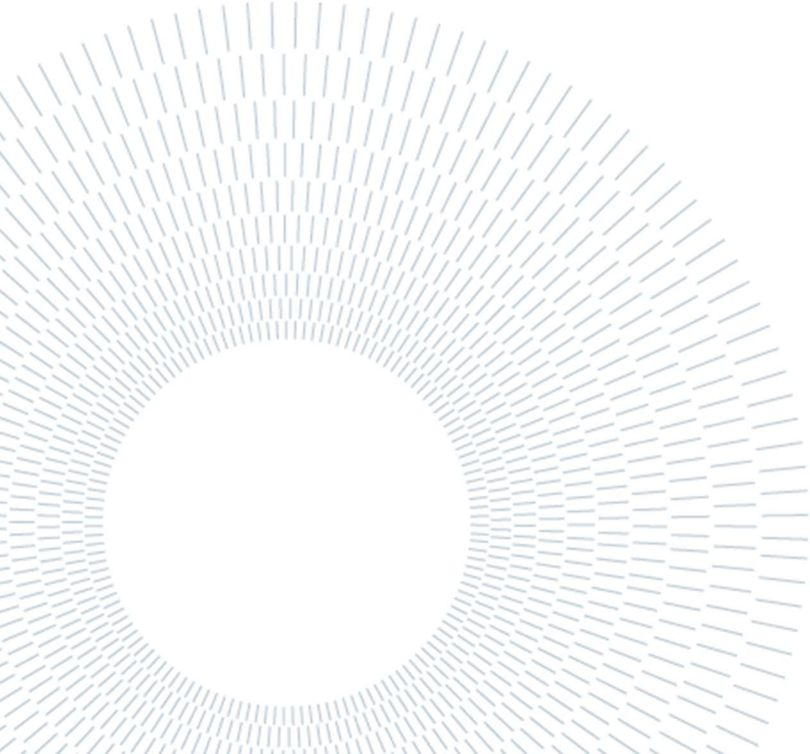

Contents

Introduction

Fuel cells are electrochemical devices which aim to exploit the chemical energy of the hydrogen oxidation by converting it directly into electrical energy, giving water as the only product. Thanks to their zero CO2 emissions, they are a promising technology to decarbonize the automotive sector. Nonetheless, they still present important costs and durability issues, due to the expenditure and to the rapid ageing of some components. Among the components, the Catalyst Layer (CL), together with the membrane, is the most critical one. It is composed of platinum nanoparticles, a carbon porous structure and ionomer. In normal PEMFCs operating conditions platinum shows an electrochemical unstable behaviour and can dissolve in the ionomer. Different reactions take place, leading to a reduction of the ElectroChemically active Surface Area (ECSA). This topic was addressed in the literature both with experimental studies and with the development of platinum dissolution model, aimed at achieving a deeper comprehension of the physics of this phenomenon and eventually find some strategies to counteract it.

The goal of this work is to investigate CL degradation due to platinum dissolution during voltage cycling, particularly focusing on the effect of different potential values and profiles. To this aim, a simple physics-based platinum dissolution model was developed, and an experimental analysis was made, performing different Accelerated Stress Tests (ASTs). The model was then used to simulate the ASTs, and model predictions were compared with experimental results to provide insight into the degradation process and improve model formulation.

Here is a list of the chapters with a short description of their content:

- **Chapter 1: State of the art: PEMFC technology and durability issues due to Platinum dissolution**
  PEMFC technology is introduced, with a brief description of its working principle and components. Platinum dissolution is also introduced, referring to the different mechanisms involved in it and models available in the literature. Finally, an overview of different platinum dissolution model is given.
- **Chapter 2: Experimental**
  The experimental methodology is presented: the experimental set-up, the basic plant layout and the experimental protocols are described.

- **Chapter 3**: **Platinum dissolution model**
  The developed model is presented, referring to the main hypothesis, the described reactions and the equations. The model in its first version is mainly taken from the literature. Main parameters are calibrated on experimental data.
- **Chapter 4: Experimental results**
  The AST design is described and the experimental results are presented. The starting point for the design of ageing protocols is the low power AST, designed in the frame of the European H2020 ID-FAST project [1], which aims at reproducing the degradation of realistic automotive low power operation. Starting from this standard protocol, several degradation tests have been designed and performed to investigate platinum dissolution mechanisms.
  Some attempts were made to reproduce experimental data with the model, but the simulated results did not match with experimental ones, suggesting the need for a more complex model.
- **Chapter 5: Model: a further development**
  A further developed model version is presented, obtained by adding some more reactions. A better reproduction of experimental results was obtained, and this also leaded to an insight on the dissolution process in real world operation.

1 State of the art: PEMFC technology and durability issues due to Platinum dissolution

In this chapter an overview on PEMFC technology will be firstly presented. Secondly, the specific topic of this work, namely platinum dissolution in the cathode catalyst layer, will be described, also giving an overview on models which have been proposed in the literature to describe this phenomenon.

1.1. PEMFC technology

1.1.1. PEMFC working principle

Fuel cells are electrochemical devices which aim to exploit the chemical energy of the hydrogen oxidation by converting it directly into electrical energy, giving water as the only product.

The oxidation of hydrogen (reaction (1)) produces indeed a great amount of energy, having a lower heating value of 119.96 MJ/kg.

$$H_2 + \frac{1}{2}O_2 \rightarrow H_2O \qquad LHV_{H_2} = 119.96\ \frac{MJ}{kg} \tag{1}$$

When hydrogen and oxygen are in contact, a combustion reaction takes place, converting the whole amount of chemical energy into heat.

In a fuel cell there is no direct contact between the two gases, and the reaction energy is mostly converted into electrical energy.

The schematic of a fuel cell is shown in Figure 1. Hydrogen and oxygen are separately fed respectively at the anode and at the cathode, creating a potential difference between the two electrodes.

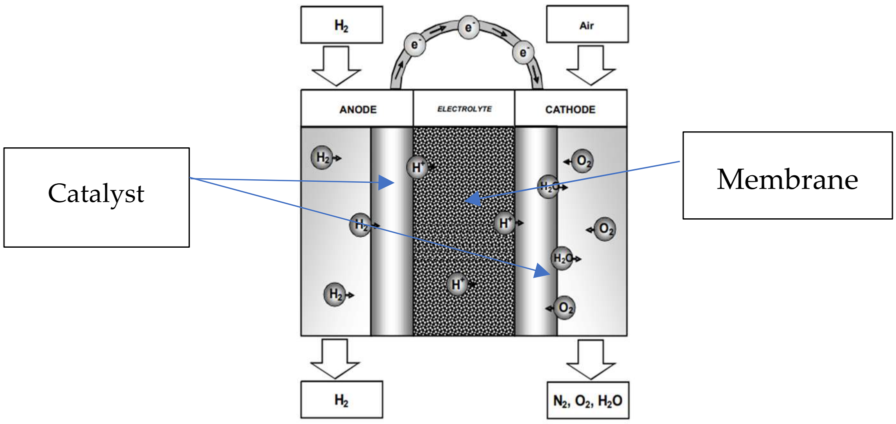

Figure 1 - PEMFC schematic

When the electrodes are electrically connected, the hydrogen is ionized according to reaction (2) (called Hydrogen Oxidation Reaction, HOR), protons migrate through the polymeric membrane towards the cathode, while electrons spontaneously flow in an external circuit thanks to the potential difference, creating a current. At the cathode oxygen eventually reacts with protons and electrons producing water. This second reaction (equation (3)) is called Oxygen Reduction Reaction (ORR). The sum of HOR and ORR results in Hydrogen oxidation (reaction (1)).

$$\frac{1}{2}H_2 \rightarrow H^+ + e^- \tag{2}$$

$$2H^+ + \frac{1}{2}O_2 + 2e^- \rightarrow H_2O \tag{3}$$

PEMFCs are characterized by a low operating temperature (about 70/80°C). A catalyst is thus necessary (typically platinum) to make the HOR and ORR reactions take place with a relevant reaction rate.

1.1.2. PEMFC components

The structure of a single fuel cell is shown in Figure 2. In real applications many cells are used together, forming a stack, but the main components are the same. The cell is composed of:

- A polymeric membrane, which allows the selective passage of protons and physically separates the anode and the cathode. It has to be proton conductive, impermeable to hydrogen and oxygen, and electrically insulant. The used material is Nafion, an acidic polymer whose proton conductivity strongly depends on the hydration level. Humidity control is therefore essential to ensure a proper operation of the system.

Although the membrane should totally hinder the gas passage, in real operation little amounts of hydrogen can cross the membrane, reacting directly with oxygen in gaseous phase at the cathode. This hydrogen crossover must be avoided as much as possible, as it represents a loss.

- Two catalyst layers, where HOR and ORR take place. They have to provide a high active area of the catalyst and allow the gases to flow towards the Pt active sites, the protons through the membrane, and the electrons back to the current collectors. To fulfil all these functions a three-phase structure is needed. The catalyst layers are thus composed by Platinum nanoparticles, that ensure a high specific area, a carbon porous structure, which allows the flow of gases and the conduction of electrons, and ionomer (the membrane material), which allows the flow of protons. This structure is known as triple phase boundary.
- Two Gas Diffusion Layers (GDLs), which allow the reactants to spread homogeneously and let the electrons flow towards the current collector. They are realized with a porous carbon structure.
- Two flow fields, which provide mechanical stability to the structure and supply gases to the system through some channels. They have to be mechanically resistant and electrically conductive, therefore they are typically made with graphite.
- Two current collectors, which are typically metallic.

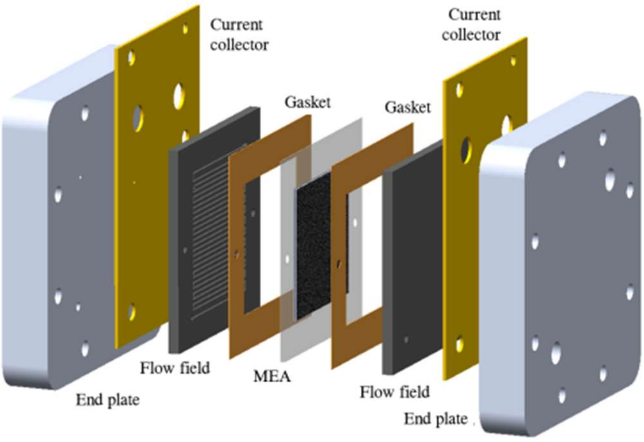

Figure 2 - Single cell structure

1.1.3. PEMFC issues

PEMFCs have shown important improvements in recent years. The most interest application for this technology is the automotive one, and some Fuel cell vehicle models are already available in the market, as *Toyota Mirai* (2015), *Honda Clarity* (2016), *Hyundai Nexo* (2018), while other models will be soon available, as *BMW X5 i Hydrogen Next* and the minivan *Citroen e-Jumpy Hydrogen*. Nonetheless the technology is still not sustainable from an economic point of view and suffers from durability problems.

According to the US Department of Energy (DOE) Hydrogen Program Record [2], the 2020 estimated cost of an 80-kWnet automotive PEMFC system is projected to be $76/kWnet when manufactured at a volume of 100,000 units/year. This cost represents the power system cost to achieve 8,000 hours of on-road operation (the so-called durability adjusted cost). The ultimate target of US Department Of Energy (DOE) to make the technology able to compete with internal combustion engine vehicles is fixed to $30/kWnet, considering the same durability (with a loss of less than 10% of nominal power) and the same volume of manufactured vehicles per year.

The polymeric membrane and the catalyst layer are the most critical components of PEMFC both in term of cost and durability. Further research is thus needed to increase the durability of this components.

To reduce the cost of the catalyst layer, the Platinum Loading (the mass of platinum for unit of electrode area, measured in $\frac{g_{Pt}}{cm_{el}^2}$) must be reduced, keeping constant the specific active area (platinum active area for unit of electrode area, $\frac{cm_{Pt}^2}{cm_{el}^2}$). To achieve that, platinum particles with smaller radius can be used, providing the same specific active area with a lower platinum loading (as the area-to-volume ratio is inversely proportional to the radius) and therefore with lower costs. Nonetheless, smaller platinum particles are more prone to dissolution, as will be explained later, which imposes a lower limit to their dimensions.

In order to overcome the cost and durability issues it is essential to achieve a deeper comprehension of the catalyst layer degradation mechanisms, which would eventually allow to find some strategies to counteract them.

1.2. Platinum dissolution and catalyst active area loss

As previously said, the catalyst is essential for PEMFC operation, as it allows reactions to take place with relevant reaction rates at low temperatures, but it is also really expensive and subject to degradation.

To optimize its utilization, it is essential to maximize the specific surface area, while to reduce its cost it is important to reduce the mass of platinum as much as possible. To achieve that, the catalyst is dispersed as nanoparticles on a carbon structure. The lower is the radius of nanoparticles, the higher is the specific surface area (active area of platinum per unit area of electrode) with the same platinum loading. Nonetheless, smaller particles are more prone to degradation, which leads to an optimal mean diameter of nanoparticles which at state of art is about 5 nm. If the particles were smaller, they would degrade too fast, leading to a rapid performance decay of the fuel cell. Pt particles radius varies in a range, forming a Particle Radius Distribution (PRD), which is usually described with a log-normal distribution, as shown in Figure 3.

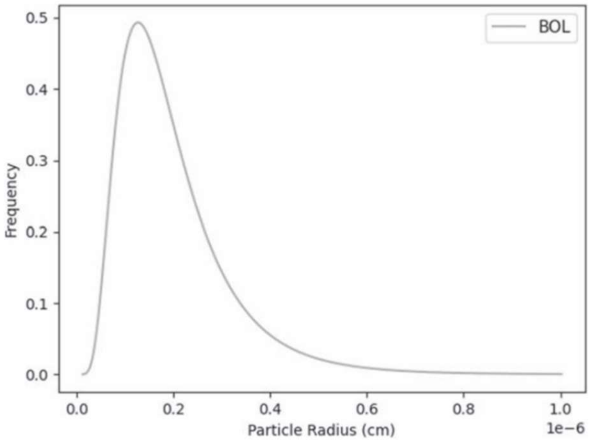

Figure 3 – Example of Particle Radius Distribution [3]

An important quantity to describe CCL degradation and performance decay is the Electrochemically active Surface Area (ECSA) which is the active platinum surface per mass unit and is measured in $\frac{cm_{Pt}^2}{g_{Pt}}$. If the Pt loading is kept constant, a higher ECSA corresponds to a higher active platinum surface per unit of electrode area. From now on we will quantify the loss of active area in term of ECSA loss.

The catalyst is present both at the anode and at the cathode but the ORR (which takes place at the cathode) is much more sluggish with respect to the HOR (which takes place at the anode). For this reason, the platinum loading at the cathode is always higher than the one at the anode. Typical values are 0.5/0.4 $\frac{mg_{Pt}}{cm_{el}^2}$ at the cathode and 0.1 $\frac{mg_{Pt}}{cm_{el}^2}$ at the anode. Furthermore, inside the cell the potential is not uniform, reaching its maximum value at the cathode, which exposes the CCL (Cathode Catalyst Layer) to a more aggressive environment with respect to the ACL (Anode Catalyst layer). This work will focus therefore on the CCL degradation, as all the literature does.

Platinum dissolution is mainly a transient phenomenon, resulting from the equilibrium of different reactions which take place simultaneously. Its driving force is the potential. When the potential is increased Pt dissolves in the electrolyte but at the same time it is oxidized, which rapidly limits dissolution. When the potential is decreased, Pt oxides are reduced and platinum redeposition is enhanced. Moreover, an increase of Pt concentration is experimentally observed [4][5] during decreasing potential sweep. This is associated to the dissolution of Pt oxides directly in the electrolyte. The reaction which causes this dissolution, as well as its impact on degradation, is still debated in literature. The reactions involved in platinum dissolution are described in detail in the following.

1.2.1. Reactions and mechanisms

During their functioning in vehicles, PEMFCs must be able to withstand changing load conditions, which correspond to different voltages. In normal operating conditions the voltage should range between 0.6 V and 0.95 V, while during start-up and shut down it can temporarily rise above 1.2 V.

In this potential range platinum shows an electrochemically unstable behaviour, which results in a sum of reactions which lead to the so-called platinum dissolution.

Different reactions and mechanisms have been suggested to describe this complex phenomenon, part of them being commonly accepted by most of the authors, others being proposed only by some authors, and modelled with different formulations.

Anyway, some major reactions and mechanisms can be outlined.

Platinum oxidation

The oxidation of Pt is commonly assumed to follow reaction (4) [6][7]. The driving force of this reaction is the potential, and the direction in which the reaction takes place depends on the difference between the applied potential and the respective equilibrium potential $\boldsymbol{\Phi_{ox}}$ of the reaction. When the potential goes toward the equilibrium potential platinum oxidizes, when the potential decreases again below this value the platinum oxide is reduced. The actual equilibrium potential is lower than the reference one (which refers to bulk Platinum) as it depends on the radius of nanoparticles. The lower is the radius, the lower is the equilibrium potential, the higher will be the oxidation rate. This also means that particles with different radius will have different oxidation state at the same time.

$$Pt + H_2O \rightleftarrows PtO + 2H^+ + 2e^- \quad [\Phi_{ox,ref} = 0.97V] \tag{4}$$

Some authors propose more complex mechanisms with an intermediate oxide, as shown in reactions (5), (6) and (7). [8].

$$Pt + H_2O \rightarrow PtOH + H^+ + e^- \tag{5}$$

$$PtOH \rightarrow PtO + H^+ + e^- \tag{6}$$

$$PtO + 2H^+ \rightarrow Pt + H_2O \tag{7}$$

Surface oxidation prevents platinum from dissolution but also hinders the catalysation of reactions by lowering temporarily the catalyst active area. A partial oxidation can therefore protect from dissolution, but too high value of oxide coverage (i.e. oxidized platinum area divided by the total area) will limit the ability of the catalyst to perform his function and finally the capability of the fuel cell to produce a current and power a load.

Platinum anodic dissolution

Given the acidic environment and the voltage variations, platinum can dissolve in the electrolyte (i.e. the ionomer), which is part of the catalyst layer. The so called "anodic dissolution" follows reaction 8.

$$Pt \rightleftarrows Pt^{2+} + 2e^- \qquad [\Phi_{Adiss}^{ref} = 1.188\,V] \tag{8}$$

The term anodic dissolution, is used to distinguish it from the cathodic one, described later. This type of dissolution is generally considered indeed to be more relevant during anodic potential sweeps (increasing potentials).

Similarly to the oxidation, the reaction rate and its direction are function of the difference between the potential and the reference potential $\boldsymbol{\Phi_{Adiss}}$ **,** which depends on $\boldsymbol{\Phi_{Adiss,ref}}$ and on the particle radius, decreasing for smaller particles. Consequently, particles with different radius will show different dissolution rates, smaller particles will be more prone to dissolution, while platinum will redeposit mainly on bigger particles. In some conditions it is possible that dissolution of smaller particles and redeposition on bigger particles take place simultaneously.

Both dissolution and reprecipitation are hindered by the presence of oxides, which cover the platinum surface. When the potential is increased and kept constant to a certain value, anodic dissolution is enhanced, but the platinum rapidly oxidizes, limiting the dissolution. When the potential is decreased, Pt oxides are reduced, and dissolved Pt can redeposit. Therefore, anodic dissolution is mainly relevant during potential sweeps, when the Pt surface is still not oxidized.

Ostwald ripening and ECSA loss

During operation, the voltage will often increase and decrease, leading to a continue Pt dissolution and redeposition. As previously said, particles with smaller radius are more prone to dissolution, while Pt redeposition happens mainly on bigger particles.

As a result, smaller particles will become smaller and smaller and eventually disappear, while bigger particles will grow, leading to an increase of the mean particle radius, a reduction of ECSA (inversely proportional to the radius) and a decay of performances. This mechanism is known as Ostwald ripening and it is one of the main causes of ECSA loss.

Platinum loss in the membrane

Another loss source is platinum migration into the membrane. As the platinum dissolves in the electrolyte, the concentration of dissolved ions rises, creating a concentration gradient toward the membrane. Then, Pt ions can migrate through the electrolyte toward the membrane, and eventually precipitate there forming the so-called Pt band, reacting with crossover hydrogen according to reaction (9). This platinum is not active anymore, as it cannot be reached anymore by the oxygen, and represents another cause of performance loss.

$$Pt^{2+} + H_2 \rightarrow Pt + 2H^+ \tag{9}$$

Chemical dissolution

When the potential decreases, the oxide is reduced and the platinum is exposed again to dissolution. Nonetheless, it has been observed that the oxide can also dissolve directly into the electrolyte. Although there is no general consensus in the literature about the nature of this mechanism and its driving force, some reactions have been proposed, among these chemical dissolution [6][7][9] (reaction (10)). The reaction rate doesn’t depend on the voltage but only on the oxide coverage. Anyway this reaction is difficult to be measured or quantified, and it's often considered not really relevant [6].

$$PtO + 2H^{+} \rightarrow Pt^{2+} + H_2O \tag{10}$$

Place exchange

As the potential reaches higher value (above 1.1 V) or a certain value of potential is kept constant for a sufficient time, the repulsive interactions between the oxygen atoms absorbed on the platinum surface because of oxidation induces the O atoms to undergo a place-exchange from surface to subsurface position (Figure 4), exposing Pt atoms once again [4]. At this point, the exposed platinum can be oxidized again so that the oxides begin to build deeper into the platinum lattice.

This mechanism, called place-exchange, allows to explain the formation of more than one layer of oxide, which is measured experimentally for high potentials or long holding times.

It is worth underlining that there is not an overall consensus in the literature about this reaction. Indeed, it is not clear whether the driving force of this mechanisms is the potential or the oxide coverage, as both conditions happen simultaneously. Moreover, it is not certain whether the place-exchange is a reversible o irreversible reaction.

While in deaerated solutions the place exchange is usually considered relevant at potential higher than 1.15V, lower values have been reported in the presence of oxygen. According to Kongkanand [10], in presence of oxygen place-exchange initiates at potentials as low as 0.75 V.

Cathodic dissolution

The increase of Pt concentration which is experimentally observed [4][5] during decreasing potential sweeps can be associated to the dissolution of place-exchanged oxides directly in the electrolyte. This reaction is called cathodic dissolution, as it is supposed to take place mainly during cathodic potential sweeps (decreasing potential). There is no general consensus in the literature about its exact formulation. Some authors describe it as shown in reaction (11)[7] , while other authors [5] associates cathodic dissolution to a more complex oxides, PtO_2 which is obtained by the further oxidation of place-exchanged oxides.

Differently from the chemical dissolution, it is described by some authors as a potential dependent reaction [8][7].

As for place exchange reaction, the role of cathodic dissolution is still not clarified in literature.

$$OPt + 2H^{+} \rightarrow Pt^{2+} + H_2O \tag{11}$$

$$PtO2 + 2e^{-} + 4H^{+} \rightarrow 2H_2O + Pt^{2+} \tag{12}$$

Carbon corrosion

Catalyst layers are made up of Pt nanoparticles on a carbon porous structure. This carbon structure is subjected to corrosion in presence of water, according to reaction (12). Considering the normal operating voltage (typically between 0.6 and 0.95 V) the reaction could take place, but the low temperature kinetically limits it.

$$C + H_2O \rightarrow CO_2 + 4H^{+} + 4e^{-} \qquad E^0 = 0.207\ \mathrm{V} \tag{13}$$

Nonetheless, in peculiar operating conditions as fuel starvation or start-up and shutdown processes the voltage can increase above 1 V making the carbon corrosion from the support, making them not active anymore, as they cannot be reached from the gas which flows through the carbon porous structure. Although this phenomenon doesn't directly involve the catalyst, it is an important source of ECSA loss. Indeed, it causes the detachment of Pt articles.

Figure 4 depicts the main mechanisms involved in catalyst layer degradation, previously explained.

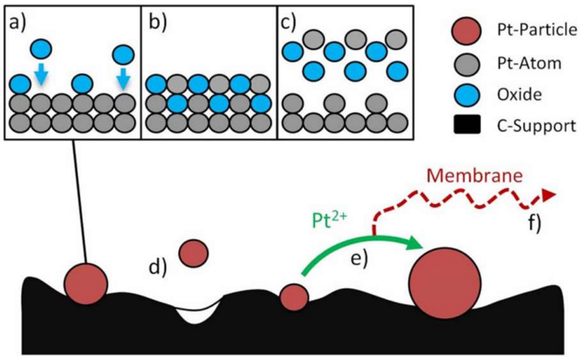

Figure 4 - Pt degradation mechanisms (a) Pt oxidation (b) Place exchange (c) oxide reduction and oxide dissolution in the ionomer (d) Carbon corrosion (e) Ostwald ripening [7]

1.3. Platinum dissolution models: a literature review

In the literature, several platinum dissolution models with different level of complexity have been developed to simulate this phenomenon and achieve a deeper comprehension of its physics. This works focuses on zero-dimensional models, which allow to predict ECSA evolution over time with acceptable computational times.

As already said, Pt dissolution is strongly related to oxidation, as the oxide protects the particle from dissolution. Consequently, dissolution models always contains both oxidation and dissolution reactions, described with different equations, which generally depend on potential. Furthermore, material balances will be necessary to obtain the evolution of quantity of interest, i.e. oxide coverage, platinum concentration in the electrolyte and particle radius.

In the literature, different dissolution models have been proposed, which will be described in the following.

Some major reactions are always considered (anodic dissolution, Pt oxidation), although differently modelled, while other mechanisms and reactions (place exchange, chemical and cathodic dissolution) are not always considered, depending on the model complexity and on the relevance the authors attribute to them. The main reactions involved are those exposed in section 1.2.1.

Darling and Meyers, the first kinetic dissolution model

Darling and Meyers [6] proposed the first kinetic dissolution model, including anodic dissolution, Pt oxidation, and chemical dissolution.

The anodic dissolution and Pt oxidation are electrochemical reactions, therefore they follow a Butler-Volmer equation, as shown respectively in equations (13) and (14), where k_1 and k_2 are kinetic constants, Φ_1 is the solid potential, Φ_2 is the membrane phase potential, U_1 is the dissolution equilibrium potential, U_2 is the oxidation equilibrium potential, θ_{PtO} is the surface fraction covered by oxides, $\mathrm{c}_{\mathrm{Pt}^{2+}}$ and $\mathrm{c}_{\mathrm{H}^+}$ are platinum and protons concentration in the electrolyte, ω is the PtO-PtO interaction energy.

$$r_1 = k_1(1-\theta_{\mathrm{PtO}})\left[\exp\left(\frac{\alpha_{a,1}\mathrm{n}_1\mathrm{F}}{RT}(\Phi_1-\Phi_2-U_1(r))\right)-\left(\frac{\mathrm{c}_{\mathrm{Pt}^{2+}}}{\mathrm{c}_{\mathrm{Pt}^{2+},ref}}\right)\exp\left(-\frac{\alpha_{c,1}\mathrm{n}_1\mathrm{F}}{RT}(\Phi_1-\Phi_2-U_1)\right)\right] \tag{14}$$

$$r_2 = k_2 \left[\exp\left(-\frac{\omega\theta_{\mathrm{PtO}}}{RT}\right) \exp\left(\frac{\alpha_{a,2}\mathrm{n}_2\mathrm{F}}{RT}(\Phi_1 - \Phi_2 - U_2(r))\right) - \theta_{\mathrm{PtO}} \left(\frac{\mathrm{c}_{\mathrm{H}^+}}{\mathrm{c}_{\mathrm{H}^+,ref}}\right)^2 \exp\left(-\frac{\alpha_{c,2}\mathrm{n}_2\mathrm{F}}{RT}(\Phi_1 - \Phi_2 - U_2)\right) \right] \tag{15}$$

Both the reaction rates (measured in $\frac{mol}{cm_{Pt}^2*s}$) depend on the difference between the applied potential and the equilibrium potential of the reaction. The equilibrium potential depends on the particle radius, ad it is lower than the reference equilibrium potential (which refers to bulk Platinum), being corrected with a term directly proportional to the surface tension σ_{Pt}, and inversely proportional to the particle radius, as shown in equations (15) and (16) for the dissolution equilibrium potential U_1. The oxidation equilibrium potential U_2 is corrected too following the same principle.

$$U_1 = U_1^{\vartheta} - \frac{\Delta\mu_{Pt}}{2F} \tag{16}$$

$$\Delta\mu_{Pt} = \frac{\sigma_{Pt} M_{Pt}}{r\rho_{Pt}} \tag{17}$$

Experimental observations show that the oxide growth is logarithmic with time. This suggests that the reaction rate is lowered by the presence of already formed oxides. The exponential term in equation (15), depending on the interaction energy ω, allows to reproduce this trend.

The third considered reaction is chemical dissolution, whose reaction rate follows equation (17). k_3 is a kinetic constant and K_3 is an equilibrium constant, depending on the anodic dissolution and oxidation equilibrium potential U_1 and U_2.

$$r_3 = k_3 \left(\theta_{\mathrm{PtO}} \mathrm{c}_{\mathrm{H}^+}^2 - \frac{c_{Pt^{2+}}}{K_3} \right) \tag{18}$$

In this model, the whole dissolution is attributed to the anodic dissolution, as the chemical dissolution kinetic constant k_3 is arbitrarily set to a very low value, as the authors didn't have experimental data to calibrate it. Although reactions rates depend on the particle radius, the Ostwald ripening mechanisms is not reproduced, as simulations are made with a constant radius instead of a radius distribution.

Schneider et al., a more complex model

Schneider et al. [7] started from Darling and Meyers' model, adding some reactions and mechanisms.

Anodic dissolution, Pt oxidation and chemical dissolution are described with the same equations. The oxidation and the anodic dissolution reaction rates depend on the difference between the applied potential and the equilibrium potential of the reaction, shifted from the reference value to take into account the surface tension effect.

In this model also place exchange and cathodic dissolution are included, according to equations (19) and (20), where k_{PE}, $k_{PE,r}$ and k_{Cd} are kinetic constants, φ is the applied potential, φ_{PE} is the place exchange equilibrium potential, θ_{OPt} is the place-exchanged oxides coverage, ω_{PE} is the OPt-OPt interaction energy, $\theta_{OPt,lim}$ is the maximal stable place-exchanged oxide surface coverage, which is obtained by setting r_{PE} to zero and solving the equation for θ_{OPt}.

$$r_{PE} = k_{PE}\theta_{PtO} \exp\left(\frac{\omega_{PE}\theta_{PtO}}{RT}\right) \exp\left(\frac{\beta F(\varphi - \varphi_{PE})}{RT}\right) - k_{PE,r}\theta_{OPt} \exp\left(\frac{\omega_{PE,r}\theta_{OPt}}{RT}\right) \quad (19)$$

$$r_{Cd} = k_{Cd}\left(\theta_{OPt} - \theta_{OPt,lim}\right) \qquad for\ \ \theta_{OPt} > \theta_{OPt,lim} \quad (20)$$

$$r_{Cd} = 0 \qquad for\ \ \theta_{OPt} < \theta_{OPt,lim}$$

Finally, the Pt loss in the membrane is considered, according to Fick’s first law as shown in equation (21), where D_{diff} is diffusion coefficient, L_x is the diffusion length and h_{CL} is the catalyst layer thickness.

$$q_{Ptloss} = -D_{diff}\frac{c_{Pt}^{2+}}{L_x h_{CL}} \quad (21)$$

As already said, place exchange and cathodic dissolution are not univocally described in the literature, as there is no total consensus about the mechanisms and their driving forces. Consequently, they are modelled with different equations. Here is an outline of the most interesting features of Schneider’s model:

- place exchange forward reaction is modelled as an electrochemical one. The driving force is the difference between the applied potential and the equilibrium potential, set to 1.2 V and not dependent on particle radius;
- place exchange backward reaction is also considered, and is modelled as a chemical reaction, depending only on the place exchange surface coverage θ_{OPt} ;
- cathodic dissolution is dependent on the difference between θ_{OPt} and $\theta_{OPt,lim}$. In this way, it is indirectly linked to potential variation and becomes relevant only when potential reaches high values (which allows to form place-exchanged oxides) and then rapidly decrease (which allows the term $\theta_{OPt} - \theta_{OPt,li}$ to become negative).

Jhanke et al., an indirect place exchange formulation

Jhanke et al. [8] proposed a model based on two Pt oxides, anodic dissolution and cathodic dissolution. Place exchange is not directly modelled, but it is indirectly considered through the cathodic dissolution, as shown in the following.

The oxide model, as shown in reactions (22), (23) and (24), includes a reversible oxidation of Pt to PtOH, a further irreversible oxidation of this intermediate oxide to PtO, and eventually a reduction of PtO to Pt. Reaction rates follows a Butler-Volmer equation, depending on potential, equilibrium potential and oxide coverage.

$$Pt + H_2O \leftrightarrow PtOH + H^+ + e^- \qquad E^0 = 0.75\,V \tag{22}$$

$$PtOH \rightarrow PtO + H^+ + e^- \tag{23}$$

$$PtO + 2H^+ + 2e^- \rightarrow Pt + H_2O \tag{24}$$

What is more relevant for the purpose of this work is the dissolution model.

Anodic dissolution is modelled as in previous models, while cathodic dissolution reaction rate is modelled as proportional to the oxide reduction reaction rate, as shown in equation (25), where $r_{ox,r}$ is the oxide reduction reaction rate, k_f is a proportionality constant, $A(r)$ is the surface area of all particles with radius r (platinum surface for unite of electrode area), Γ is the Pt surface site density (Pt moles per unit of Pt area) and $X_{edge}(r)$ describes the fraction of edge sites of the platinum particle, depending on the size and geometry of the particles.

$$r_{Cd}(r) = A(r)\Gamma\, k_f X_{edge}(r)\, r_{ox,r} \tag{25}$$

The peculiarities of this model are the following:

- Place exchange is not directly modelled;
- cathodic dissolution is proportional to the oxide reduction reaction, indirectly describing place exchange mechanism. The idea behind this formulation is that the platinum oxidation can lead to a place exchange between the platinum and oxygen atoms; when potential decreases, oxides are reduced, and place-exchanged oxides can directly dissolve into the electrolyte. In this way, place exchange is not taken into account in material balances, nonetheless its effect on dissolution is considered: when potential decreases the oxide reduction (Equation (24)) and the oxide dissolution in the electrolyte (cathodic dissolution) take place at the same time, reproducing the same mechanism modelled with place exchange;

- a direct dependence of cathodic dissolution on particle size is introduced with the term $X_{edge}(r)$.

Karan et al, Platinum oxidation and ORR interaction

Karan et al [9], developed a single reaction framework, which includes both ORR reaction and platinum oxidation. The proposed model does not include dissolution, but it is of peculiar interest as it features a detailed description of place exchange and explores the potential influence of the presence of oxygen and ORR reaction on platinum oxidation. This is very remarkable as in real operation ORR and platinum oxidation and dissolution take place simultaneously, while typically experimental tests which investigate oxide formation, as well as Accelerated Stress Tests (AST) (which will be described later), are performed in de-aerated conditions, potentially neglecting the effects of the presence of oxygen.

The model proposes a multi-step oxidation model as shown in reactions from 26 to 30, including a reversible oxidation of Pt to PtOH, a further oxidation of this intermediate oxide to PtO, a place exchange between platinum and oxygen atoms, a further two-steps oxidation of place-exchanged atoms to OPtOH and eventually to OPtO.

$$Pt + H_2O \leftrightarrow PtOH + H^+ + e^- \qquad E^0 = 0.79\,V \tag{26}$$

$$PtOH \leftrightarrow PtO + H^+ + e^- \qquad E^0 = 0.79\,V \tag{27}$$

$$PtO \leftrightarrow OPt \qquad E^0 = 1.2\,V \tag{28}$$

$$O - Pt + H_2O \leftrightarrow O - Pt - OH + H^+ + e^- \qquad E^0 = 0.98\,V \tag{29}$$

$$O - PtOH \leftrightarrow O - Pt - O + H^+ + e^- \qquad E^0 = 0.98\,V \tag{30}$$

All the reactions are considered reversible. The oxidation reactions are modelled with a Butler-Volmer equation, depending on the applied potential and the reaction equilibrium potential, while the place exchange reaction is modelled as a chemical reaction, as shown in equation (31).

$$r_{PE} = k_{PE}\theta_{Pto} \exp\left(-\omega_{PE} \frac{\theta_{OPt} + \theta_{OPtOH} + \theta_{OPtO}}{kT}\right) - k_{PE}\theta_{OPt} \tag{31}$$

Karan's oxide model is therefore much more complex and detailed than the previous ones, requiring a higher number of material balances (one for each coverage θ), and consequently major computational efforts.

As for oxygen presence influence, it is worth underlining two concepts:

- in the presence of oxygen place exchange can start at potential values as low as 0.9 V, while much higher values (1.15 V) are typically reported in deaerated solutions;
- the kinetic model developed to describe the platinum oxide growth is then completed with additional reaction steps in order to capture oxygen reduction reaction within a single kinetic framework. Although the resulting model is really complex and goes beyond the field of interest of this work, it's worth underlying that ORR and platinum dissolution are described not as separate mechanisms, but as a unified one.

1.4. Objective of the work

In order to address the durability issue, it is essential to achieve a deeper comprehension of the physics phenomena responsible for degradation. This will eventually allow to find some strategies to counteract it. This work aims to investigate catalyst degradation during realistic operating conditions, exploring the physics phenomena which lead to platinum dissolution and ECSA loss.

To this aim, a zero-dimensional physics-based platinum dissolution model is developed, including the main reactions involved in platinum dissolution.

An experimental analysis is also made, performing several Accelerated Stress Tests (ASTs) in hydrogen/air with different voltage profiles, under conditions that mimic realistic automotive dynamic power operation. The objective is to investigate the effect of different voltage profiles and limit values.

Model predictions will be compared with experimental results to provide insight into the degradation process and improve model formulation.

2 Experimental

In this chapter, firstly the structure of the used cell and the plant layout are described, secondly testing procedures are presented, which are divided in characterization protocols and degradation protocols.

2.1. Experimental set-up

The same hardware, a Multi Zero-gradient cell (Multi-0G), has been used for all experimental activities. This particular hardware, showed in Figure 5, allows to test 4 different cells at the same time.

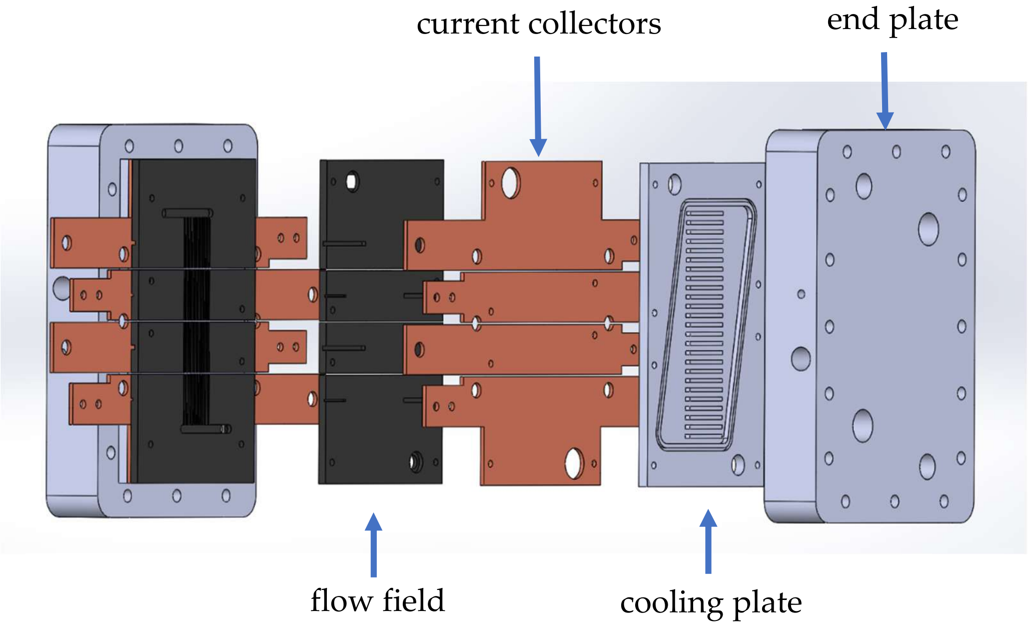

Figure 5 - Hardware Multi-0G

The flow field is indeed divided in four parts which are electrically insulated, and each segment has separate current collectors, which ensures electrical insulation. Therefore, each MEA tested along the flow field operates as if in a standard single cell hardware.

The cell area is really small and the used flowrates are typically much higher than stoichiometric ones, so that operating conditions as gas relative humidity and oxygen concentration in the channel are kept almost constant among the different samples.

Thank to this hardware more experimental data can be obtained simultaneously, strongly reducing the testing time. It's possible indeed to test different materials at the same time, using the same degradation protocol and analyse their response to the same stressor or, alternatively, it's possible to use the same materials and apply different degradation protocols, analysing thus its response to different stressors. Obviously, operating conditions (temperature, flowrates, relative humidity) cannot be varied among the cells, while imposed current or voltage can be different for different segments.

MEA's Assembly

All experimental activities were performed with the same Catalyst Coated Membrane (CCM), with an active area of 2 cm^2 per each cell. Its Pt loading is of 0.5 mg cm^{-2} for the cathode and 0.1 mg cm^{-2} for the anode. It was assembled with a commercial automotive GDL (Freudenberg GDL H14CX483).

Mylar gaskets were used to support the MEA's assembly: two 100 μm thick gaskets to limit gas leakages and support the GDL, two 23 μm thick sub-gaskets to define the active area, and another 23 μm thick sub-gasket to support the CCM. The samples resulted as 80% mechanically compressed.

Flow field

The flow fields (shown in Figure 6) are realised with graphite and they are made by two manifolds and 24 parallel channels 0.6 mm wide and 0.3 mm deep respectively. For the segmented hardware, both at anode and cathode the distributors are divided into four parts and segmentation cuts are filled with an insulant material, which ensure electrical insulation among the segments.

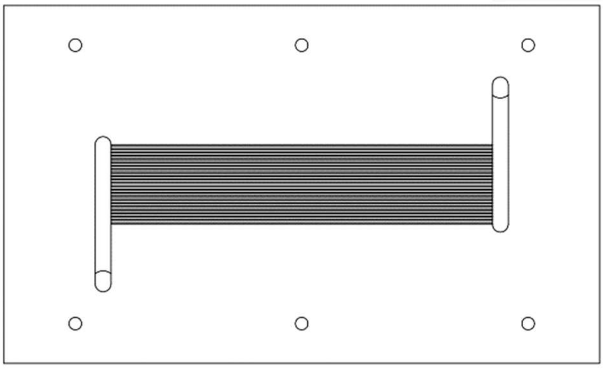

Figure 6 - Flow field

Current collectors

These components allow to collect the current produced and link the graphite to the external circuit. They are made of chromium plated copper to maximize their electric conductivity, and they are directly in contact with the flow fields. In multi-0G hardware, four separate current collectors are used, one for each segment, as shown in Figure 7.

The connection to the electronic load is based on sources and senses cables. Two couplets of senses cables are necessary, as two different loads are used for different testing protocols. Moreover, voltage measurement passes also through a data acquisition system. A total of 8 cables is thus necessary for each segment.

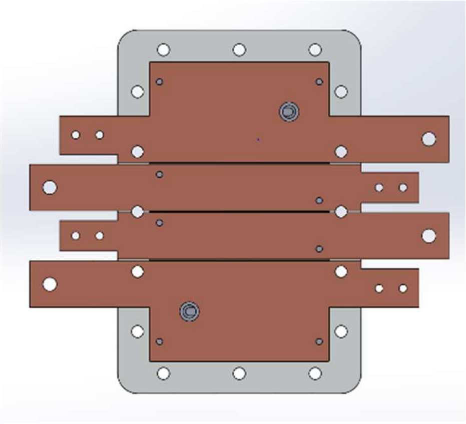

Figure 7 - Current collectors

End plates

The end plates are made in aluminium, and their function is holding together the different components and assure a proper compression of the MEA. The compression must be as uniform as possible and strong enough to avoid leakages. Sixteen 10 mm bolts are thus distributed along the edges and are tighten with a torque wrench to 8 Nm.

Two cylindrical caves are milled in the end plate to host electrical cartridge heaters, which have been used to control the cell temperature. With this hardware a liquid cooling system could alternatively be used, with liquid water flowing between the cooling plate and the end plate, which provides a more uniform temperature control, but also implies a higher system complexity.

2.2. Basic plant layout

The basic plant layout is shown in Figure 8, where the solid lines indicate fluid pipelines, while the dashed ones are electric connections. In the left side of the scheme there are feed gas tanks, mass flow meters and bubblers, necessary to heat and humify gases that are fed to the cell. The used gases are hydrogen, Nitrogen, Air and Oxygen. The gases flowrates are set by electronic flow meters, that ensure a fast control. Some upstream valves, not drawn, allow to switch from Air to oxygen, as they share the same flow meter. The bubblers saturate the gases before they enter the cell, keeping the relative humidity to the desired value. The dew point temperature is regulated by means of a T-controller. A pump fills the bubblers any time the level of water, provided by a float, drops down. Heated ducts are used immediately downstream to avoid the decrease of flow temperature and water condensation and the cell itself is heated up with an electrical heating system, based on cartridge heaters which are placed in dedicated holes milled in the end plates. The ducts and the cell heating are managed by T-controllers.

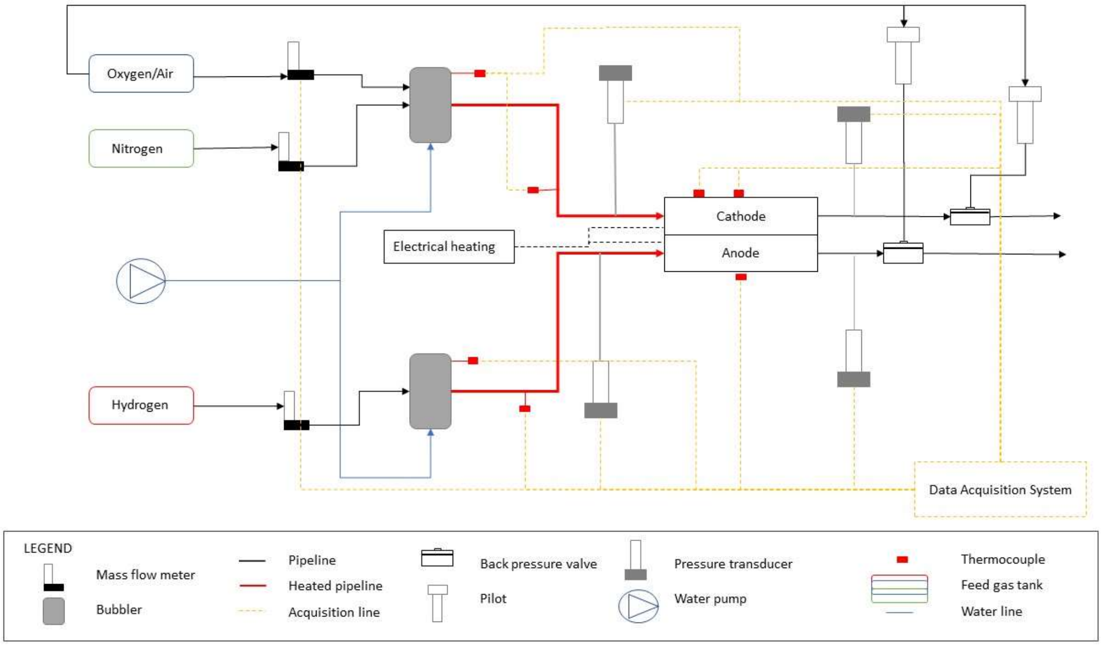

Figure 8 - Basic plant layout [11]

Pressure is regulated with back pressure valves which are placed downstream of the cell. Both the upstream and the downstream pressure are measured by means of transducer. All the measured quantities are collected by the data acquisition system.

2.3. Characterization protocols

In this paragraph the characterization protocols will be described, which have been used to measure cell performances. Characterization tests were performed at the Beginning Of Tests (BOT), and then repeated at each stop of the AST (every 200/400 cycles) and at the End Of Test (EOT), in order to track the performances evolution.

To perform characterization protocols, the following electronic devices have been used:

- The electric multichannel Chroma® 63610-80-80, which sets currents - in galvanostatic operations - through sources cables, while measures the voltage through senses, so that it is not affected by cables resistance. This load is generally used for in operando tests with H_2/air or H_2/O_2 feed, such as polarization curves and EIS (described in following paragraphs). It could also work in a potentiostatic mode and the power that is produced is dissipated. These operando tests are managed by some LabView System Design Softwares.
- Autolab with 20 A Booster has been used to perform in-situ tests, as Cyclic Voltammetry (CV), Linear Sweep Voltammetry (LSV) and Resistance Catalyst Layer measurement (RCL), which are described in the following paragraphs. Autolab is a potentiostat and is able to work both in galvanostatic and potentiostatic operation. It works too with sources and senses cables to impose and measure current or voltage, and it is commanded by NOVA user interface.

The collected raw data are saved and then post-processed using Matlab.

2.4. Cyclic voltammetry

The Cyclic Voltammetry (CV) is an in-situ test performed feeding nitrogen at the cathode and hydrogen at the anode. Temperature, flowrates, and relative humidity are kept constant during the test. Thanks to a potentiostat, the potential is increased at a constant rate from a minimum value (which corresponds to the Open Circuit Voltage, OCP) to a maximum value, and then decreased again down to the initial value. In the meanwhile, current is recorded. The resulting i-V curve (shown in Figure 9) is called cyclic voltammogram. Several scans (the combination of an increasing and a decreasing potential sweep) are typically performed, to obtain more reliable results.

In the cyclic voltammetry, it's possible to identify different potential regions, in which the measured current is attributed to different phenomena.

In the low potential range, from the Open Circuit Voltage (OCV) to around 0.35 V, the positive current is generated by the hydrogen desorption reaction, from 0.35 to 0.60V a flat current is observed, which is due to the double layer charging, while the current above 0.6 V is due to Pt oxidation. Decreasing potential from 1.2 V to 0.6 V, a negative current is measured, which is associated to Pt oxide reduction, then there is a lower current region, where only double-layer discharging occurs, and finally there is a negative peak due to hydrogen adsorption reaction.

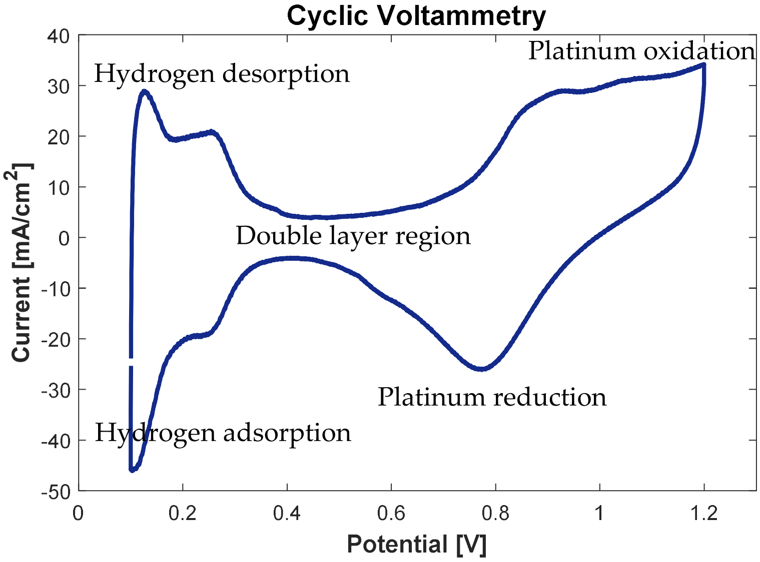

Figure 9 - Cyclic voltammetry

Integrating the current of the desorption peak, from OCV to the point of minimum current of the double layer region, it's possible to estimate the ElectroChemically active Surface Area (ECSA) with the following expression:

$$ECSA = \frac{\int_{OCV}^{E_{dl}} (i - i_{DL})\, dV}{\sigma_m L_{Pt}\, n_e\, SR} \left[\frac{m^2}{g_{Pt}}\right]$$

Where i_{DL} is the double layer current, σ_m is the hydrogen charge density, assumed 210 μC cm−2, n_e is the ratio between adsorbed hydrogen atoms and used catalyst surface, L_{Pt} is the platinum loading, and SR is the Scan Rate [mV s−1], i.e. the velocity of potential variation.

Similarly, in the higher potential region, it is possible to estimate the oxide coverage integrating the current from the local minimum of the double layer region to the maximum potential value, according to the following formula:

$$\theta_{PtO} = \frac{\int_{E_{dl}}^{E_{ma}} (i - i_{DL})\, dV}{\sigma_m L_{Pt}\, n_e\, SR\, ECSA}$$

Typically, CV are stopped at either 0.6 V or 1.2 V as further increasing potential leads in a favourable carbon corrosion region, which must be avoided.

For this work, CV were performed at room temperature, with fully humidified streams and flowrates of 100 ml/min at both electrodes.

The following procedure has been applied:

- OCV was measured at BOT in the test operative conditions, this value has been used during the whole degradation test in order to obtain comparable i-V curves;
- 5 scans were executed starting from the OCV and going up to 0.6 V;
- 5 scans were executed starting from the OCV and going up to 1.2 V. These are referred to as cleaning scans, as it is expected that reaching so high potential values, the catalyst is totally oxidated and then totally reduced. In this way the active surface is cleaned up from all oxides and other possible contaminants that could affect the ECSA measurement.
- 5 more scans were executed starting from the OCV and going up to 0.6 V. The ECSA measure was made on these scans, as the whole platinum active area is expected to be cleaned after the high potential scans.

The used scan rate was 0.1 V/s for all the scans.

As previously explained, the current measured in the cyclic voltammetry is due to the hydrogen adsorption and desorption reaction, the double layer charging and discharging and the platinum oxidation and reduction. Nevertheless, the crossover current (due to hydrogen crossover through the membrane), as well as the short-circuit current (due to the fact that the membrane is not a perfect insulant, therefore some electrons may flow through it), will be also detected, affecting the current measurement. For this reason, CVs were corrected, subtracting from the measured current the terms due to crossover and short circuit, as shown in equation 1, where I_{cross} is the crossover current and R_{ohm} is the ohmic resistance, which can be measured with a specific test, the Linear Sweep Voltammetry, described in the following.

$$I_{corr} = I_{measured} - I_{cross} - I_{measured} * R_{ohm} \qquad (1)$$

2.4.1. Linear sweep voltammetry

Linear Sweep Voltammetry is an *in situ* technique used to measure the hydrogen crossover and the membrane electric resistance, and to determine whether there is a short circuit or pinholes between the electrodes.

To perform this measurement, nitrogen is used to purge the fuel cell cathode while hydrogen is passed through the fuel cell anode. As for cyclic voltammetry, temperature, relative humidity and flowrates are kept constant.

During the test, the potential of the fuel cell cathode is swept by means of a linear potential scan. This test is characterized by a really slow potential increase, with scan rates as low as 1 mV/s. As the membrane is not totally impermeable, some hydrogen (crossover hydrogen) reaches the cathode in gas phase. Thanks to the rising potentials, any hydrogen gas present at the fuel cell cathode is instantaneously oxidized.

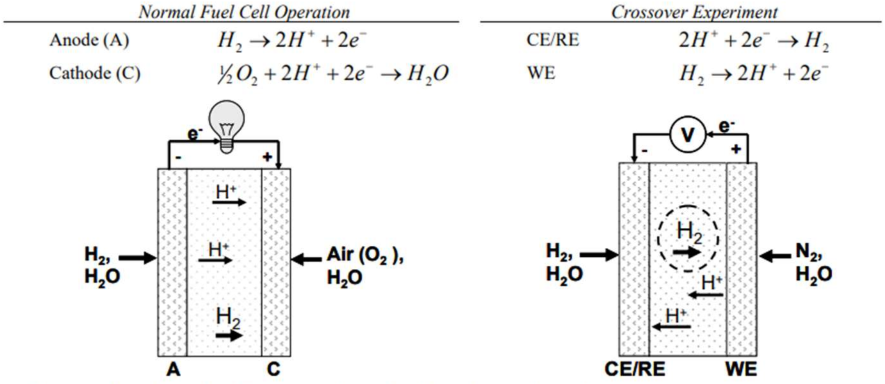

WE = working electrode, CE = counter electrode, RE = reference electrode.

Figure 10 - LSV principle [12]

Consequently to hydrogen oxidation, and thanks to the potential difference imposed by the potentiostat, protons and electrons flow back to the anode respectively through the membrane and through the external circuit, as shown in Figure 10. A current can thus be measured.

Additionally, although the electrolyte is designed to be an ionic but not electronic conductor, direct conduction of electrons between the electrodes through the membrane can take place. The resultant current is called short-circuit current, and it represents a source of loss. This current is proportional to the imposed potential and to the membrane ohmic resistance.

Typically, crossover and short-circuit currents at BOT are really low, but they become more relevant when the membrane is damaged or degraded.

The result of the test is a chart of the current as a function of the voltage, which presents a specific trend: a first very fast current increase and then a plateau, as shown in Figure 10. The ohmic membrane resistance is defined as the inverse of V-i slope, the crossover current is the intercept of the y-axis, obtained extending the ohmic linear region (plateau).

For this work, LSV were performed at room temperature, with fully humidified streams and flowrates of 100 ml/min at both electrodes.

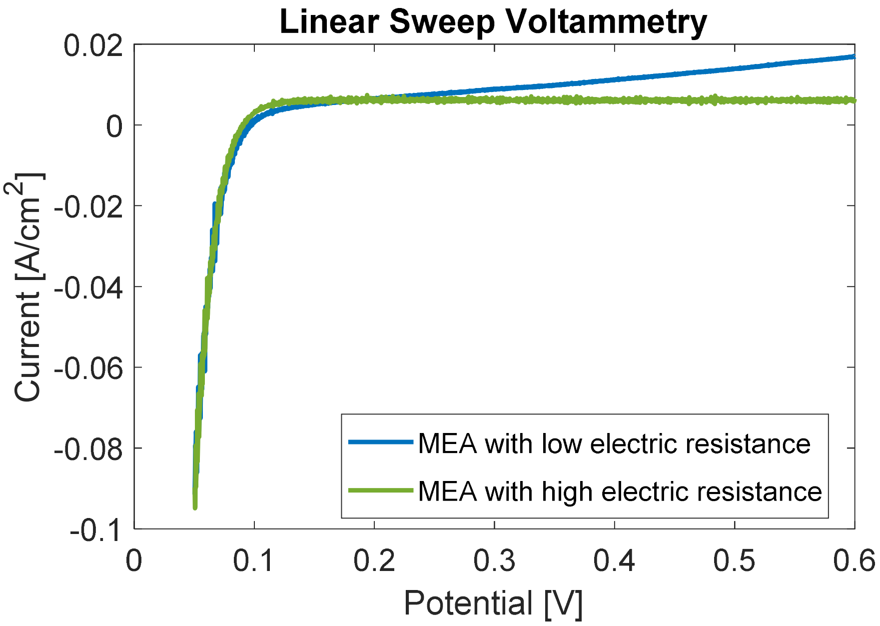

Figure 11 - Linear Sweep Voltammetry

2.4.2. Electrochemical Impedance Spectroscopy

The Electrochemical Impedance Spectroscopy (EIS) is a time-based technique, in which current, oscillating with a sinusoidal wave with a decreasing frequency, is imposed, and the resultant voltage is measured. The impedance is thus calculated, as shown in equation (2), where Z_{real} is the real (resistive) part and Z_{im} is the imaginary (inductive or capacitive) part. EIS are typically performed with H_2/O_2 or H_2/air feed.

The impedance is represented in a Nyquist plot: the real part is plotted on the X-axis and the imaginary part is plotted on the Y-axis. Each point on the Nyquist Plot corresponds to the impedance at a certain frequency.

$$Z(\omega) = \frac{E}{I} = Z_{real} + i * Z_{im} \qquad (2)$$

In the Nyquist plot it is possible to distinguish some features linked to phenomena occurring in the fuel cell. Some of these phenomena (i.e. ionic phenomena), showing a faster response, are highlighted in the high frequency region, while others (i.e. mass transport phenomena), showing a slower response, can be appreciated just at low frequencies. At different current values the EIS will have different shapes, highlighting different phenomena. An example is shown in Figure 12.

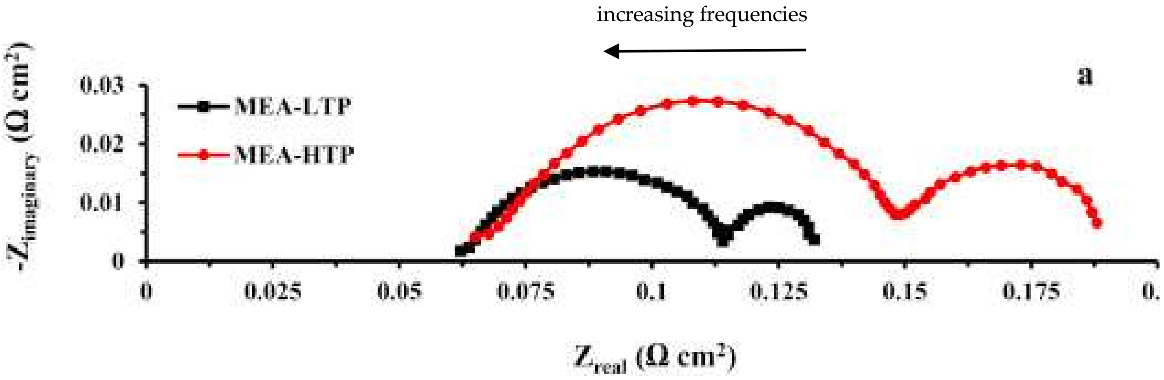

Figure 12 - Electrochemical impedance spectroscopy [13]

From the EIS plot it is thus possible to identify:

- The High Frequency Resistance (HFR), which is the sum of contact and ohmic resistance of GDL, MPL and membrane, and can be measured as the intercept of the chart at high frequencies with the real axis. Ohmic phenomena are really fast indeed, and ohmic resistances are characterized by a real impedance (a simple electric resistance);
- A main arch, which is linked to ORR kinetics and accounts for Charge Transfer Resistance of the cathode catalyst layer, measured as the length of the arch;
- A second arch, which can be present at low frequencies if the mass transport effects are significative (i.e. at high current values). It is indeed related to oxygen mass transport, which is a slow phenomenon, and becomes relevant in mass-transport limiting conditions. From the diameter of this arch it's possible to estimate the Mass Transfer Resistance.
- A linear branch with a slope of 45° in the first part of the main arch: it is caused by the Resistance of the Catalyst Layer (RCL) to the proton transport,

which shows both a resistive and a capacitive component. Nonetheless, this linear branch is not always clearly visible.

2.4.3. Catalyst layer resistance measurement

The Catalyst Layer Resistance measurement (RCL) is a peculiar type of Electrochemical Impedance Spectroscopy (EIS).

RCL is performed feeding hydrogen at the anode and nitrogen at the cathode, keeping constant temperature, relative humidity and flowrates. Instead of a current, a potential is imposed, which then starts to oscillates with varying frequency. An example of the resulting Nyquist plot is shown in Figure 13. From this plot it is possible to identify the HFR and the linear branch.

For this work, RCL were performed at room temperature, with fully humidified streams and flowrates of 300 ml/min at both electrodes. A potential of 0.3 V was imposed, and frequencies were varied from 10 kHz to 1 Hz.

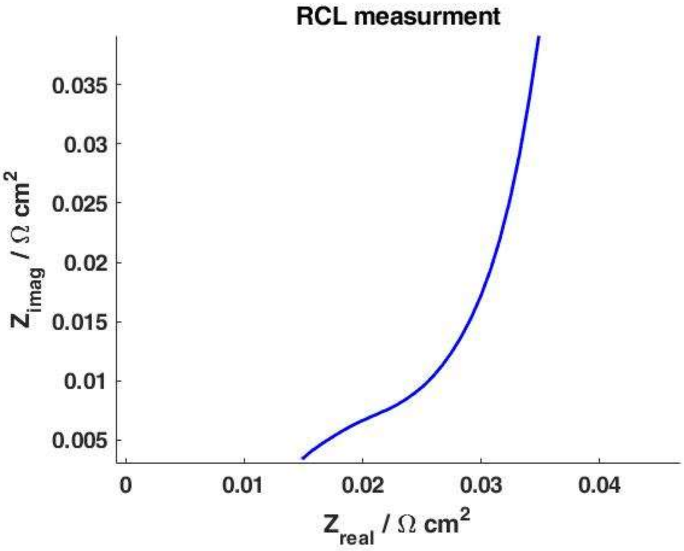

Figure 13- RCL measurement

2.4.4. Polarization curve

Polarization curve is the technique traditionally used to assess fuel cell performances. Different current values (starting from 0A and gradually increasing) are imposed. Each current value is kept constant for a while (1 or few minutes), and the resulting voltage is measured, obtaining the V-i chart, as shown in Figure 14.

This test allows to have an overview of the cell performances and of main loss sources, which strongly affect the shape of the V-i curve. Three major types of overpotentials can be outlined: the first one is due to reactions kinetic, the second one to ohmic losses, the last one to mass transport losses. During a durability test, it's thus possible to calculate the increase of overpotentials and determine the causes of performance losses.

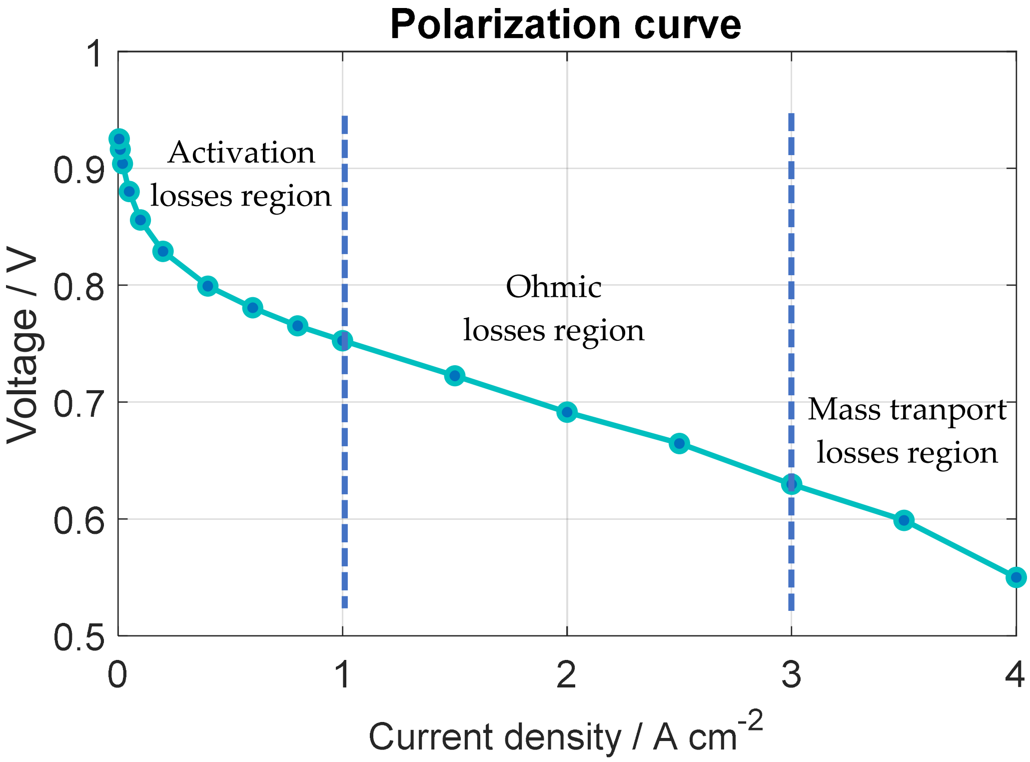

Figure 14 - Polarization curve

It is possible indeed to distinguish different regions in the i-V curve, where one of these losses is more relevant.

At open circuit (zero current), although there a no overpotentials, the actual Open Circuit Voltage (OCV) is generally lower than the theoretical one (1.23 V). This loss is due to hydrogen crossover and short circuit current. For low current density values, there is a steep potential decrease. This region is referred to as the ORR activation polarization region. The main loss source is indeed the kinetic overpotential due to the activation of ORR. In the intermediate current range the voltage decreases almost linearly. This region is referred to as the ohmic region, as the main loss source is the internal protonic and electric resistance, mainly due to the membrane and to the CL. For higher current values, voltage start to decrease more rapidly, and finally approaches a limit value. The mass transport of the reactants limits indeed the reactions. Oxygen transport at the cathode is particularly difficult, as the produced water hinders oxygen diffusion, or even partially obstructs (when it becomes liquid) the pores of the carbon structure of GDL and CL. This region is known as the mass transfer polarization region.

Many types of polarization curves may be performed, which differ in the operative conditions (temperature, RH, pressures), in the cathode feed gas (air or oxygen) and in the current range.

For this work, a polarization curve with the following characteristic was performed.

Operating conditions are reported in Table 1, while current values and holding time are reported in Table 2. Stoichiometry was set to fixed values, but the minimum flowrate is set at 0.2 Acm^{-2}, meaning that for lower currents the test is performed at fixed streams instead of fixed stoichiometry.

Parameter	Unit	Value
Nominal cell operating temperature	°C	80
Anode		
Gas inlet temperature	°C	90
Gas inlet humidity	%	100
Gas pressure (absolute)	kPa	250
Gas inlet stoichiometry	-	8
Cathode		
Gas inlet temperature	°C	90
Gas inlet humidity	%	100
Gas pressure (absolute)	kPa	230
Gas inlet stoichiometry	-	20

Table 1 - Polarization curve operating conditions

First, a reference current value of 0.5 A cm^{-2} is imposed for 300 s, then the current points are imposed. Only the descending points are used for the i-V curve and the initial transient from one imposition to the next is depleted during data analysis. EIS are usually obtained at 3, 2 and 1 A cm^{-2}, with frequency range from 10 kHz to 0.1 Hz.

Current density [A cm-2]	Dwell time [s]
0,005	60
0,01	60
0,02	60
0,05	60
0,1	180
0,2	180
0,4	180
0,6	180
0,8	180
1	180
1,5	180
2	180
2,5	180
3	180
3,5	180
4	180
3,5	180
3	180
2,5	180
2	180
1,5	180
1	180
0,8	180
0,6	180
0,6	180
0,4	180
0,1	180
0,005	60
0,002	60
0,001	60
0,005	60

Table 2 - Polarization curve points

2.5. Accelerated Stress Test protocols

Accelerated Stress Tests (ASTs) are commonly used to study fuel cell degradation. Their aim is to reproduce the degradation due to real operation in much shorter time, allowing a significative cost and time reduction. The degradation is accelerated by means of higher stress level and/or a more frequent stress application.

In this work ASTs were used to mimic realistic operation and study degradation, focusing on platinum degradation. The initial reference for the degradation tests design was the ID-FAST Low Power AST, explained in the following. At first this protocol was applied with some modifications, and then other ad-hoc degradation tests have been designed to better investigate phenomena of interest.

With respect to the initial reference, the designed ASTs have the same operating conditions and the same characteristic times, but a different potential profile.

All these tests were performed with the electric multichannel Chroma® 63610-80-80.

2.5.1. Accelerated Stress Test that mimics realistic operation: low power AST

The Low Power AST, mentioned before, was defined in the context of the European project IDFAST [1] (*Investigations on degradation mechanisms and Definition of protocols for PEM Fuel cells Accelerated Stress Testing*). The aim of this project, concluded in December 2021, was to support and promote the deployment of fuel cell vehicles, through the development of appropriate ASTs for PEMFC components, and the development of transfer functions that allow to predict the performance degradation during real world operation knowing the performance degradation produced with the AST.

Low Power AST, developed for Zero-Gradient hardware, aims at reproducing conditions and voltage cycling of the realistic automotive low power operation. The AST is designed to be carry out in galvanostatic mode, in order to be able to see the voltage losses consequent to the aging and compare the result with realistic driving data.

To perform Low Power AST, the current values which corresponds to 0.85 V and 0.70 V are evaluated for each MEA at BOT, and these current values are imposed. A single cycle is thus composed: a step of 30s at the minimum current (i.e. 0.85 V at Bot) followed by a step of 12 s at the high current (i.e. 0.7 V at BoT); these two steps are repeated 6 times and they are finally followed by 30 s at the minimum current. After each set of current cycling, a short stop (110 s) is introduced. The test is performed with constant flux and the operating conditions are shown in Table 3.

Parameters	**Unit**	**Values**
Cell temperature	°C	71
Dew point anode	°C	63
Dew point cathode	°C	59,1
Flow rate anode	-	Fixed at $\lambda = 8$ @ max current
Flow rate cathode	-	Fixed at $\lambda = 20$ @ max current
Pressure anode	kPa	190
Pressure cathode	kPa	140

Table 3 - AST Low Power operating conditions

3 Platinum dissolution model

In this chapter the model will be described, as it was implemented in its first version, mainly taken from the literature [7].

The aim of the proposed model is to simulate the platinum dissolution in the cathode catalyst layer and the consequent ECSA loss as a function of the potential profile which is imposed to the cell.

The model inputs are potential profile, which is the driving force of the whole degradation process, operative conditions (temperature and RH), and initial Particle Radius Distribution (PRD). The model is composed with reaction rate equations and material balances, giving as outputs reaction rates (and currents), oxide coverage, platinum concentration in the ionomer, PRD and ECSA evolution in time.

It is important to highlight the main hypothesis:

- The developed model is zero-dimensional. The described phenomena are in fact not spatially uniform, as their driving force (i.e. the potential) as well as other quantities (i.e. water activity and proton concentration) are not uniform across the catalyst layer. Consequently reaction rates, platinum concentration and oxide coverage will neither be uniform. Nevertheless, a 0D model can provide quite an accurate description, and allows to build a simpler and more manageable model, considerably reducing computational times.
- The model is created to simulate platinum dissolution in a potential range which goes up to 0.95 V, which corresponds to normal operating conditions of a fuel cell. Reactions which take place at higher potentials (i.e. Carbon corrosion or possibly more complex oxides formation) are not modelled, therefore the model simulation will not be representative of what happens in these operating conditions.
- The PRD is represented with a gaussian distribution, discretized with a finite number of particle groups, each one characterized by the particle radius r_i and the corresponding particles amount n_i. Particles of different groups will be subjected to different reaction rates, depending on their radius, while inside the same group all the particles will have the same destiny: either they all grow, or they all shrink. For each group therefore, the particle number remains constant during the degradation, meaning that particles cannot

move into another group, and new groups cannot be generated. With this approach, coalescence is not modelled. During the degradation, if the radius of one group decreases under a minimum value, the group is eliminated.

3.1. Model description

The phenomena described by the model are the following: platinum anodic dissolution, platinum oxidation and platinum oxide chemical dissolution (reaction (3) (4) and (5)), platinum loss into the membrane and Ostwald ripening. With respect the model proposed by Schneider[7], other reactions (place exchange, cathodic dissolution and carbon corrosion) were neglected as they were not relevant below 0.95 V.

$$Pt \rightleftarrows Pt^{2+} + 2e^- \qquad [\Phi_{diss}^{ref} = 1.188\ V] \tag{3}$$

$$Pt + H_2O \rightleftarrows PtO + 2H^+ + 2e^- \qquad [\Phi_{ox}^{ref} = 0.98\ V] \tag{4}$$

$$PtO + 2H^+ \rightarrow Pt^{2+} + H_2O \tag{5}$$

The anodic dissolution reaction rate consists of anodic and cathodic exponential terms, as shown in equation (6) [7], where the anodic term describes the dissolution of Pt and the cathodic term defines the re-deposition of dissolved Pt^{2+} ions, both depending on the overpotential $\Phi - \Phi_{dis}(r)$, namely the difference between the applied electrode potential and the dissolution equilibrium potential. The reaction rate also depends on the concentration of dissolved Pt, $c_{Pt^{2+}}$ and on the oxide coverage θ_{PtO}. This implies that if there is a low amount of dissolved Pt^{2+} in the electrolyte, the anodic term will prevail in the reaction, while a high oxide coverage will strongly hinder both the forward and the backward reaction. Pt dissolution is also promoted by a higher electrode humidification; the kinetic constant is thus assumed to be dependent on the relative gas humidity RH.

$$\begin{aligned} r_{dis}(r) = k_{dis}(1-\theta_{PtO})\Bigg[&\exp\left(\frac{\alpha_{a1} n_1 F}{RT}(\Phi - \Phi_{dis}(r))\right) \\ &- \left(\frac{c_{Pt^{2+}}}{c_{Pt^{2+},ref}}\right)\exp\left(-\frac{\alpha_{c1} n_1 F}{RT}(\Phi - \Phi_{dis}(r))\right)\Bigg] \end{aligned} \tag{6}$$

$$k_{dis} = k_{dis}^{ref}\left(\frac{RH}{RH_0}\right)^{\vartheta} \tag{7}$$

As the catalyst is dispersed as nanoparticles on a carbon structure, the equilibrium potential is shifted from the reference one by means of a Gibbs-Thompson correction, which describes the correlation between the surface energy of a curved surface and particle radius, as shown in equation (8), where Φ_{dis}^{ref} is the equilibrium potential of Pt bulk material and $\Delta\mu_{Pt}$ represents the effect of the surface tension, which is inversely proportional to particle radius, as shown in equation (9) where σ_{Pt} is the surface tension, M_{Pt} is the platinum molar mass, r is the particle radius and ρ_{Pt} is platinum density.

$$\Phi_{dis}(r) = \Phi_{dis}^{ref} - \frac{\Delta\mu_{Pt}}{2F} \tag{8}$$

$$\Delta\mu_{Pt} = \frac{\sigma_{Pt}\, M_{Pt}}{r\, \rho_{Pt}} \tag{9}$$

The anodic reaction rate is thus dependent on the particle radius, assuming, in the same conditions, different values for different particles. For a given potential value, smaller particles will have lower equilibrium potential and will be more prone to dissolution, while bigger particles will have higher equilibrium potential and, consequently, a reaction rate which is lower or even negative. The model is thus able to reproduce Ostwald ripening mechanism, explained in paragraph 1.2.1.

The rate of Pt oxidation also follows the Butler-Volmer equation as given by equation (10). The overpotential $\Phi - \Phi_{ox}(r)$ determines the reaction rate value, as well as its direction.

$$\begin{aligned} r_{Ox}(r) = k_{ox} \Bigg[& \left(1 - \theta_{\mathrm{PtO}}\right) * \exp\left(-\frac{\omega_{PtO}\theta_{\mathrm{PtO}}}{RT}\right) \exp\left(\frac{\alpha_{a2}\mathrm{n_{Ox}F}}{RT}\left(\Phi - \Phi_{ox}(r)\right)\right) \\ & - \theta_{\mathrm{PtO}} \left(\frac{\mathrm{c_{H^+}}}{\mathrm{c}_{\mathrm{H^+},ref}}\right)^2 \exp\left(-\frac{\alpha_{c2}\mathrm{n_{Ox}F}}{RT}\left(\Phi - \Phi_{ox}(r)\right)\right) \Bigg] \end{aligned} \tag{10}$$

The forward reaction term, which describes the oxide formation, is limited by the presence of already formed oxides, thanks to the term $1 - \theta_{\mathrm{PtO}}$ (which is bounded to zero), meaning that the oxide formation is limited to one layer. The coverage θ_{PtO} is intended to include only the most external layer of oxides, while additional layers formation will be modelled with place-exchange in the second version of the model described in chapter 5. The term $1 - \theta_{\mathrm{PtO}}$ was not present in Schneider formulation [7], meaning that the oxide formation may exceed a mono-layer.

The exponential term containing the interaction energy ω_{PtO} is necessary to reproduce the oxide coverage experimental trends, which show a logarithmic oxide growth.

While the anodic term is not dependent on water concentration, considered not limiting for the oxidation, the cathodic oxide reduction is also governed by the proton concentration c_{H^+}, which is assumed to be constant, and is calculated as shown in equation (11), where EW is the equivalent weight of the ionomer, ρ_{Nafion} its density, and λ the amount of water molecules per acid group, dependent on the water activity a_w, which corresponds to relative gas humidity.

$$c_H^+ = \frac{1}{\frac{EW}{\rho_{Nafion}} + \frac{\lambda M_{H_2O}}{\rho_{H_2O}}} \tag{11}$$

$$\lambda = 0.043 + 17.81a_w - 39.85a_w^2 + 36a_w^3 \tag{12}$$

The equilibrium potential is corrected to take into account the particle size effect, as shown in equation (13). Particles with different radius will thus have different oxidation equilibrium potentials, and consequently different oxidation states in the same moment.

$$\Phi_{ox}(r) = \Phi_{ox}^{ref} - \frac{\Delta\mu_{Pt}}{2F} + \frac{\Delta\mu_{PtO}}{2F} \tag{13}$$

$$\Delta\mu_{PtO} = \Delta\mu_{PtO}^{ref} + \frac{\sigma_{PtO}\, M_{PtO}}{r_{Pt}\rho_{PtO}} \tag{14}$$

The platinum oxide, once it is formed, can either be reduced according to the backward oxidation reaction, or dissolve directly into the electrolyte. This reaction is called oxide chemical dissolution, as it is assumed not to be dependent on potential. It is thus modelled like a simple chemical reaction, as shown in equation (15) [3].

$$r_{chem} = k_{chem}\theta_{\mathrm{PtO}}\mathrm{c}_{\mathrm{H}^+}^2 \tag{15}$$

The last considered phenomenon is platinum migration into the membrane. It is described as a diffusive flux, depending on the Pt concentration gradient. The Pt concentration in the catalyst layer is considered constant, according to the 0D hypothesis, while in the membrane it is assumed to be zero. The diffusive flux can thus be written as shown in equation (16) where D_{diff} is the catalyst layer diffusivity, assumed to be dependent on temperature and relative humidity [7], h_{CL} is its thickness and L_x is the diffusion length.

$$q_{Ptloss} = -D_{diff} \frac{c_{Pt}^{2+}}{L_x h_{CL}} \tag{16}$$

$$D_{diff} = D_o \left(\frac{T}{T_0}\right)^2 \left(\frac{RH}{RH_0}\right)^2 \tag{17}$$

Finally, material balances are necessary to complete the model, describing the variation over time of oxide coverage, platinum concentration, and particle radius. The equations are taken from the literature [7] neglecting the reaction rates which are not included in this model.

The platinum concentration material balance includes anodic and chemical dissolution, together with the platinum loss in the membrane:

$$\varepsilon \frac{dc_{Pt^{2+}}}{dt} = 4\pi \sum_i {r_{Pt}^i}^2 n_{Pt}^i \left(r_{dis}^i + r_{chem}^i\right) \; - \varepsilon \, q_{PtLoss} \tag{18}$$

The electrode porosity ε represents the volume fraction of the ionomer inside the catalyst layer, which is the volume where the platinum can actually dissolve.

The oxide coverage balance is composed of two terms: the first one depends on reaction rates which involve Pt oxide, namely oxidation and chemical dissolution, the second one takes into account the change in the oxide coverage due to the change of particle size.

$$\frac{d\theta_{PtO}^i}{dt} = \left(\frac{r_{ox}^i - r_{chem}^i}{\Gamma_{max}}\right) - \left(\frac{2\theta_{PtO}^i}{r_{Pt}^i}\right) \frac{dr_{Pt}^i}{dt} \tag{19}$$

Reaction rates are divided by Γ_{max}, which is the number of moles of active sites per unit of platinum area.

As previously said, reaction rates change with particle radius, leading to different values of oxide coverage. Hence, one oxide material balance for each particle group will be necessary.

Finally, Pt particle radius variation (equation (19)) is affected only by anodic and chemical dissolution reaction. Obviously, a separate balance is necessary for each particles group, which is characterized by different reactions rates and different radius evolution over time.

$$\frac{dr_{Pt}^{i}}{dt} = -\frac{M_{Pt}}{\rho_{Pt}}\left(r_{dis}^{i} + r_{chem}^{i}\right) \tag{20}$$

As a whole, 2N+1 material balances are needed, where N is the number of particles groups. Increasing the groups number, the PRD is better approximated, but the computational time also increases significantly.

At first, parameters where taken from the literature [7] (Table 4), in order to validate the model.

Parameter	**Symbol**	**Value**	Unit	
Reference equilibrium potential	Φ_{dis}^{ref}	1,188	V	[7]
Reference oxidation equilibrium potential	Φ_{ox}^{ref}	0,98	V	[7]
Anodic dissolution reference kinetic constant	k_{dis}^{ref}	1E-10	$mol\ cm^{-2}$	[7]
Oxidation kinetic constant	k_{ox}	1,4E-11	$mol\ cm^{-2}$	[7]
Chemical dissolution kinetic constant	k_{chem}	3E-24	$mol\ cm^{-2}$	[7]
Transfer coefficient	α_{a1}	0,3	-	[7]
Transfer coefficient	α_{c1}	0,5	-	[7]
Transfer coefficient	α_{a2}	0,35	-	[7]
Transfer coefficient	α_{c2}	0,5	-	[7]
Platinum Oxide interaction energy	ω_{PtO}	27000	$J\ mol - 1$	[7]
Platinum surface tension	σ_{Pt}	0,237	$mJ\ cm^{-2}$	[7]
Platinum oxide surface tension	σ_{PtO}	0,1	$mJ\ cm^\wedge - 2$	[7]
Chemical potential	$\Delta\mu_{PtO}^{ref}$	-42,3	$kJ\ mol^{-1}$	[7]
Reference proton concentration	$c_{H^+,ref}$	0,001	$mol\ cm^{-3}$	[7]
Reference platinum concentration	$c_{Pt^{2+},ref}$	0,001	$mol\ cm^{-3}$	[7]
Maximum Pt surface coverage	Γ_{max}	2,18E-09	$mol\ cm^{-2}$	[7]
Electrode porosity	ε	0,3	-	[14]
Fitting parameter RH	ϑ	1,7	-	[7]
Reference relative humidity	RH_0	1	%	[7]
Reference temperature	T_0	80	°C	[7]

Table 4 - Parameters from the literature

3.2. Numerical implementation

The model is implemented with Matlab, and the differential equations system is solved with the ODE solver *ode15s*, which is used to solve stiff differential equations. It is a variable-step, variable-order (VSVO) solver based on the numerical differentiation formulas (NDFs) of orders 1 to 5. Optionally, it can use the backward differentiation formulas (BDFs) that are usually less efficient.

The coverage starting condition was set to zero, while the Pt concentration starting condition was calculated as the equilibrium concentration at the initial potential. Radius and concentration values resulting from the system of differential equations were bounded below to zero.

3.3. Model validation

In order to validate the model, all parameters were firstly taken from Schneider et al. [7], as well as the initial PRD. Parameters value are those shown in Table 4, while the initial PRD follows a normal distribution with 8 particle groups (few groups were sufficient as no high accuracy was needed in the validation phase) and a mean radius of 5.5 nm, as shown in Figure 15.

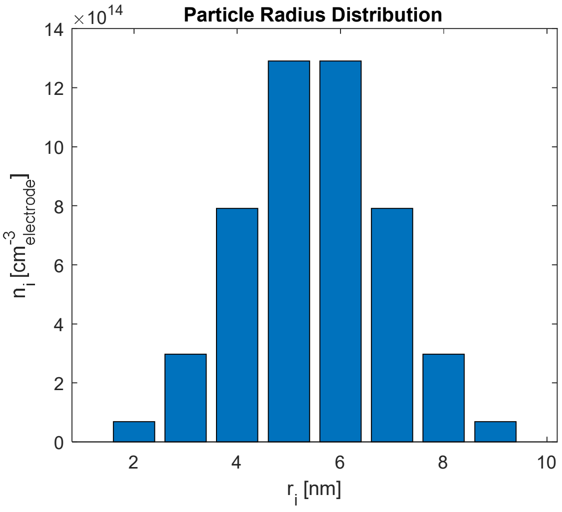

Figure 15 - Particle Radius Distribution used for model validation

A basic potential profile (a trapezoidal wave between 0.6 and 0.95 V, holding each potential step for 2.5s, and with a Scan Rate of 0.7 V/s during potential sweep) was simulated, and the operating temperature was set to 80°C. The resulting Oxide coverage, anodic dissolution reaction rates, platinum concentration and flux into the membrane were compared with those found in the literature (Figure 16). Although the model presents some differences with respect to the one proposed by Schneider (mainly it leaves out carbon corrosion, place exchange and cathodic dissolution and limits the maximum oxide coverage value to one), the results match very well. In the simulated potential range carbon corrosion and place exchange are not favoured indeed, and also because of short dwell times, oxide coverage values are much lower than one.

These results are also really helpful to understand the mechanisms leading to platinum dissolution and ECSA loss.

In Figure 16.a.2 the oxide coverage profile for different particle groups is shown. As previously explained, the coverage assumes different values for particles with different radius, as the equilibrium potential depends on it. In particular, smaller particles will be more oxidized.

It's worth highlighting what is shown in Figure 16.b.2, where the anodic dissolution rates are plotted for different particle radius and the Ostwald ripening mechanism can be easily observed. The smallest radius particle group (2 nm) has the highest dissolution reaction rate, always with positive values. For increasing radius, the reaction rate is lower, with a negative peak during the decreasing potential sweep, while the biggest radius particle group has a small positive peak during the increasing potential sweep but assumes negative values as soon as Pt concentration starts to grow (Figure 16.c.2). This implies that platinum dissolves mainly from smaller particles and re-deposits mainly on bigger particles, which causes, over a longer degradation period, an overall shift in the PRD toward larger particles, and eventually an ECSA loss due to the effect of Ostwald ripening.

In Figure 16.c.2 the platinum concentration and its flux into the membrane is represented, which is relevant during the holding period at 0.95V, when the Pt concentration rises. As previously explained, platinum will then redeposit in the membrane where it will be not active anymore.

A similar potential profile was than simulated with different operating temperatures, namely 60°C, 80°C and 90°C. As the diffusive constant is dependent on temperature, different profile of platinum concentration and flux into the membrane were obtained, which are plotted and compared with Schneider results in Figure 17, obtaining a very good agreement. Moreover, different potential profiles were simulated and the results in term of platinum concentration and flux into the membrane are compared with literature results in Figure 18.

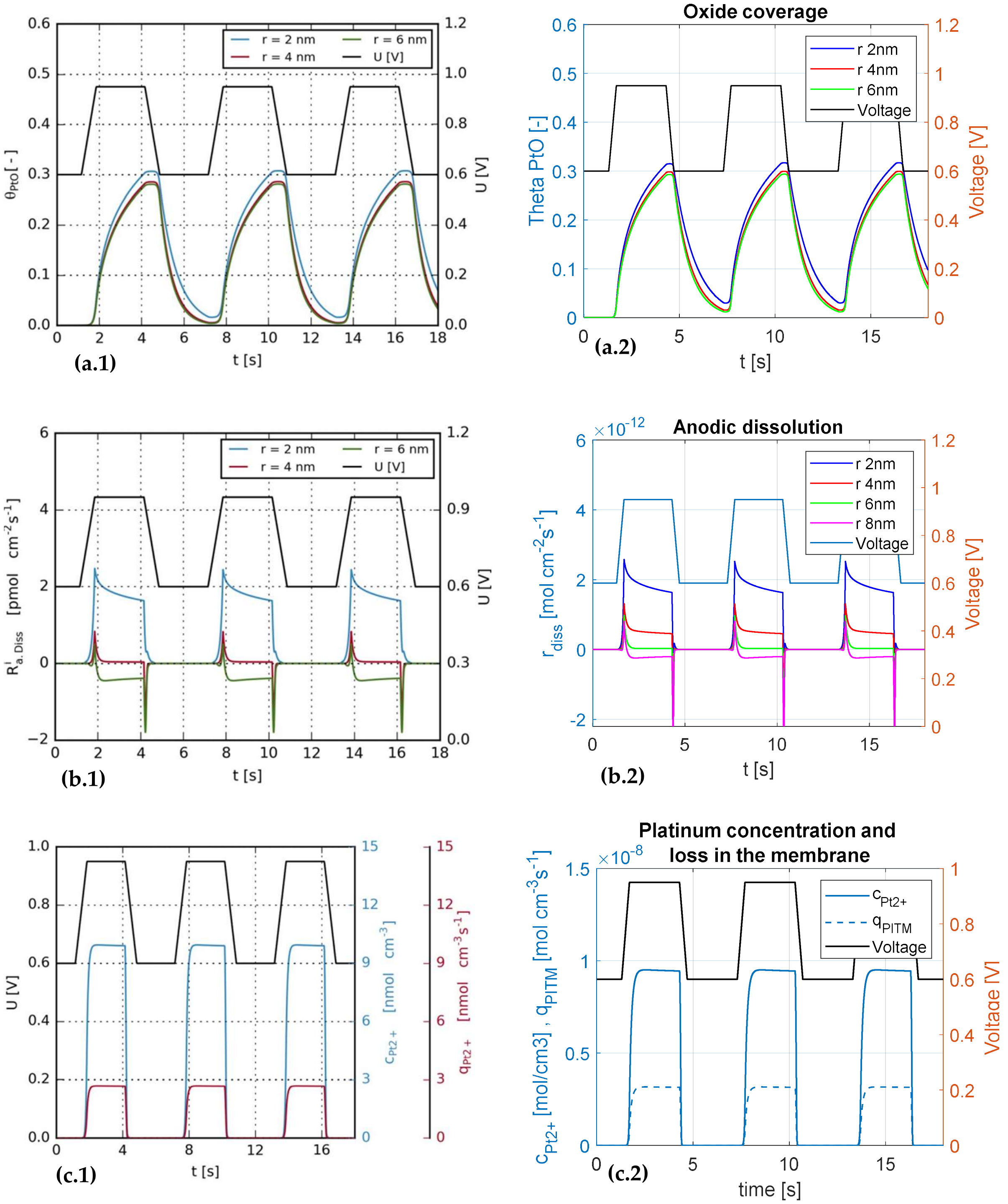

Figure 16 - Basic profile simulated results compared with literature results [7] (a.1) oxide coverage from the literature; (a.2) simulated oxide coverage; (b.1) anodic dissolution reaction rates from the literature; (b.2) simulated anodic dissolution reaction rates; (c.1) platinum concentration and loss into the membrane from the literature; (c.2) simulated platinum concentration and loss into the membrane

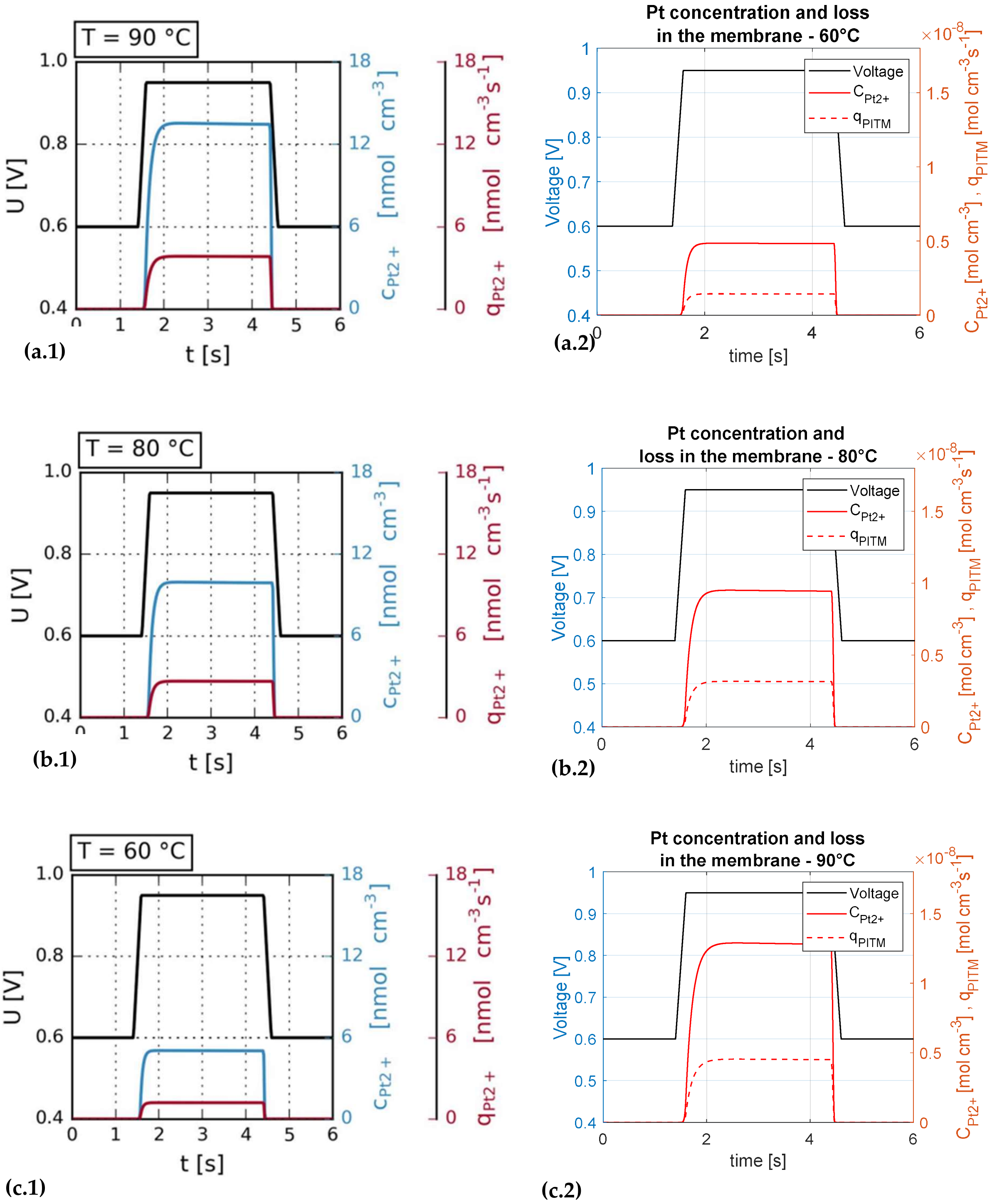

Figure 17 - Basic profile simulated results compared with literature results [7]: platinum concentration and flux into the membrane at different operating temperatures: (a.1) 90°C data from the literature; (a.2) 90°C simulated data; (b.1) 80°C data from the literature; (b.2) 80°C simulated data; (c.1) 60°C data from the literature; (c.2) 60°C simulated data

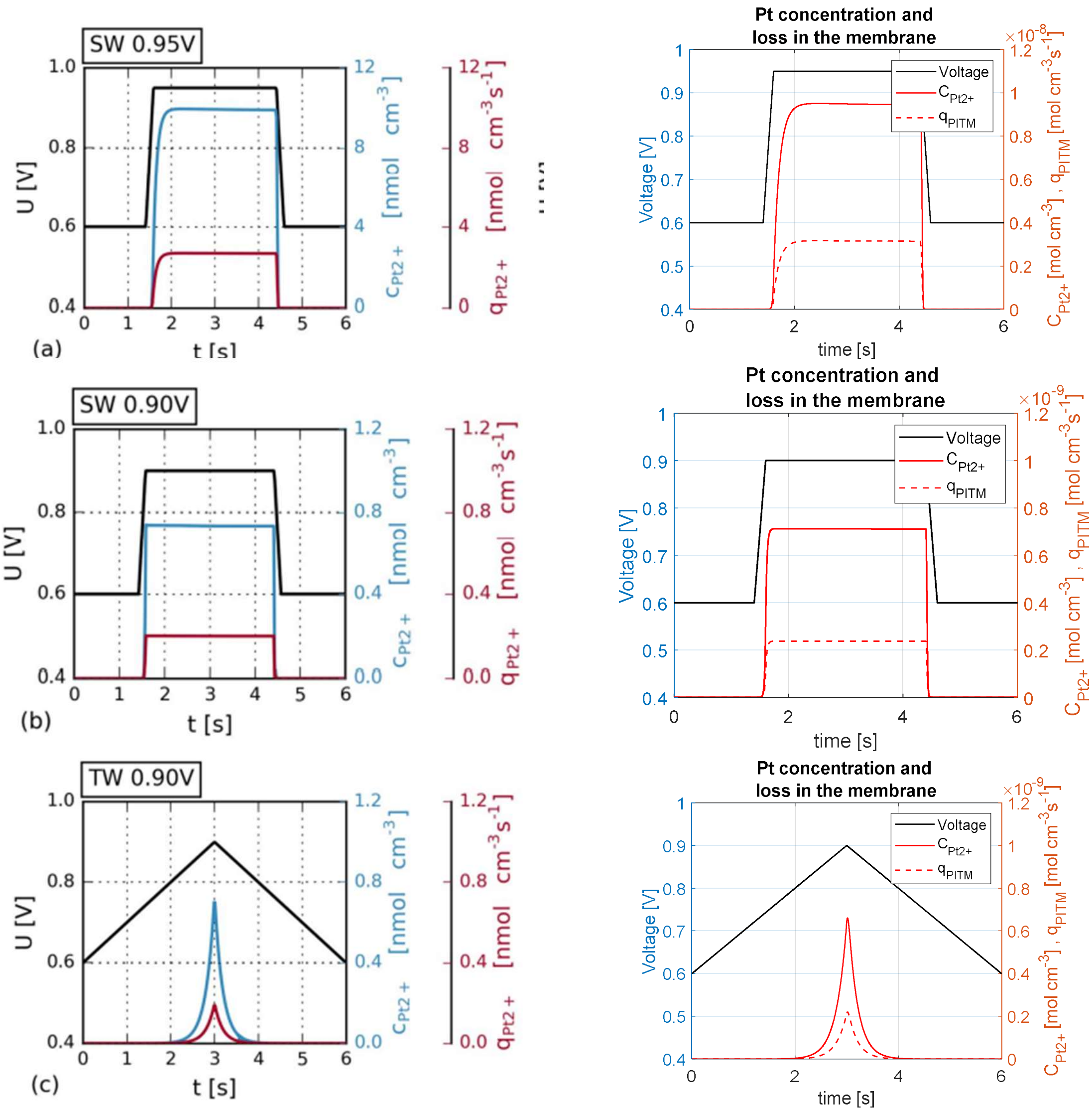

Figure 18 – Different basic profiles simulated results compared with literature results: platinum concentration and platinum flux in the membrane

A longer degradation tests were then simulated repeating the basic potential profile shown before for a really high cycle number.

During the simulation, if a particle group reaches a minimum value (set to 0.7 nm), it gets erased from the PRD, and a corresponding amount of Pt mass is added to dissolved platinum (increasing the concentration) in order to respect mass conservation.

The results in terms of ECSA loss and radius evolution in time for each group are shown and compared with the literature results in Figure 19.

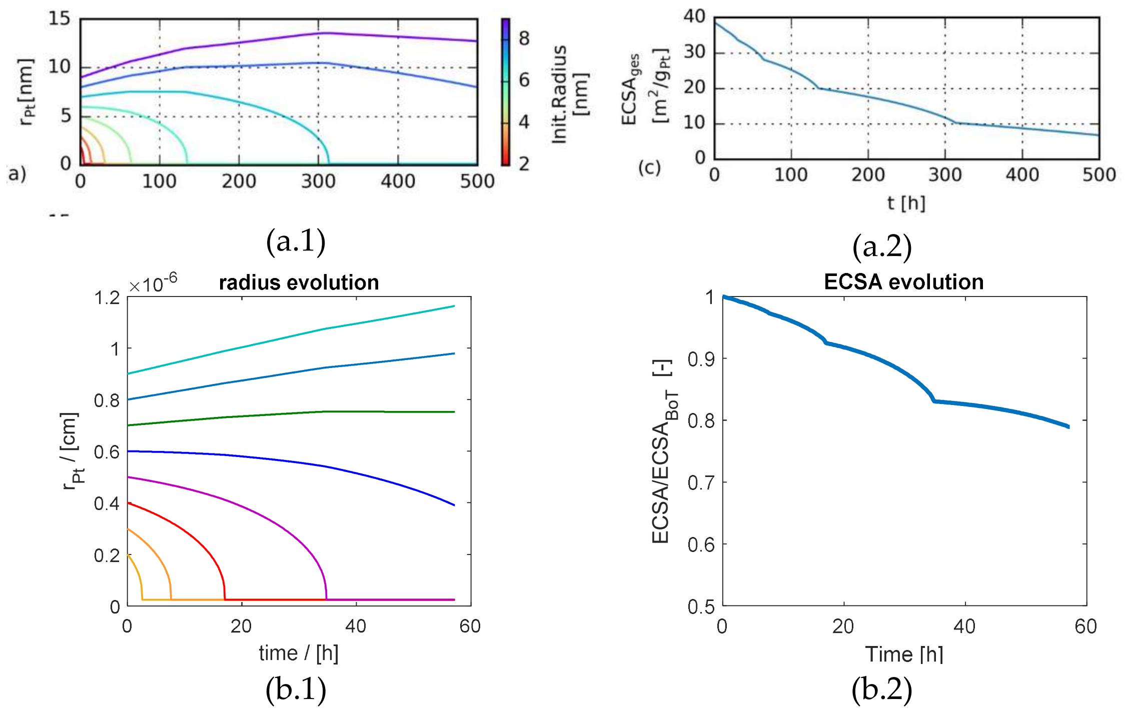

(a.1)

(a.2)

(b.1)

(b.2)

Figure 19 - Degradation test simulation: (a.1) radius evolution from the literature; (a.2) ECSA loss from the literature [7]; (b.1) radius evolution simulated; (b.2)ECSA loss simulated

3.4. Oxides model calibration with experimental data

The oxidation parameters, in particular the kinetic constant k_{ox}, the interaction energy ω_{PtO} and the reference equilibrium potential Φ_{ox}^{ref} were calibrated with experimental data. Some specific tests were used to investigate oxide formation, performed with an operating temperature of 70°C, which is almost equal to the temperature used in the Accelerated Stress Tests (described in the following chapter), i.e. 71°C.

Cyclic voltammetries (CV) were performed with different Upper Potential Limit (UPL), varying from 0.6V to 0.95V and different ScanRate (SR), (0.1 V/s, 0.25 V/s and 0.5 V/s). Some of these are shown in Figure 20.

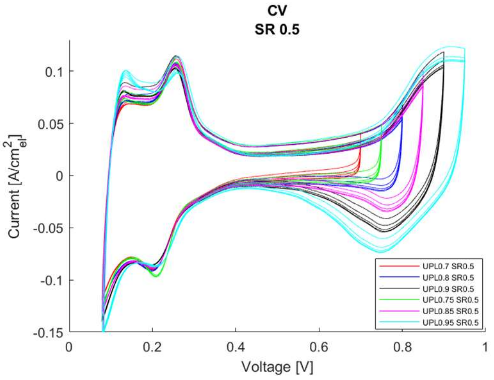

Figure 20 - CV with ScanRate 0.5 V/s

Some peculiar Linear Sweep Voltammetries were also performed, which will be referred to as Holding LSVs. The potential was raised up to a certain UPL, then kept constant for a certain holding time and then decreased linearly with a SR of 0.1 V/s. During the decreasing potential sweep, the current was detected and plotted against the potential (Figure 21, Figure 22). As the used scan rate is much higher than the one used in the standard LSV described in 2.4.1., it is possible to detect the current due to oxides reduction and platinum desorption reaction, as shown in Figure 21 and Figure 22.

Integrating this current from the maximum potential value to the local minimum (in absolute term) of the double layer current (around 0.4 V), it is thus possible to measure the oxide coverage, according to the following formula:

$$\theta_{PtO} = \frac{\int_{E_{dl}}^{E_{max}} (i - i_{DL})\, dV}{\sigma_m L_{Pt}\, n_e\, SR\, ECSA} \qquad (21)$$

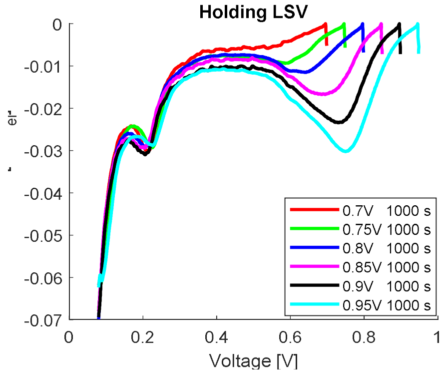

Figure 21 - Holding LSV with 1000s holding time

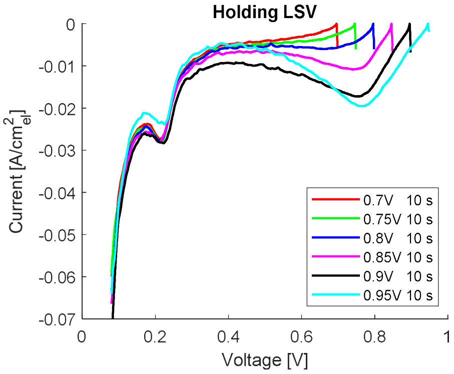

Figure 22 - Holding LSV with 10s holding time

This test was performed for different UPL, varying from 0.7V to 0.95V with a step of 0.5 V, and different holding time (1s, 10s, 100s, 1000s).

Both CVs and Holding LSVs were then reproduced with the model and the simulated results were compared with the experimental ones. To do so, two quantities were considered: for CVs the reduction peak potential E_{red}^{exp}, i.e. the potential corresponding to the maximum current value, while for Holding LSVs the measured oxides coverage θ_{PtO}^{exp} was compared with the simulated value θ_{PtO}^{model}. The errors between the experimental and the simulated quantities were then calculated, and the oxidation parameters were calibrated in order to minimize these errors.

$$err_{\%}^{\theta_{PtO}} = \frac{\theta_{PtO}^{exp} - \theta_{PtO}^{model}}{\theta_{PtO}^{exp}} * 100 \tag{22}$$

$$err_{\%}^{E_{redpeak}} = \frac{E_{red}^{exp} - E_{red}^{model}}{E_{red}^{exp}} * 100 \tag{23}$$

The oxide coverage obtained with calibrated parameters are shown in Figure 23, compared with the experimental values, while simulated and experimental CVs are shown in Figure 23 (only CVs with UPL higher than 0.85 are reported, as for lower values no relevant oxides formation is detected). The model is able to reproduce the increase of oxide coverage with increasing holding time and increasing potential values, while it slightly underestimates it for low potential values.

Cyclic Voltammetries cannot be exactly reproduced, as the platinum adsorption and desorption, as well as the double layer charging and discharging, are not included in the model. For this reason the aim was not to obtain the exact CV shape but to reproduce oxide formation and reduction in a potential range as close as possible to the experimental one. The shape of simulated CVs differs from the experimental one especially in the oxide reduction peak, which is much narrower. In order to obtain a better reproduction of experimental CVs, a more complex model would be necessary, i.e. with a two steps oxidation, which includes an intermediate oxide (i.e. PtOH).

The model is able to reproduce the increase in currents values due to different Scan Rates. To the author's knowledge no model is available in the literature that correctly reproduces voltammograms in a wide range of scan rates as the ones analyzed in this work.

The oxidation parameters as obtained from calibration are shown in Table 5.

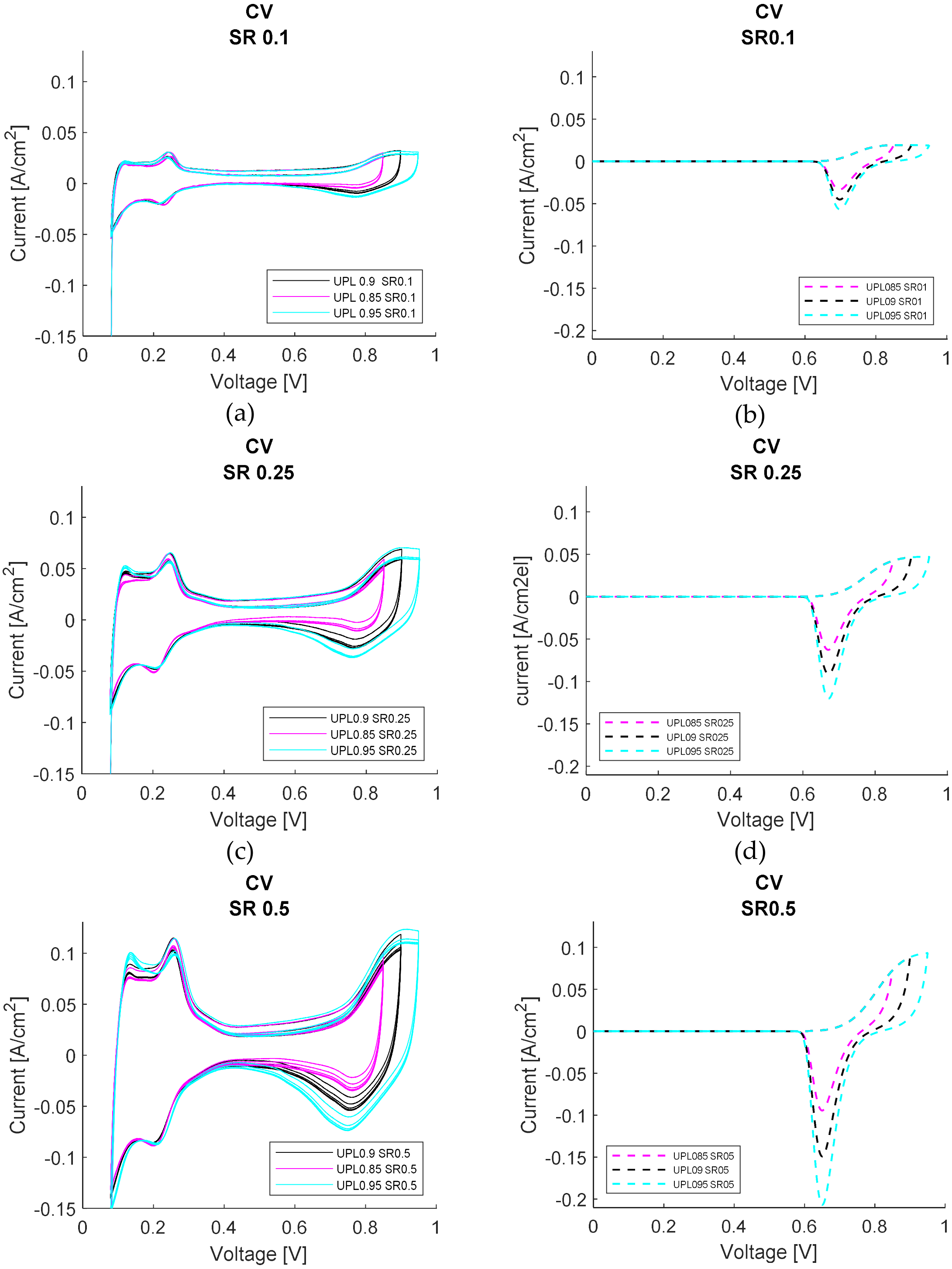

(a) (b) (c) (d) (e) (f)

Figure 23 - CV simulated VS experimental with different Scan Rate
(a) SR=0.1 V/s experimental; (b) SR=0.1 V/s simulated;
(c) SR=0.25 V/s experimental; (d) SR=0.25 V/s simulated;
(e) SR=0.5 V/s experimental; (e) SR=0.5 V/s simulated

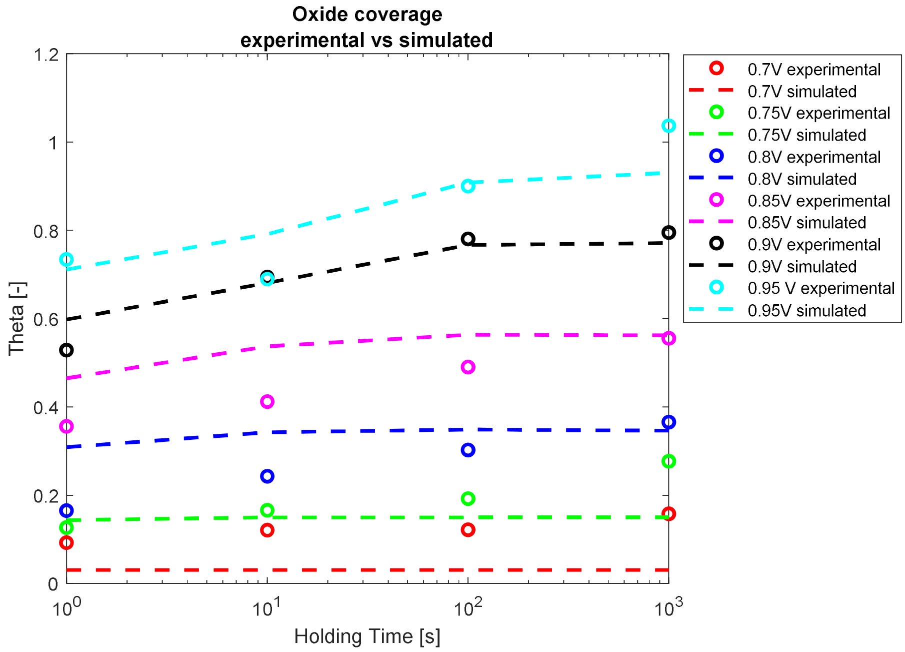

Figure 23 - Oxide coverage: experimental VS simulated

Parameter	**Symbol**	**Value from literature**	**Value from calibration**	**Unit**
Reference oxidation equilibrium potential	Φ_{ox}^{ref}	0,98	0,99	V
Oxidation kinetic constant	k_{ox}	1,4E-11	8E-10	$mol\ cm^{-2}$
Transfer coefficient	α_{a2}	0,35	0,35	-
Transfer coefficient	α_{c2}	0,5	0,5	-
Platinum Oxide interaction energy	ω_{PtO}	27000	26000	$J\ mol^{-1}$

Table 5 - Calibrated oxidation parameters

3.5. Dissolution model calibration with experimental data

Dissolution parameters, namely the kinetic constant k_{dis} and the transfer coefficients α_{a1} and α_{c1} were fitted on electrocatalyst AST experimental data taken from ref [11].

The electrocatalyst AST is defined by the US Department Of Energy (DOE) [15] to assess cathode electrocatalyst durability. A voltage square wave is performed between 0.6 V and 0.95 V, with a holding time of 3s and a rise time of 0.5s, as shown in Figure 24. The voltage range is similar to the one which is expected in automotive operation and should maximize catalyst degradation and minimize carbon corrosion. The cell is fed with hydrogen at the anode and nitrogen at the cathode, the temperature is set to 80°C and the streams are fully humidified. Test specifications are summarized in Table 6.

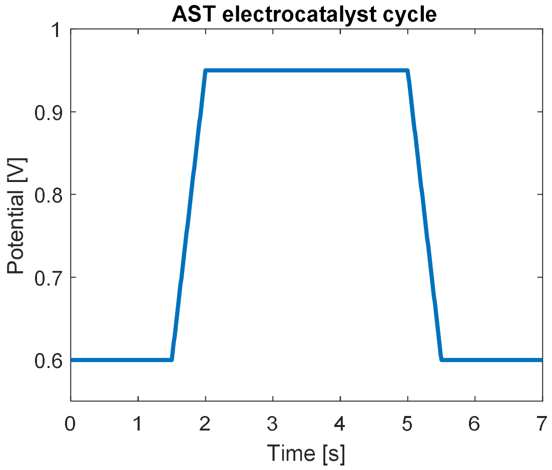

Figure 24 - AST electrocatalyst base cycle

AST electrocatalyst	
Cycle	From 0.6V (3s) to 0.95V (3s) with rise time of 0.5 s
Cycles number	50000
Temperature	80°C
RH	100%
Feed Gases	H2/N2
Pressure	atmospheric

Table 6 - AST electrocatalyst specifics

The test was simulated varying anodic dissolution parameters in order to reproduce the ECSA loss experimental trend. The result is shown in Figure 25, while the calibrated parameters are shown in Table 7.

Parameter	**Symbol**	**Value**	**Unit**
Anodic dissolution kinetic constant	k_{dis}^{ref}	$5 * 10^{-9}$	$mol\ cm^{-2} s^{-1}$
Transfer coefficient	α_{a1}	0.5	-
Transfer coefficient	α_{c1}	0.5	-

Table 7 – Anodic dissolution parameters

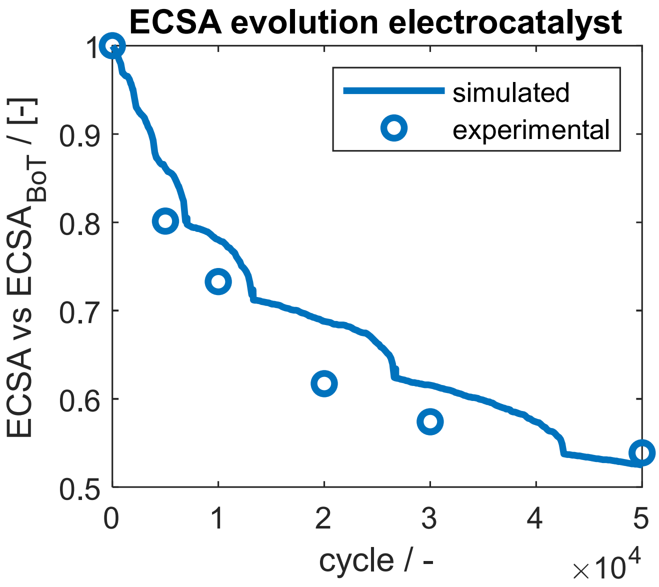

Figure 25 - ECSA evolution of AST electrocatalyst, experimental vs model results

3.6. Conclusion

A zero-dimensional model was developed, starting from the work of Schneider et al. [7]. The aim is to simulate the platinum dissolution in the cathode catalyst layer and the consequent ECSA loss as a function of the potential profile which is imposed to the cell. The model is built to run in a potential range corresponding to normal operating conditions (below 0.95 V): reactions which take place at higher potentials are neglected. The Particle Radius Distribution (PRD) is discretized with a finite number of particle groups, characterized by the radius and the particle number. All the particles of the same group undergo the same transition they either shrink or grow, and they cannot move to other groups.

The model inputs are potential profile, which is the driving force of the whole degradation process, operating conditions (temperature and RH), and initial Particle Radius Distribution (PRD). The model is composed with reaction rate equations and material balances, giving as outputs reaction rates, oxide coverage, platinum concentration in the ionomer, PRD and ECSA evolution in time. The reactions considered in the model are the following: anodic dissolution, platinum oxidation, oxide chemical dissolution and platinum flux in the membrane.

Simulations by Schneider were correctly reproduced with the original parametrization and perfect consistency is reported. The oxidation parameters were calibrated with experimental data, namely cyclic voltammetries and holding linear sweep voltammetries, that allow to investigate oxide formation. Anodic dissolution parameters were calibrated with the results of the electrocatalyst accelerated stress test.

4 Experimental results

In this chapter the design of the Accelerated Stress Tests (ASTs) and the experimental results will be presented, aiming at obtaining insight into the degradation process and refining the model. Some preliminary simulations of the experimental results with the model presented in Chapter 3 will be shown.

4.1. Accelerated Stress Tests design: an overview

The starting point to design the degradation tests was the IDFAST Low Power AST. As described in 2.5.1, it is designed to be performed in galvanostatic mode, and the base current profile is a square wave ranging between the current values which correspond to 0.85 V and 0.7 V at BOT. At the end of each AST cycle a short stop is introduced. The results of this AST were taken from ref [11].

Starting from this protocol, several degradation tests have been designed, thoroughly described in the following paragraphs. Here is a brief introduction to explain the approach used to define them, which is also outlined in the block diagram shown in Figure 26.

As explained later, each AST is performed simultaneously on different samples thanks to the Multi-0G hardware. The shape of the potential profile, which characterizes the AST, is the same for all the samples, while the imposed potential values are different. The features of different ASTs and samples are summarized in Table 8.

AST 2 was designed to investigate the ageing effect of short stops. To this aim, a square wave potential profile without short stops was used, while in the last part of the test short stops were introduced again.

Finally, AST 3 and 4 were used to investigate the effect of the minimum potential on the degradation. In AST 3 the Lower Potential Limit (LPL) imposed during the cycling was varied. In AST 4 the same UPL and LPL were used in the cycling, but a final step at different Holding Potential (HP) was introduced.

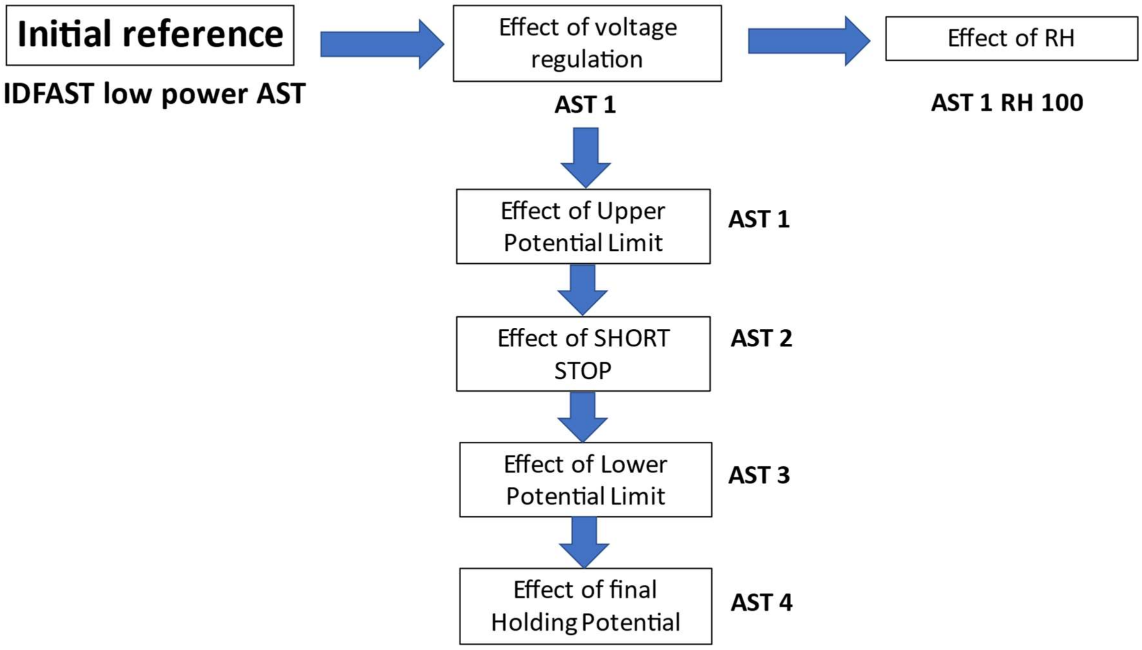

Figure 26 – Overview of the experimental campaign: parameters evaluated by designing specific accelerated stress tests

TEST	REGULATION	SAMPLE	UPL [V]	LPL [V]	Short stop / final holding
Low power	galvanostatic	1	0.85 at BoT *	0.7 at BoT *	Short stop ≈ 0 V
AST 1	potentiostatic	1	0.85	0.7	Short stop ≈ 0 V
		2	0.9	0.7	
AST 1 RH100	potentiostatic	1	0.85	0.7	Short stop ≈ 0 V
AST 2	potentiostatic	1	0.85	0.7	Short stop ≈ 0 V only in the final part of the test
		2	0.9	0.7	
AST 3	potentiostatic	1	0.85	0.7	-Not introduced
		2	0.85	0.6	
		3	0.85	0.4	
AST 4	potentiostatic	1	0.85	0.7	Final holding 0.7 V
		2	0.85	0.7	Final holding 0.6 V
		3	0.85	0.7	Final holding 0.4 V
		4	0.85	0.7	Final holding 0.2 V

*The current value corresponding to this potential value at BOT was imposed

Table 8 -Accelerated stress tests features

4.2. Design of Accelerated Stress Tests and experimental results

AST 1

As said before, AST 1 is a variation of the IDFAST Low Power AST. Potential was imposed instead of current to understand whether a potentiostatic regulation can be used instead of a galvanostatic one obtaining an equivalent degrading effect. Moreover, different values of UPL were used for different samples, to indagate the effect of potential limits.
The AST cycle (Figure 27) is composed with a of 30 s step at the UPL, followed by a step of 12 s at the Lower Potential Limit (LPL); these two steps are repeated 6 times and followed by 30 s at the UPL; finally, a short stop of 110 s at nearly 0 V is introduced, consequence of the interruption of the air feeding. The UPL was set to 0.85 V for sample 1 and 0.9 V for sample 2, while LPL was set to 0.7 V for both samples. Sample 1 differs from the IDFAST low power AST only for the regulation.

The test is performed with H_2/air feedings and constant stoichiometries. Relative humidity is set to 70% at the anode and 60% at the cathode, as in the IDFAST low power test. The operating conditions are summarized in Table 9.

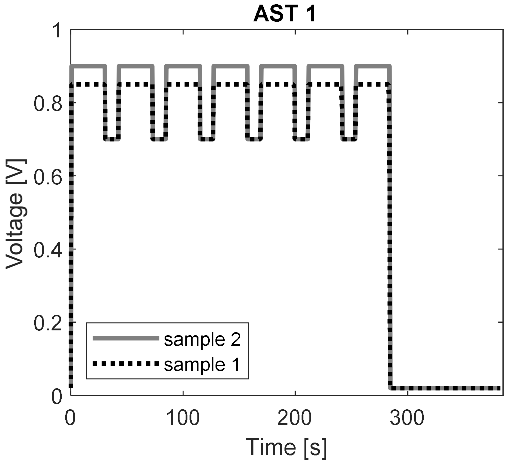

Figure 27 - AST 1 Voltage profile

Parameters	Unit	Values
Cell temperature	°C	71
RH anode	%	70
RH cathode	%	60
Flow rate anode	-	Fixed at $\lambda = 8$
Flow rate cathode	-	Fixed at $\lambda = 20$
Oxygen percentage on dry flow rate	%	20.9
Pressure anode	kPa	190
Pressure cathode	kPa	140

Table 9 - AST 1 operating conditions

AST 1 was performed for 1200 cycles, stopping every 200 cycles to perform the characterization tests.

Cyclic Voltammetries (CVs) are shown in Figure 28, while the resulting ECSA trends are shown in Figure 29, compared with the one of IDFAST low power AST.

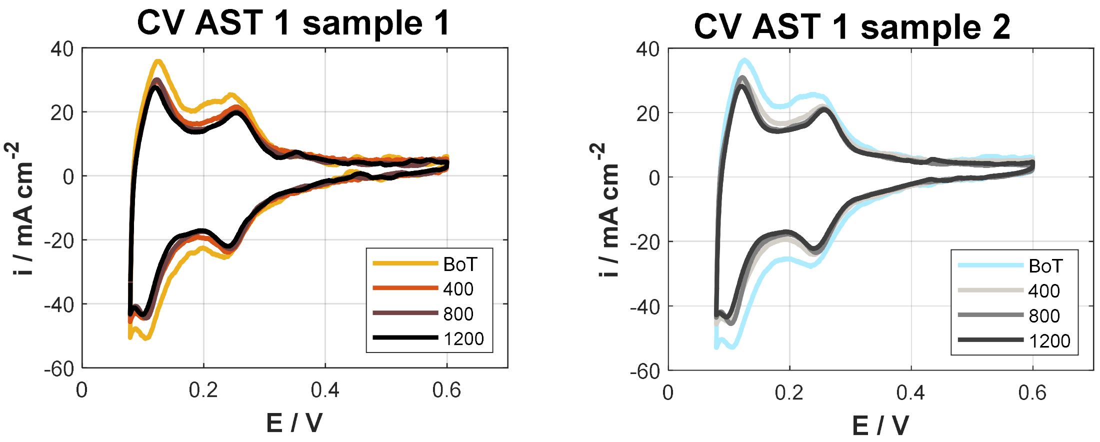

(a) (b)

Figure 28 - CV AST 1: (a) sample 1 [0.7-0.85V] (b) sample 2 [0.7-0.9V]

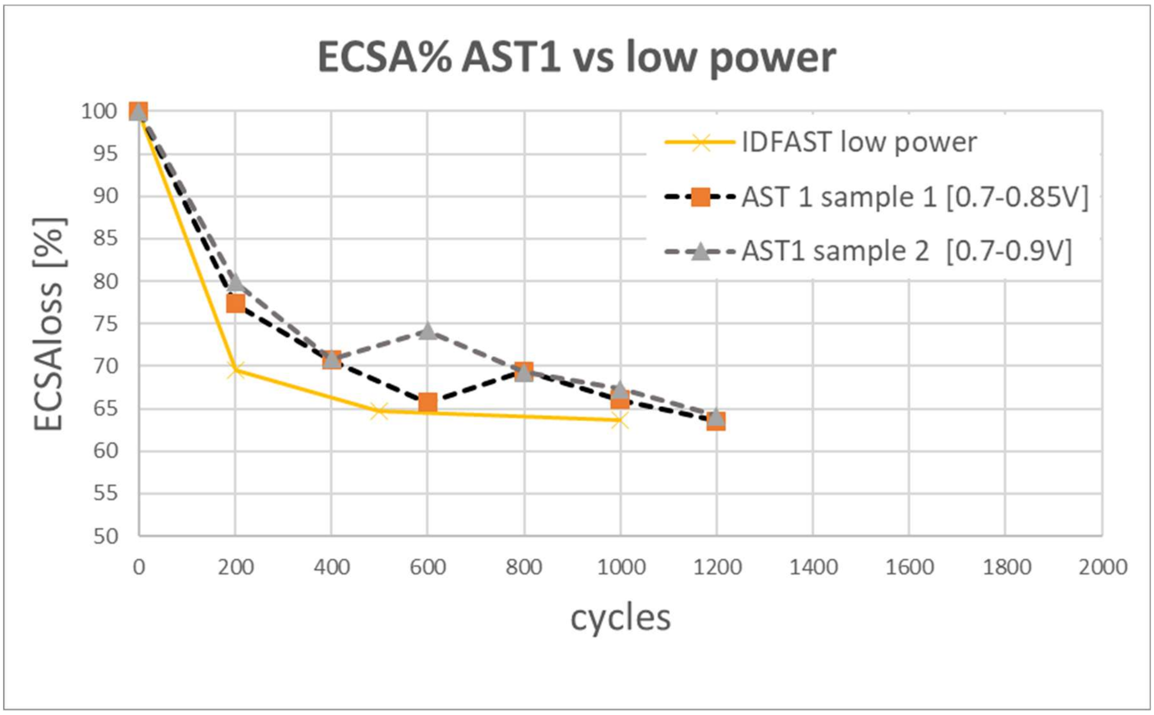

Figure 29 - ECSA evolution AST 1 vs AST low power

A rapid and considerable decrease of the ECSA can be observed (Figure 29), which drops below 80% of the initial value in the first 200 cycles for both samples, and then stabilizes around a value of 65%. This is quite evident also looking at the CV plots (Figure 28): the one performed after 400 cycles is considerably different from the BoT, while the following ones show a further area reduction which is quite restrained. Two conclusions can be drawn from these results:

- The potentiostatic mode does not lead to a substantial difference in degradation. Indeed, IDFAST low power and AST 1 sample 1, which only differ in regulation, show quite similar ECSA trends, with a difference of 5-7%. A slighter lower impact was detected in potentiostatic rather than galvanostatic;
- The effect of different UPLs appears to be negligible, as the two samples of AST 1 show a similar ECSA trend.
  This is not consistent with the general knowledge available in the literature. Indeed a higher ECSA loss has been observed when imposing a higher UPL in standard electrocatalyst AST [16][17][18].

For both samples, the polarization curve performed at the end of the tests, with respect to the one performed at BoT, show a vertical shift in the low current region, as shown in Figure 30. This feature means that the voltage loss is mainly affected by the ECSA loss, and no other degradation phenomena affecting the low current region are occurring (as the increase of crossover and/or short-circuit current to due membrane thinning).

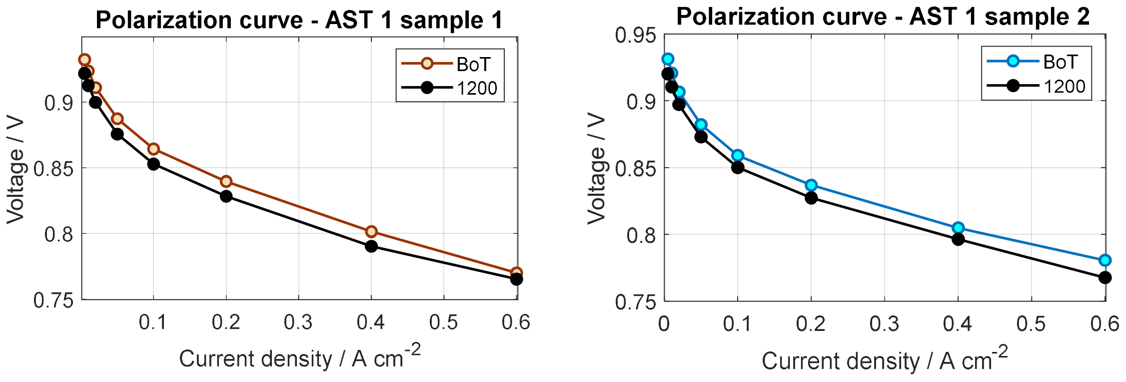

(a) (b)

Figure 30 - Polarization curve AST 1: (a) sample 1 [0.7-0.85V] (b) sample 2 [0.7-0.9V]

Current was also measured during the test execution, and its profile during two subsequent cycles performed on sample 1 is shown in Figure 31. During the AST cycle, a significative current reduction can be observed both during the single low voltage (high current) step, both among subsequent low voltage steps (from 1 to 6, Figure 31) in the AST cycle. A similar trend can be observed for the high voltage (low current) steps (from 7 to 13, Figure 31). However, the performance decrease is recovered after the short stop: no big differences are indeed observed among subsequent AST cycles.

This pattern is repeated for the entire test execution. Indeed, step 6 current is always considerably lower than the step 1 current, as shown in Figure 32

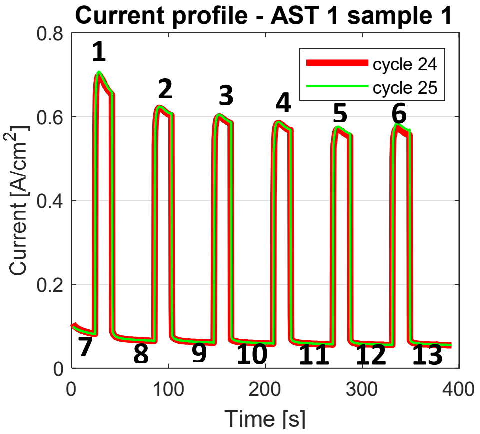

Figure 31 - Current profiles of AST 1 sample 1

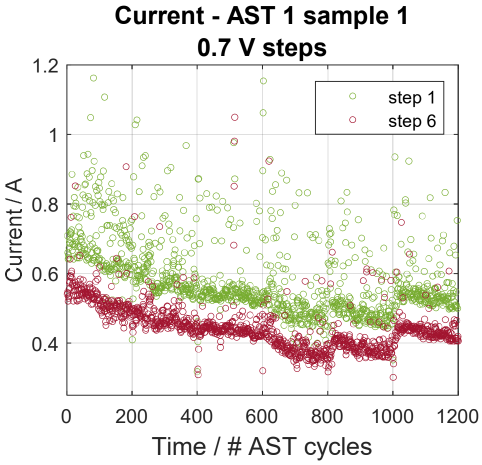

Figure 32 - Current of low voltage steps of AST 1 sample 1

This can be ascribed to the formation of an oxide on the platinum surface which is not completely reduced at 0.7 V and therefore keeps growing during the cycle, temporarily decreasing the catalyst active area. The performance recover after the short stop can be explained with a strong oxide reduction that takes place when the potential goes down to 0 V, making the catalyst surface active again. After many cycles a current reduction among different AST cycles could be observed, which can be attributed not only to an increasing oxide coverage but mainly to an irreversible performance decrease due to ECSA loss.

AST 1 RH 100

AST 1 was then performed increasing the relative humidity to 100% in order to see whether it has a significant effect on the degradation, but also to avoid secondary effects on performances linked to the humidification of the membrane.

The same potential profile of AST1 sample 1 was used, ranging between 0.7 V and 0.85 V and including the short stop. The operating conditions (Table 10) differs from AST 1 only in the relative humidity. The ECSA loss obtained with AST1 RH100 is really similar to the one obtained with AST 1 sample 1, as shown in Figure 33, meaning that relative humidity has a really limited impact on ECSA loss, , at least for values larger than 60%.

Parameters	**Unit**	**Values**
Cell temperature	°C	71
RH anode	%	100
RH cathode	%	100
Flow rate anode	-	Fixed at $\lambda = 8$
Flow rate cathode	-	Fixed at $\lambda = 20$
Oxygen percentage on dry flow rate	%	20.9
Pressure anode	kPa	190
Pressure cathode	kPa	140

Table 10 - AST 1 RH 100 operating conditions

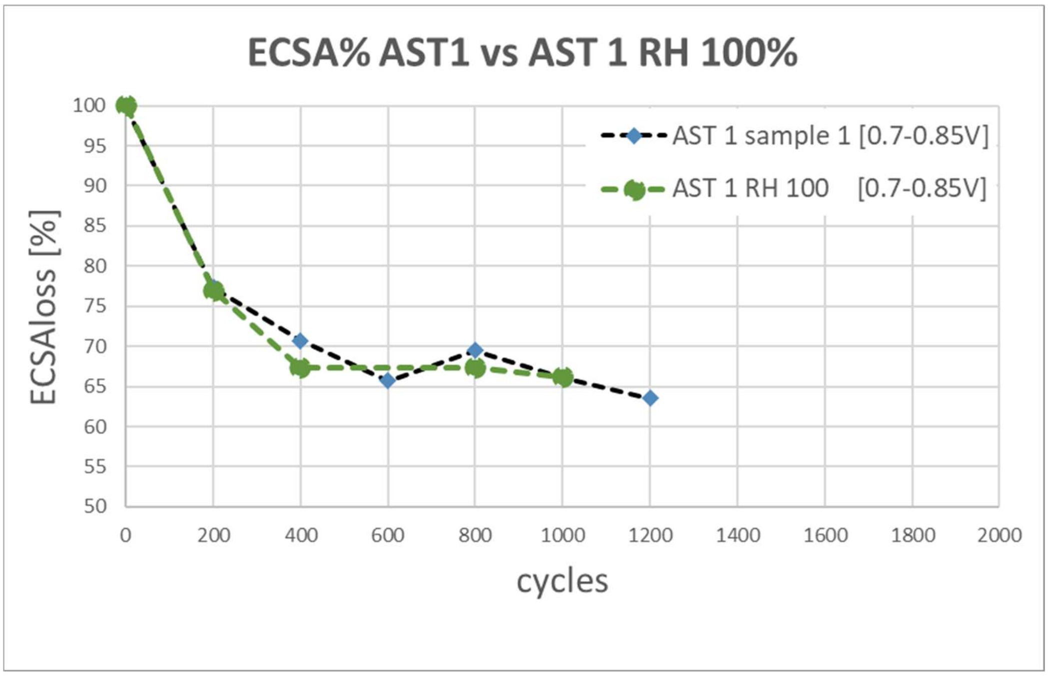

Figure 33 - ECSA evolution: AST 1 vs AST 1 RH 100%

AST 2

AST 2 was designed to separately investigate the effect of cycling and short stops. From previous results indeed, it is not clear whether the ECSA loss is mainly due to the cycling part of the potential profile or to the short stop or to the two of them.

In this test two different voltage profiles were used. The first one (Figure 34), used for the first 1200 cycles, is similar to the one used in AST 1 but without the final short stop. The AST cycle is composed with a step of 30 s at the UPL followed by a step of 12 s at the LPL, repeated for 6 times. The second one (Figure 35), used for the last 400 cycles, is the same used in AST 1. As a whole, 1600 cycles were performed, without short stops from 1 to 1200 (a short stop was introduced only every 200 cycles), and with short stops from 1201 to 1600.

The AST was performed simultaneously on two samples. On the first sample the UPL and the LPL were respectively 0.85 V and 0.7 V, on the second one 0.9 V and 0.7 V.

The test was performed with hydrogen/air feeding and constant stoichiometries. The operating conditions are shown in Table 11.

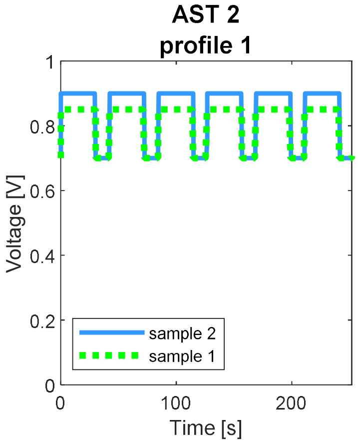

Figure 34 - AST 2 voltage profile 1 (used in the first 1200 cycles)

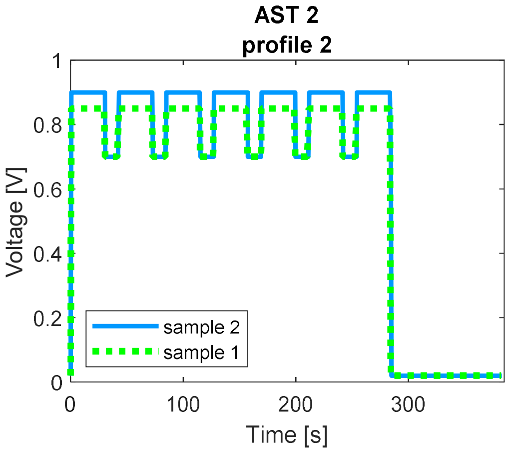

Figure 35 - AST 2 voltage profile 2 (used in the last 400 cycles)

Parameters	**Unit**	**Values**
Cell temperature	°C	71
RH anode	%	70
RH cathode	%	60
Flow rate anode	-	Fixed at $\lambda = 8$
Flow rate cathode	-	Fixed at $\lambda = 20$
Oxygen percentage on dry flow rate	%	20.9
Pressure anode	kPa	190
Pressure cathode	kPa	140

Table 11 - AST 2 operating conditions

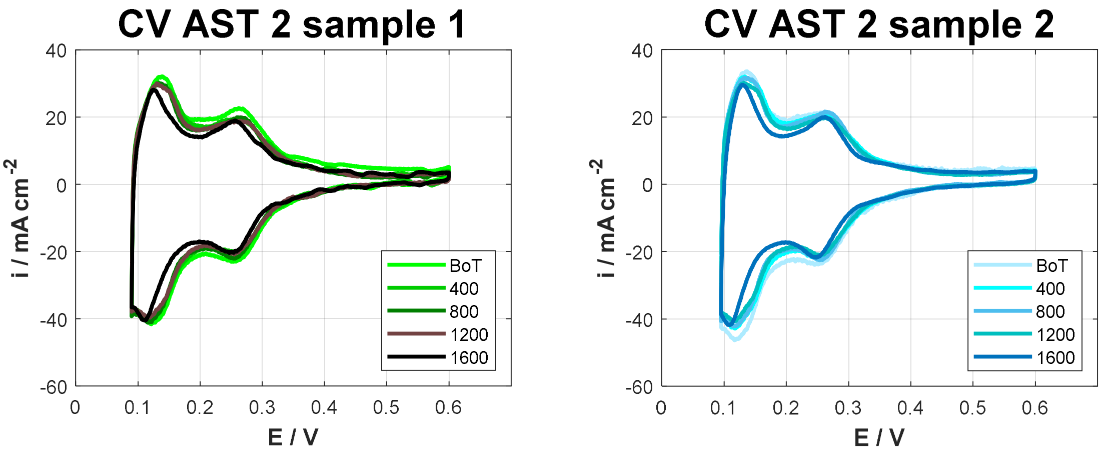

(a)

(b)

Figure 36 - CV AST 2: (a) sample 1 [0.7-0.85 V]; (b) sample 2 [0.7-0.9V].

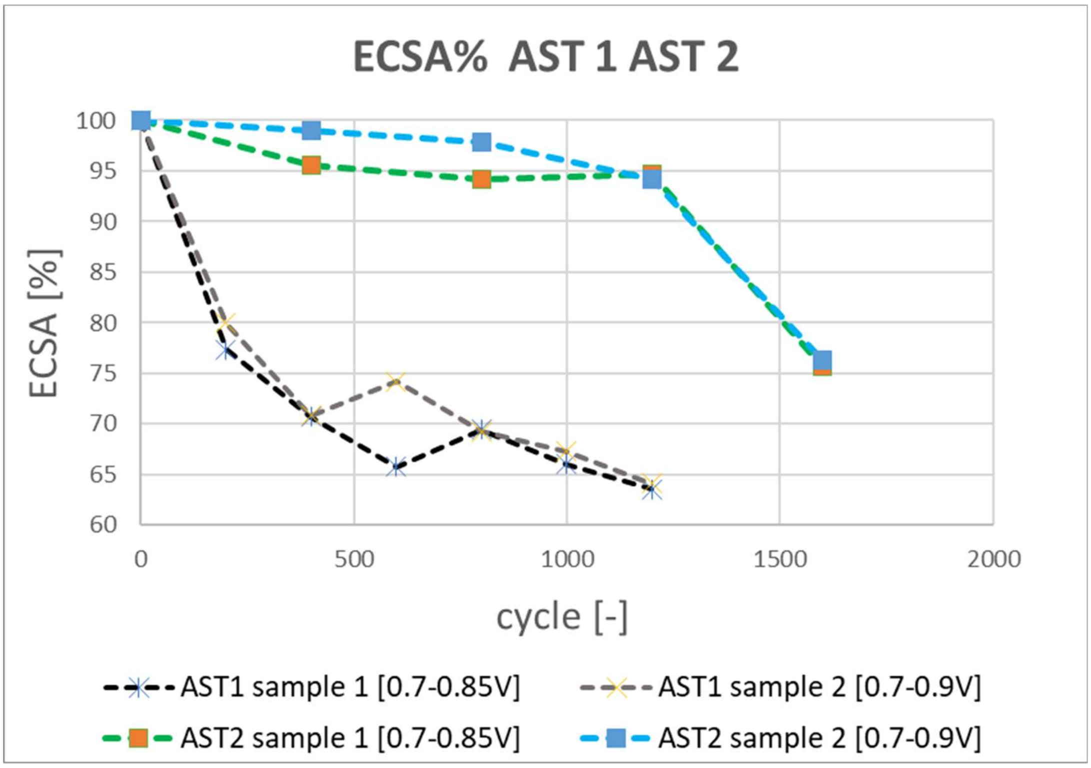

Figure 37 - ECSA evolution: AST 2 vs AST 1

The CV results are shown in Figure 36, and the resulting ECSA loss trends in Figure 37, compared with AST 1 results. Two significant remarks can be made:

- A really limited ECSA loss is observed up to 1200 cycles, meaning that that the cycling profile have a limited effect on degradation, while a significant decrease is measured in the last 400 cycles (the ECSA decreases down to 76%, similarly to the trend of AST 1 in the first cycles), meaning that the short stops have a much stronger effect. This is evident also looking at the CV plots (Figure 36), as the i-V curve measured after 1600 cycles, shows a significant drop with respect to the previous ones, which are instead more similar among themselves.
- The two samples, although going to different maximum potential values, show a similar ECSA trend (the minor degradation of sample 1 can be attributed to measurement uncertainty in the evaluation of ECSA). It is thus evident that going to potential values higher than 0.85 V does not have a significant effect on the degradation.

In Figure 38, some current profiles detected during subsequent cycles performed on sample 1 are shown, both during the first part of the test, without short stops (Figure 38a) and during the second part of the test, when short stops are introduced. Similar profiles can be observed also for sample 2.

In Figure 39 the current values of low voltage steps, detected during the test, are separately plotted for both samples. The steps number are defined as shown in Figure 38. In the first 1200 cycles, current values of different low voltage steps (Figure 39) are really close. Indeed, the current profile of the single cycle (Figure 38 a) show similar current values for subsequent steps at the same voltage. Nonetheless, during the test execution a progressive performance loss can be observed (Figure 39), which is almost completely recovered every 200 cycles when short stops are introduced.

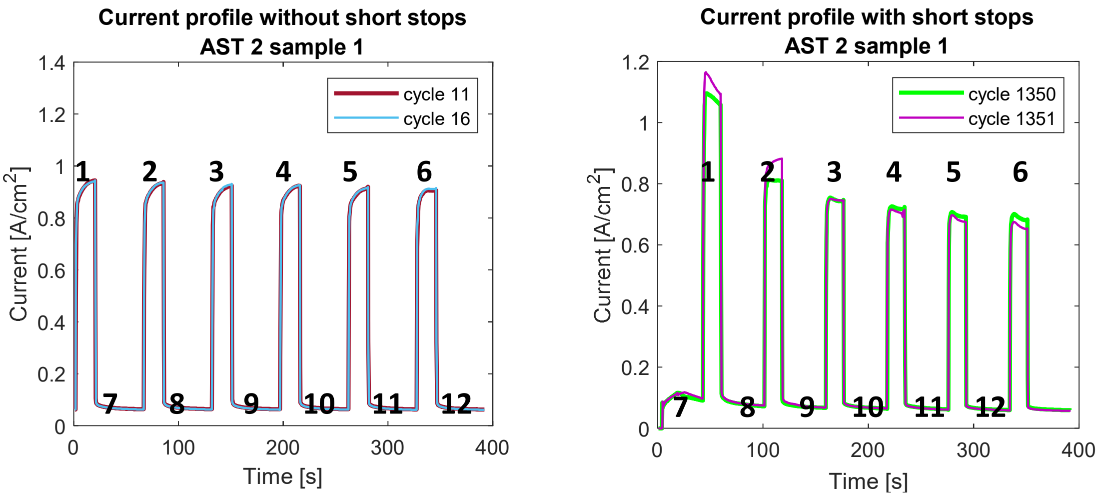

(a) (b)

Figure 38 - Current profiles of AST 2 sample 1: (a) without short stops; (b) with short stops

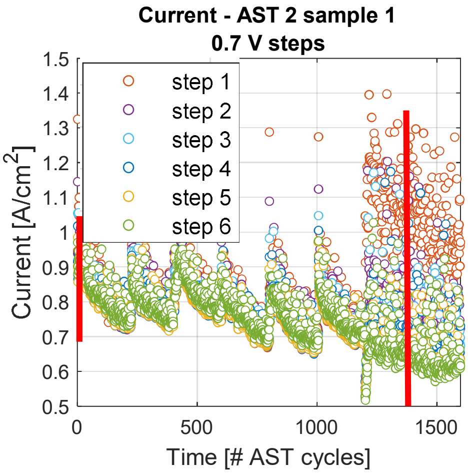

Figure 39 – Current of low voltage steps of AST 2 sample 1 (red lines indicate the position of current profiles shown in Figure 38)

The same current profiles can be observed for sample 2, and the low voltage step current values are reported in Figure 40.

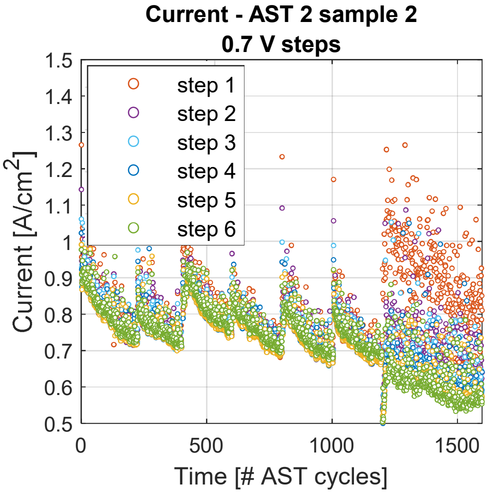

Figure 40 – Current of low voltage steps of AST 2 sample 2

This trend can be explained with a progressive accumulation of a Pt oxide, which reversibly decreases the active area. This oxide is not reduced at 0.7 V, therefore it keeps slowly growing during subsequent AST cycles and is reduced only every 200 cycles thanks to the short stop, while in AST 1 the short stop at the end of every cycle allowed to periodically reduce the formed oxide.

A slow and continue growth of the oxide justify both the single cycle current profile (the oxide grows too slowly to have a visible effect during the single cycle), and the overall trend (during 200 cycles it grows enough to reversibly reduce the current).

In the last 400 cycles, when short stops are introduced, the different steps current trends are not anymore overlapped (Figure 39). Indeed, the single cycle current profile (Figure 38 b) show decreasing values for subsequent low voltage steps: the current has a decreasing trend during the single cycle, but the performance loss is recovered with the short stop, similarly to what was observed in AST 1 (Figure 31). It can be argued that the oxide is totally removed (or at least strongly reduced) at the end of each AST cycle and the current decrease is mainly due to the irreversible performance decay.

AST 3

AST 3 was designed to understand the influence of the low potential limit in MEA degradation. Similarly to previous ASTs, the base cycle is thus composed: a step of 30 s at the UPL is followed by a step of 12 s at the LPL and these two steps are repeated for 6 times. The base cycle was repeated for 2000 times, with a stop every 400 cycles in to perform the characterization tests, while a stop was introduced every 200 cycles.

The test was performed simultaneously on 3 samples. For the first sample the UPL and the LPL were 0.85 V and 0.7 V, for the second one 0.85 V and 0.6 V and for the third one 0.85 V and 0.4 V, as shown in Figure 41.

The operating conditions are shown in Table 12. As the potential reaches low values (0.4 V for sample 3), the air flux at cathode was diluted with nitrogen to 9% of dry oxygen mole fraction. In the meanwhile, the cathode stoichiometry was reduced to 10, a still high value that however allowed to keep constant the total flow rate with respect to previous tests. The dilution avoided too high current values, which could introduce undesired additional degradation effect. The CV plots at different stops are shown in Figure 42, and the resultant ECSA trends in Figure 43.

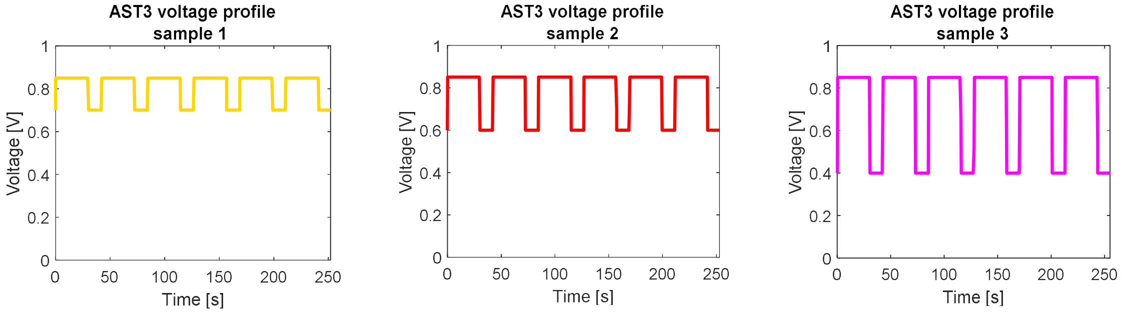

(a) (b) (c)

Figure 41 – AST 3 voltage profile of different samples (a) sample 1; (b) sample 2; (c) sample 3

Parameters	Unit	Values
Cell temperature	°C	71
RH anode	%	100
RH cathode	%	100
Flow rate anode	-	Fixed at $\lambda = 8$
Flow rate cathode	-	Fixed at $\lambda = 10$
Oxygen percentage in dry flow rate	%	9*
Pressure anode	kPa	190
Pressure cathode	kPa	140

*the air flux was diluted with nitrogen

Table 12 - AST 3 operating condition

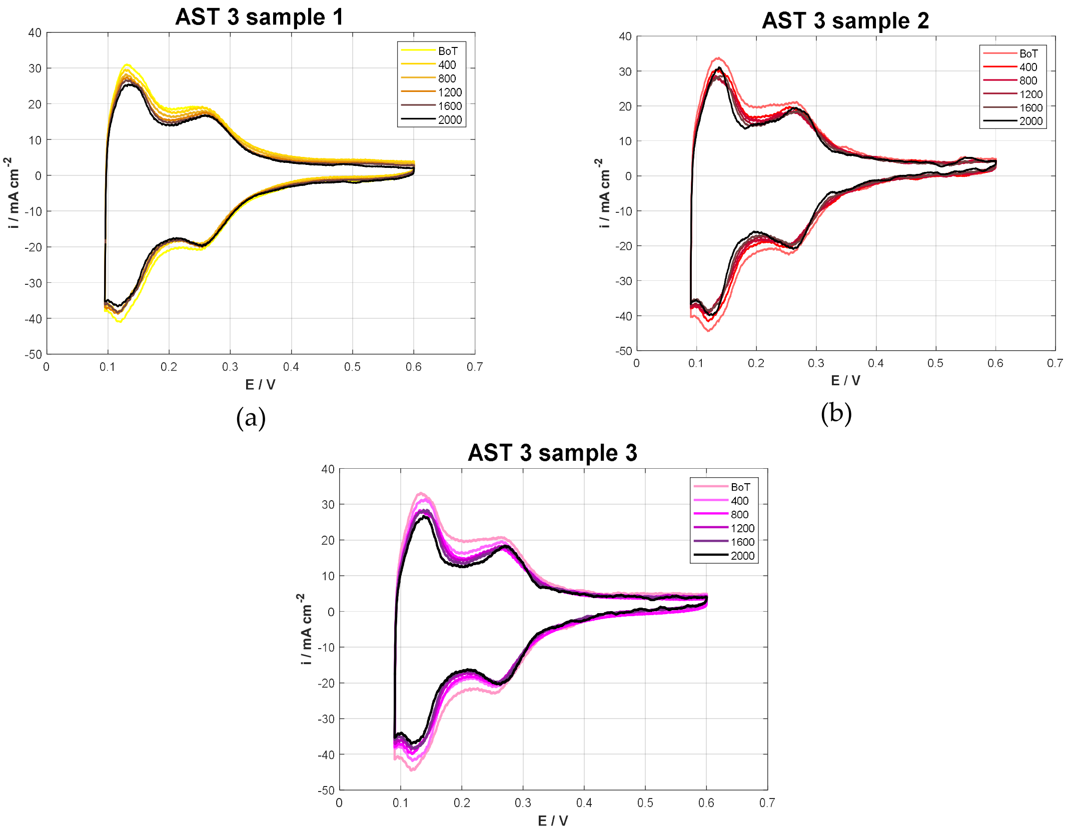

(a)

(b)

(c)

Figure 42 - CV AST 3: (a) sample 1; (b) sample 2; (c) sample 3

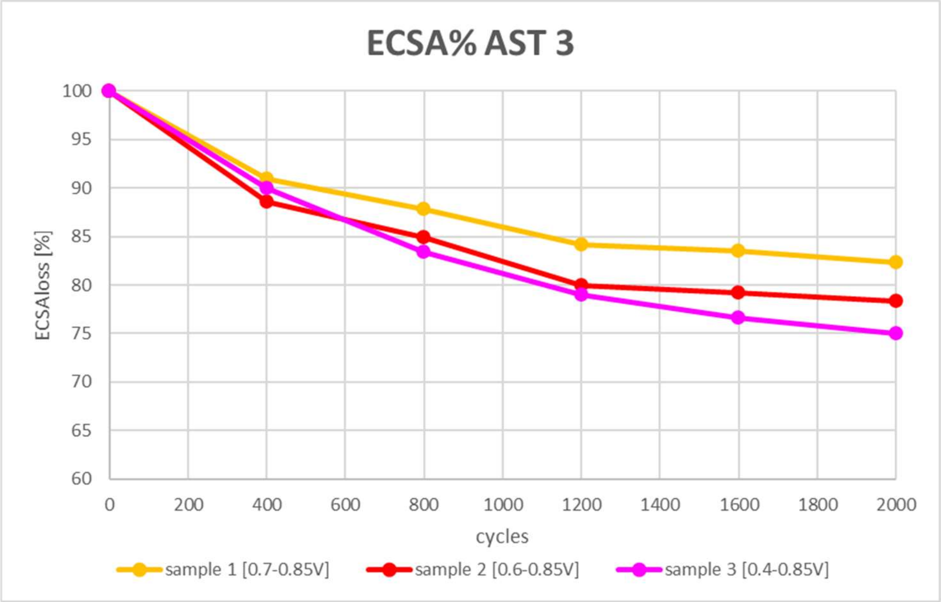

Figure 43 - AST 3 ECSA evolution

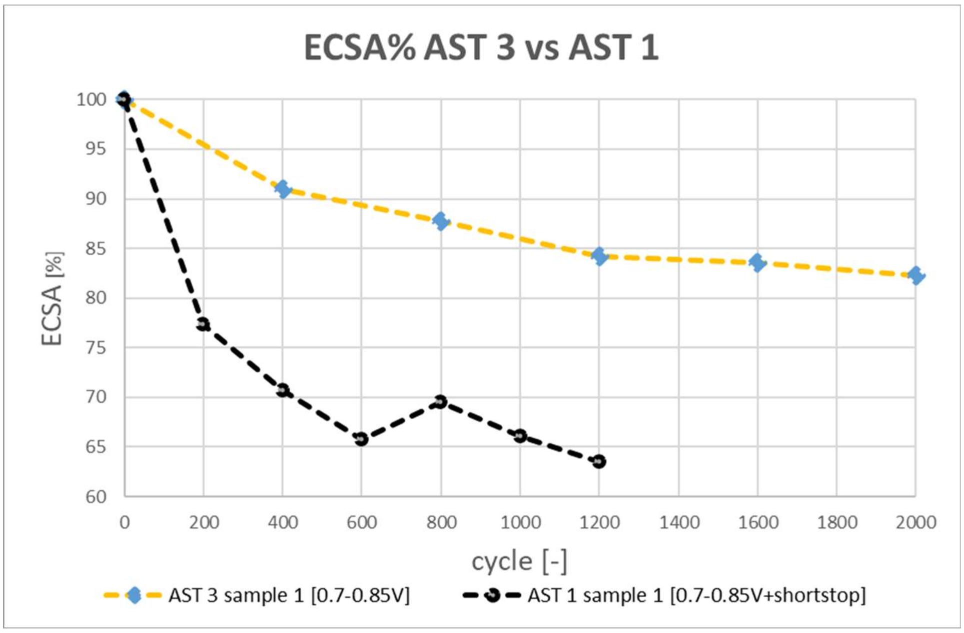

Figure 44 - ECSA evolution AST 3 sample 1 vs AST1

As it was expected [17], cycling profiles with a lower minimum potential value show a higher ECSA loss. Moreover, the comparison between the ECSA trends of AST 3 sample 1 and AST 1 sample 1 (Figure 44), provides a further confirmation of the strong degradation effect which is due to the shortstop: in the former, degradation is much more promoted.

Looking at the current profiles, shown in Figure 45, some interesting features can be highlighted. Sample 1 low voltage steps current (Figure 45a) shows a progressive performance loss, which is almost completely recovered every 200 cycles when the short stop is introduced.

This is the same trend observed in the first 1200 cycles of AST 2, and can be again explained with the progressive accumulation of an oxide which is not reduced at 0.7 V, therefore keeps growing during the test execution and is reduced every 200 cycles thanks to the short stop. A similar trend can be observed also in sample 2 high voltage steps current (Figure 45d). This suggests that the oxide is not totally reduced also when the potential goes down to 0.6 V.

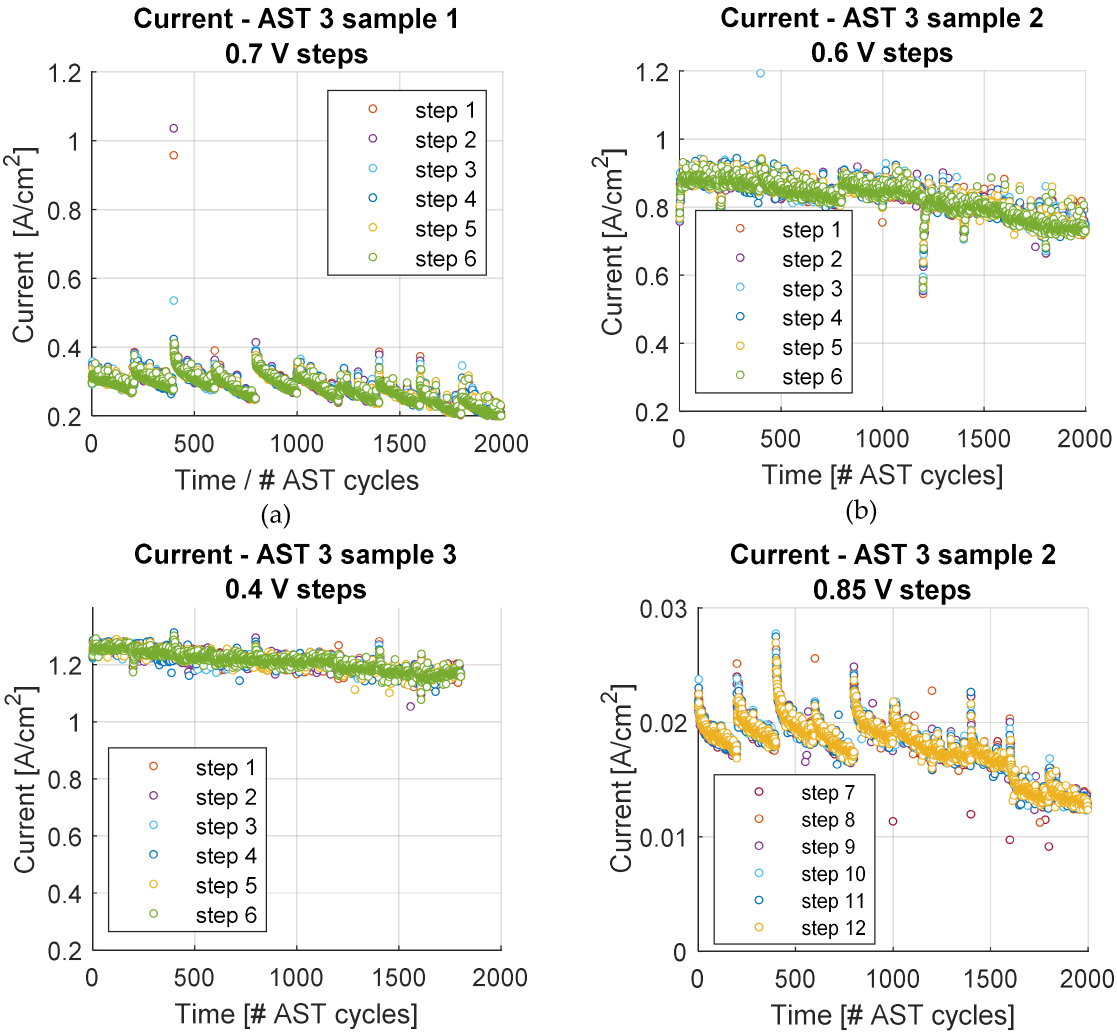

(a) (b) (c) (d)

Figure 45 – Current of AST 3: (a) sample 1 low voltage steps (b) sample 2 low voltage (c) sample 3 low voltage steps (d) sample 2 low voltage steps

*steps number are defined as for previous ASTs (Figure 38a)

AST 4

AST 4 was designed to investigate the effect of a periodic potential reduction on the degradation. To this aim, the base cycle (Figure 46) is composed with a cycling part ranging between 0.85 V and 0.7 V followed by a final holding of 110 s, that would like to mimic short stops at different potential values. The test was performed simultaneously on 4 samples. The UPL and the LPL were 0.85 V and 0.7 V for all the samples while the final Holding Potential (HP) was different: 0.7 V for sample 1, 0.6 V for sample 2, 0.4 V for sample 3, and 0.2 V for sample 4. The base cycle was repeated for 2000 cycles, stopping every 400 cycles to perform the characterization tests.

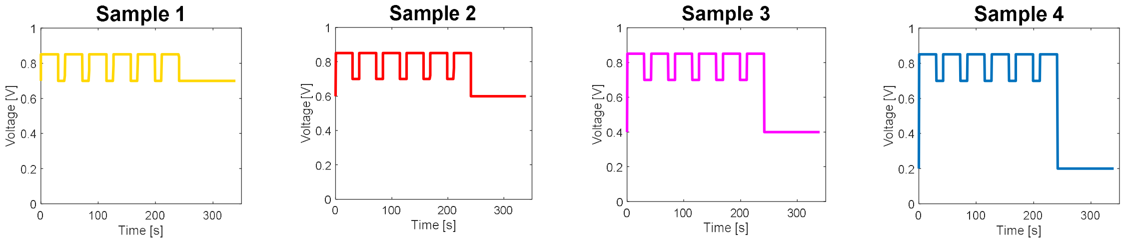

(a) (b) (c) (d)

Figure 46 - AST 4 potential profiles (a) sample 1; (b) sample 2; (c) sample 3; (4) sample 4.

The operating conditions are shown in Table 13. The air flux was diluted with nitrogen to avoid too high current values for sample 3 and 4 during the final holding, which would cause a degradation of the cell.

CV plots are shown in Figure 47, and the obtained ECSA trends in Figure 48. As expected from the previous analysis, samples with final holding at lower potential values show a higher ECSA loss. It is also worth underlining that sample 4 shows a lower ECSA loss with respect to AST 1 results (Figure 49). Thus, the final holding at 0.2 V does impact on ECSA loss as much as the short stop without air supply, that draws the MEA to even lower voltages.

The ECSA trends of sample 1, 2 and 3 shows quite similar results with sample 1, 2 and 3 of AST 3 respectively (the comparison is shown in Figure 49). It is thus not clear whether a continuous cycling on a wider potential range (AST 3) or a cycling on a narrower potential range, with less frequent potential reduction (AST 4) has a stronger effect on degradation. However, from these results it can be concluded that the introduction of a low potential step after quite a long time spent at high voltages impact significantly on degradation and could drive a different mechanism of ECSA loss.

Parameters	**Unit**	**Values**
Cell temperature	°C	71
RH anode	%	100
RH cathode	%	100
Flow rate anode	-	Fixed at $\lambda = 8$
Flow rate cathode	-	Fixed at $\lambda = 10$
Oxygen percentage on dry flow rate	%	9*
Pressure anode	kPa	190
Pressure cathode	kPa	140

*the air flux was diluted with nitrogen

Table 13 - AST 4 operating conditions

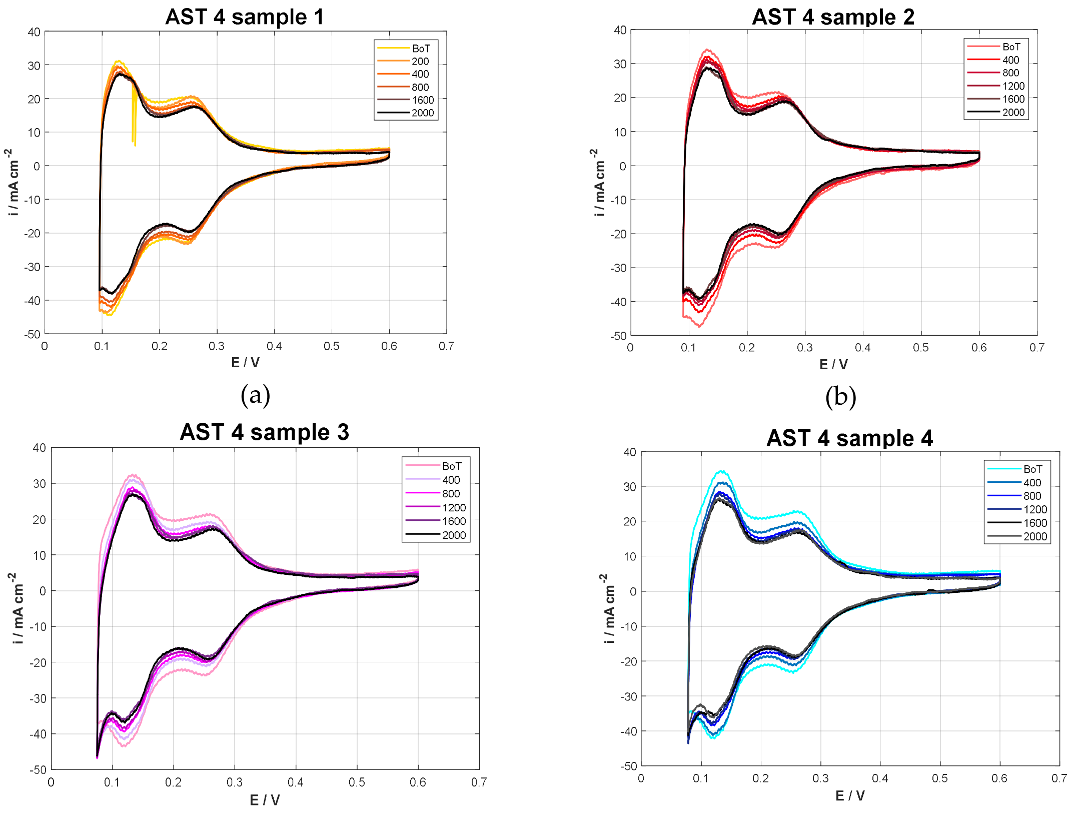

(a)

(b)

(c)

(d)

Figure 47 - CV AST 4: (a) sample 1; (b) sample 2; (c) sample 3; (d) sample 4.

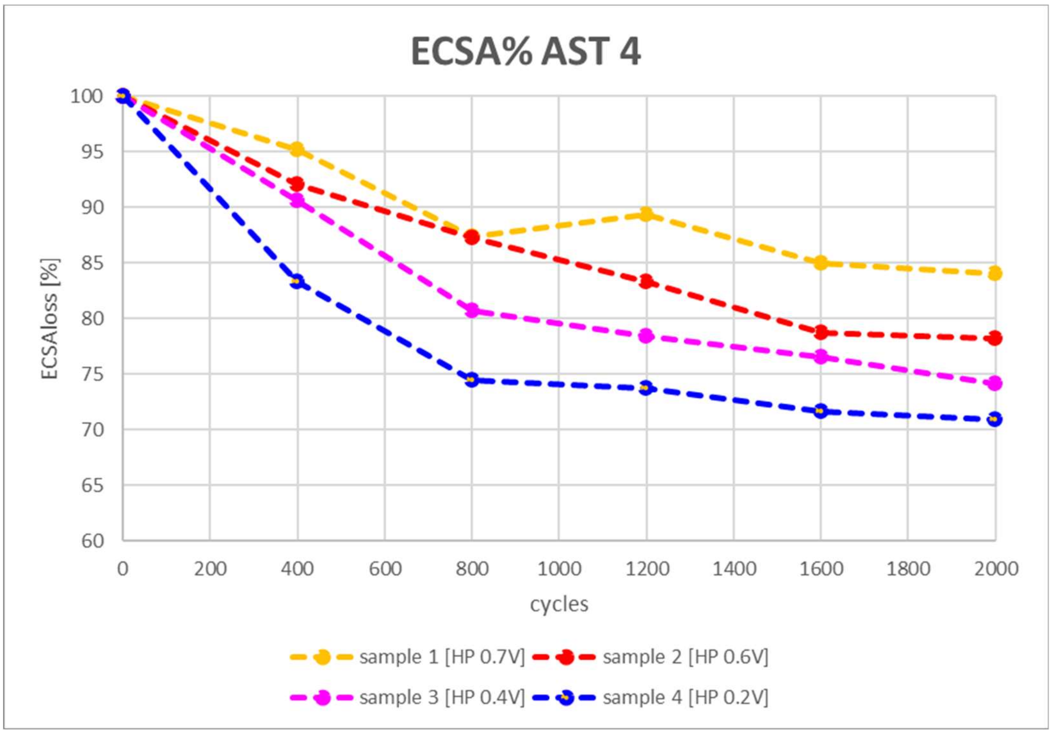

Figure 48 - ECSA evolution AST 4

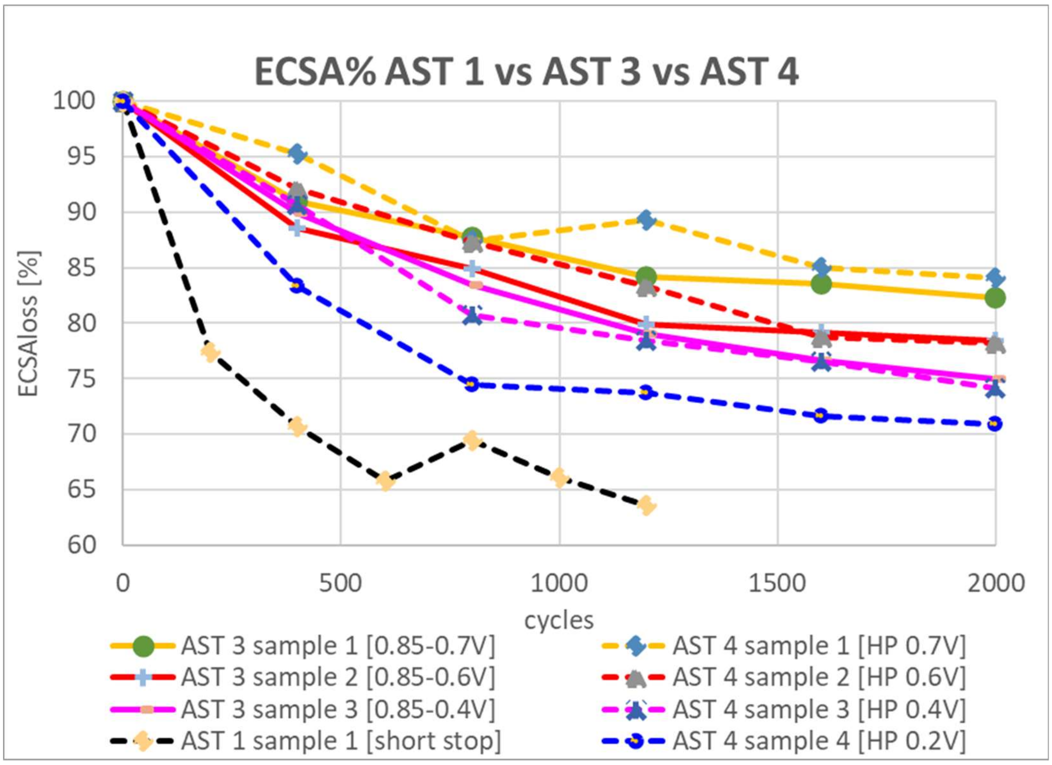

Figure 49 - ECSA evolution AST 4 vs AST 3 vs AST 1

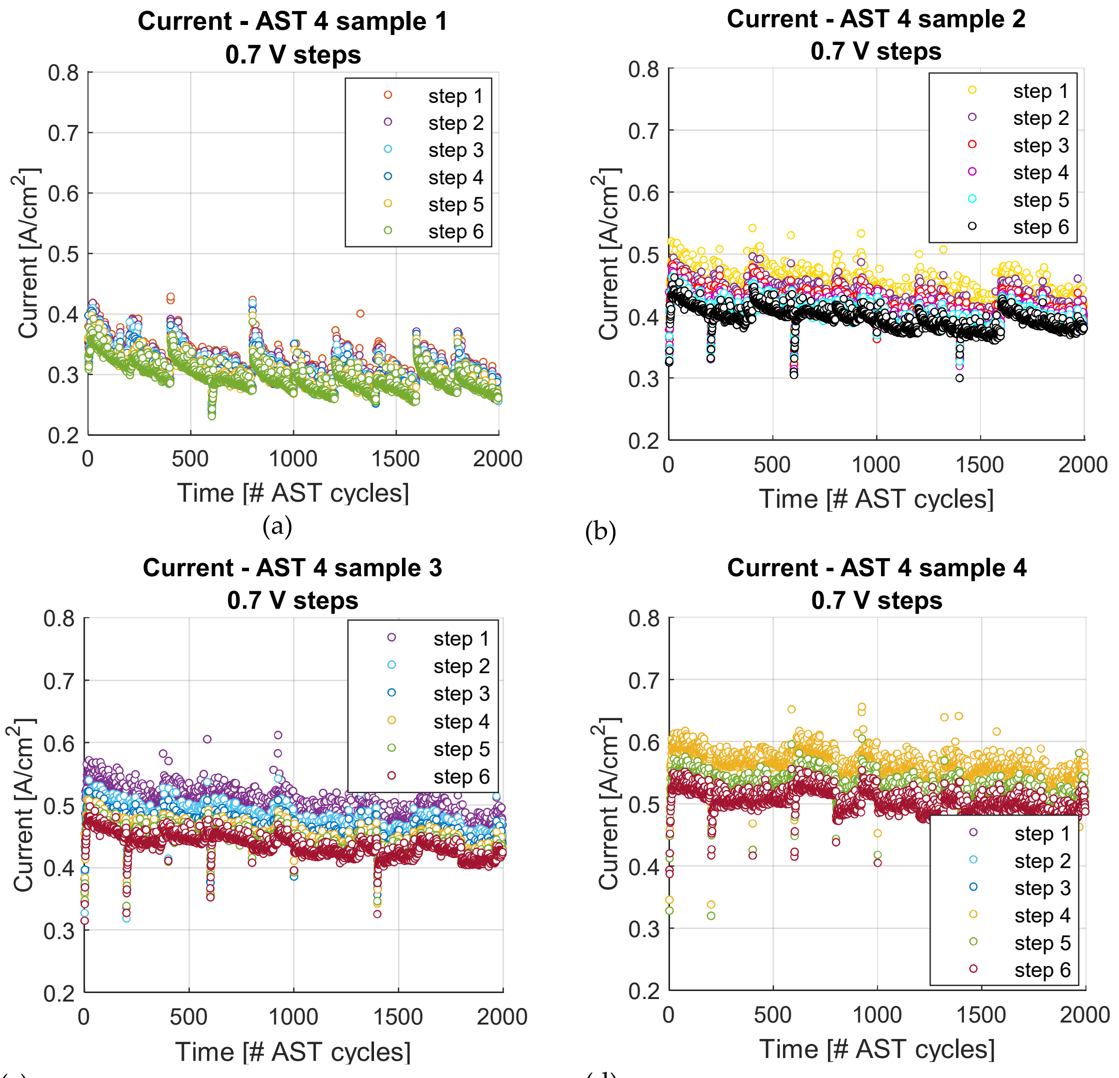

(a) (b) (c) (d)

Figure 50 - Current of AST 4 during low voltage steps: (a) sample 1 (b) sample 2 (c) sample 3 (d) sample 4

Sample	**Mean current value of low voltage steps [A]**
1	0.3075
2	0.4207
3	0.4682
4	0.5122

Table 14 - AST 4 mean current values of low voltage [0.7 V] steps

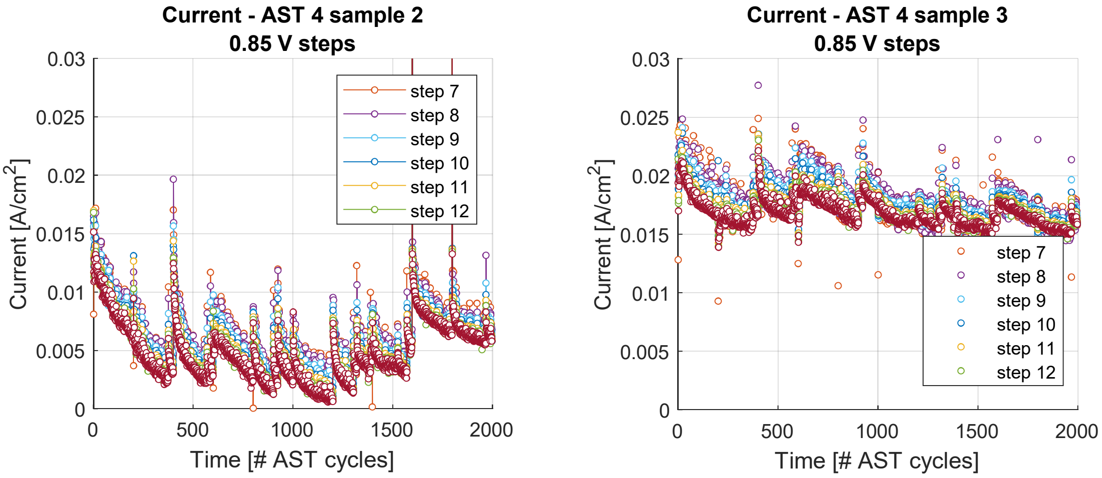

(a) (b)

Figure 51 – Current of AST 4 during high voltage steps: (a) sample 2 (b)sample 3 *steps number are defined as for previous ASTs (Figure 38a)

Low voltage steps currents (Figure 50) show increasing values from sample 1 to sample 4 (mean values are reported in Table 14), although the potential is the same (0.7 V). This can be again explained with the formation of an oxide which grows during the cycling and is differently reduced in the four samples: lower holding potential values enhance the oxide reduction, cleaning the catalyst surface and thus allowing a higher current production.

The current plots also seem to confirm this interpretation: the low voltage steps of sample 1 and 2 (Figure 50a and Figure 50b) shows a reversible performance decrease which is recovered with the shortstop (similarly to the one observed in AST 2 and 3). A similar trend can be recognized also looking at the high voltage steps current of sample 2 and 3 (Figure 51), suggesting that the oxide is not completely reduced even going down to 0.4 V. This result is really interesting, as this potential value is below the one typically considered in the literature for the reduction of PtO, which is around 0.6 V. Hence, the presence of a different, more resistant oxide can be hypothesized.

4.3. Preliminary simulations results

The accelerated stress tests 1, 3 and 4 were simulated with the model described in 3.1, using the parameters obtained from the calibration with experimental data, reported in Table 15. This set of parameters will be referred to as SET 0.

Parameter	**Symbol**	**Value**	**Unit**
Oxidation parameters			
Reference oxidation equilibrium potential	Φ_{ox}^{ref}	0,99	V
Oxidation kinetic constant	k_{ox}	8E-10	$mol\ cm^{-2}$
Transfer coefficient	α_{a2}	0,35	-
Transfer coefficient	α_{c2}	0,5	-
Platinum Oxide interaction energy	ω_{PtO}	26000	$J\ mol^{-1}$
Anodic dissolution parameters			
Anodic dissolution kinetic constant	k_{dis}^{ref}	$1 * 10^{-9}$	$mol\ cm^{-2}s^{-1}$
Transfer coefficient	α_{a1}	0.5	-
Transfer coefficient	α_{c1}	0.5	-

Table 15 - calibrated parameters: SET 0

The particle radius distribution of the catalyst layer was determined with a TEM-based analysis (Transmission Electron Microscopy) of a fresh sample, made by MINATEC laboratory in CEA-Grenoble institute. The real PRD was represented with a log normal distribution discretized in 16 particle groups, as shown in Figure 52. During the simulation, the groups were eliminated if their radius decreased under a minimum value, set to 0.7 nm, and a corresponding amount of Pt mass is added to dissolved platinum (increasing the concentration) to respect mass conservation. This limit was imposed to prevent the particles from getting infinitely small, causing numeric calculation errors.

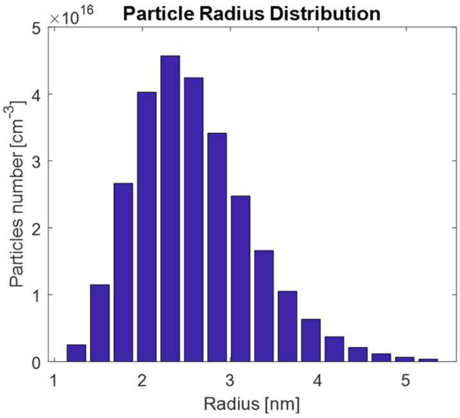

Figure 52 - Particle Radius Distribution

Potential profiles were corrected to take into account the ohmic loss consequent to current density that was measured during the AST. The ohmic loss is proportional to the high frequency resistance value and to the current, as described below, and therefore is relevant only for high current values. Hence, only the values of lower potential steps require a correction, according to equation (24), where LPL is the imposed lower potential limit, LPL_{eff} is the effective lower potential limit in the cathode catalyst layer, $I_{av,LPL}$ is the mean current value measured for the low potential step and HFR is the High Frequency Resistance. For AST 4 simulations, also holding potential values were corrected (equation (25)).

$$LPL_{eff} = LPL + HFR * I_{av,LPL} \tag{24}$$

$$HP_{eff} = HP + HFR * I_{av,HP} \tag{25}$$

The HFR was measured with an Electrochemical Impedance Spectroscopy (described in 2.4.2) performed with the same operating conditions of the ASTs, imposing three different current values (Figure 53). The measured HFR was 0.025 Ω/cm².

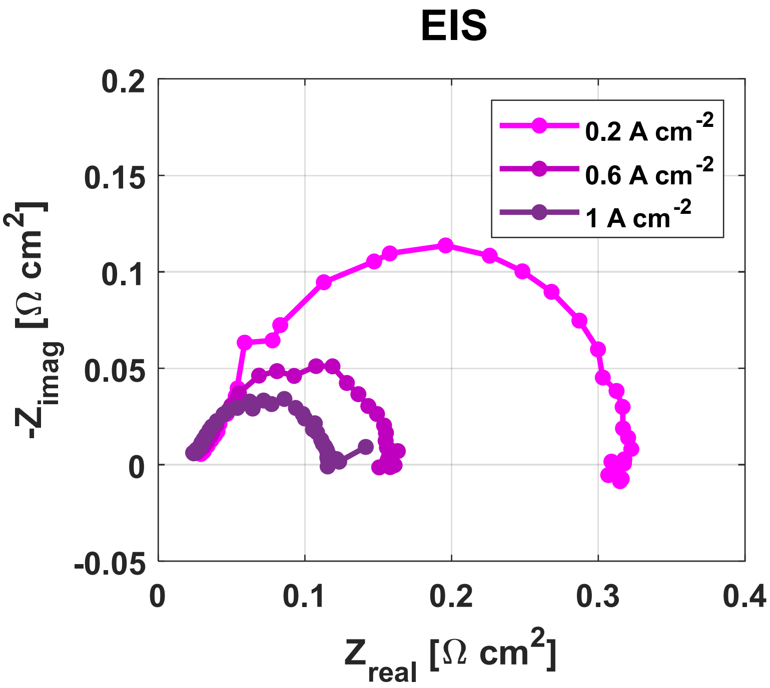

Figure 53 - Electrochemical Impedance Spectroscopy

ASTs simulations with parameters SET 0

Figure 54 depicts the ECSA evolution obtained simulating AST 1, compared with experimental results, while Figure 55 shows the simulated oxide coverage and anodic dissolution rates profiles for different particle groups during the first AST cycle.

The simulated ECSA trends do not match with experimental results, resulting in a lower degradation. With this parametrization indeed, the oxide (Figure 55a and c) is continuously reduced during the cycling when the potential goes down to 0.7 V, differently from what was observed in the experimental current data. The anodic dissolution therefore has the same profile during the cycling and the short stop (Figure 55b and d). The higher degrading effect of the short stop is not reproduced at all.

Sample 2 base profile, characterized by a higher UPL with respect to sample 1, show a higher oxide coverage (Figure 55c) and a higher anodic dissolution rate (Figure 55d). Therefore, according to the model, a higher UPL results in a stronger ECSA loss (Figure 54). This is in agreement with the literature [16][17][18], but not with the experimental results, which instead show a really limited impact of the UPL on degradation when the short stop is present.

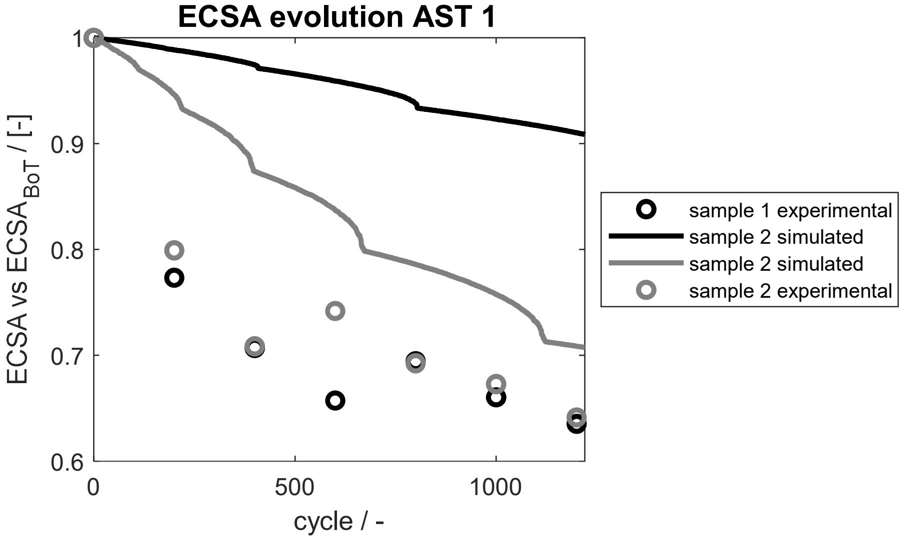

Figure 54 - ECSA evolution AST 1: experimental vs simulated data with parameters SET 0

[AST 1 sample 1: 0.7-0.85V + shortstop; AST 1 sample 2: 0.7-0.9V + shortstop]

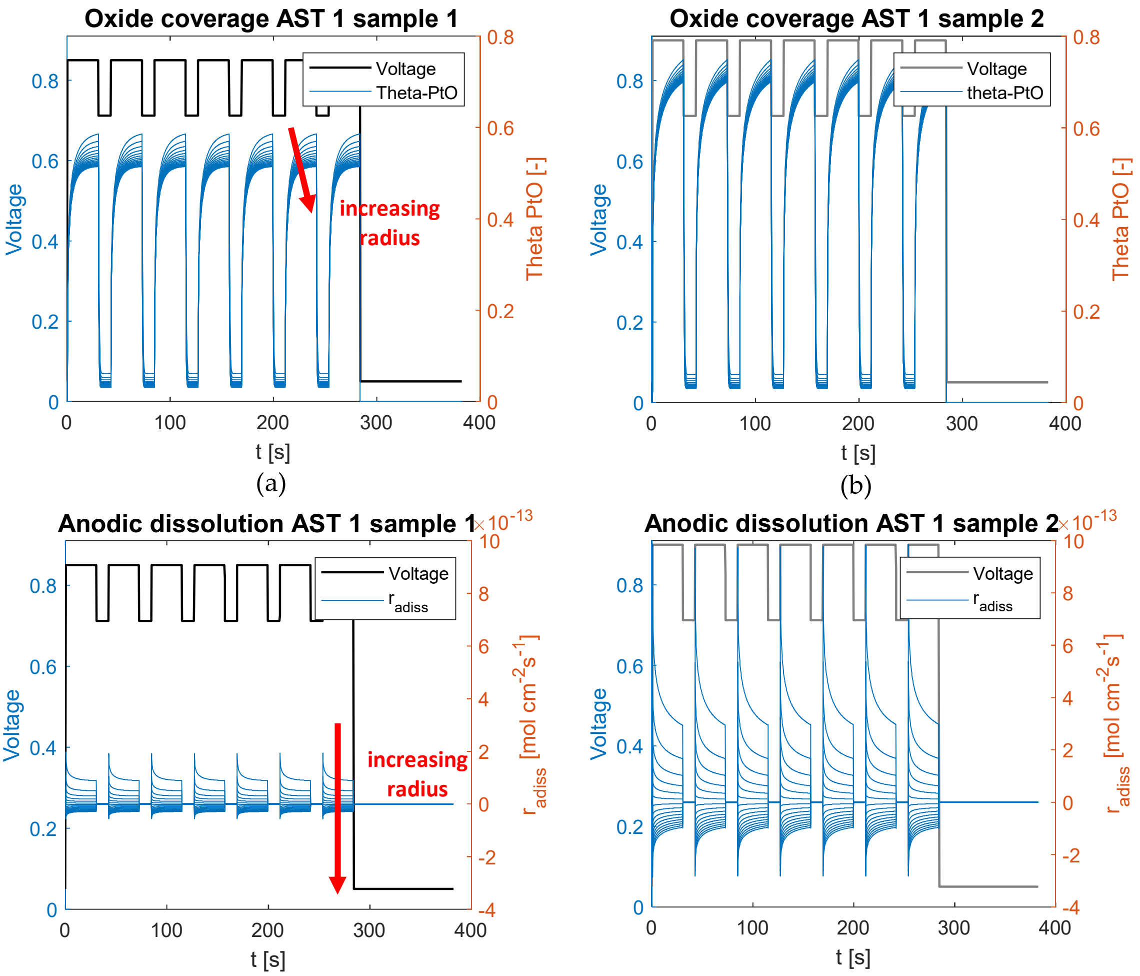

(a) (b) (c) (d)

Figure 55- AST 1 base profile for different particle groups with parameters SET0: (a) sample 1 PtO oxide coverage; (b) sample 2 PtO oxide coverage; (c) sample 1 anodic dissolution reaction rate; (d) sample 2 anodic dissolution reaction rate;

AST 3 simulation also results in a lower ECSA loss with respect to experimental one for all the samples (Figure 56). Moreover, the trends of different samples are exactly overlapped. The oxide profiles (Figure 57a,b,c) are indeed very similar, as the oxide is almost totally reduced at 0.7 V. This results in equal anodic dissolution reaction rates (Figure 57d,e,f), and consequently equal ECSA trends.

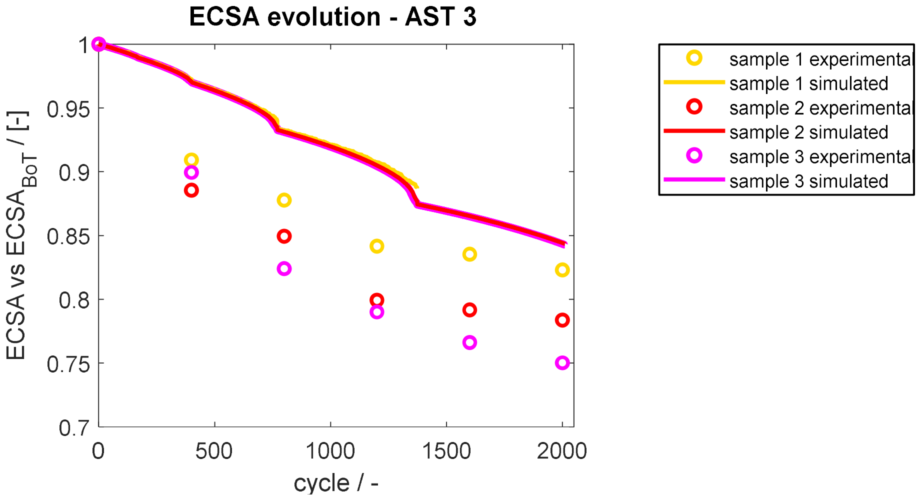

Figure 56 – ECSA evolution AST 3: experimental vs simulated data with parameters SET 0

[AST 3 sample 1: 0.7-0.85V; sample 2: 0.6-0.85V; sample 3: 0.4-0.85V; NO SHORT STOP]

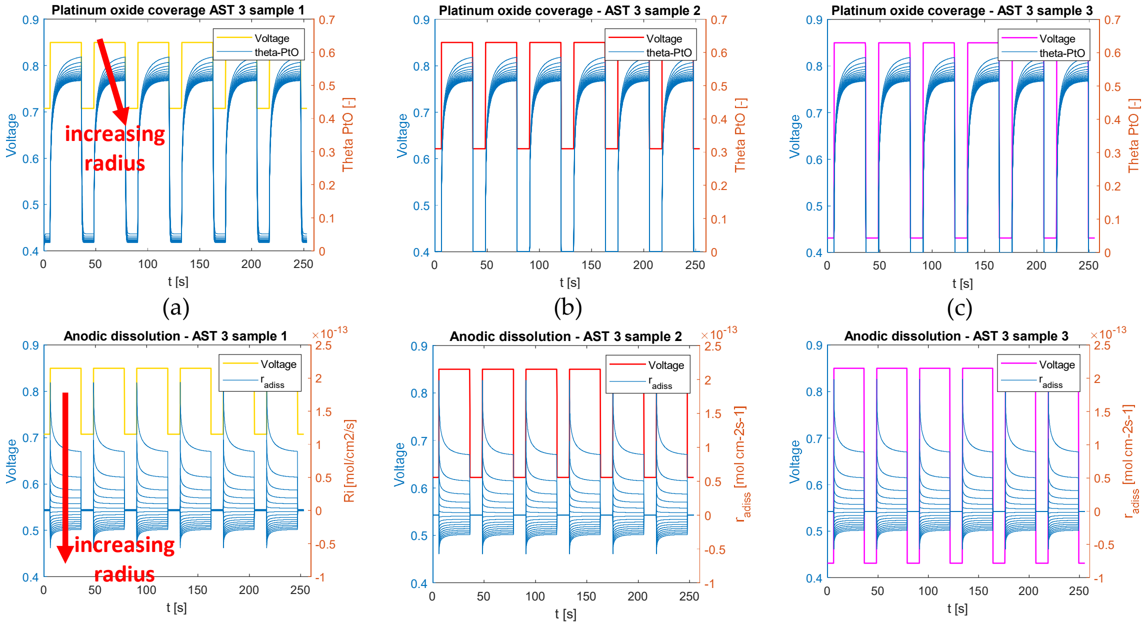

(a) (b) (c)

(d) (e) (f)

Figure 57 - AST 3 base profile for different particle groups with parameters SET0: (a) sample 1 PtO oxide coverage; (b) sample 2 PtO oxide coverage; (c) sample 3 PtO oxide coverage; (d) sample 1 anodic dissolution reaction rate; (e) sample 2 anodic dissolution reaction rate; (e) sample 3 anodic dissolution reaction rate

AST 4 simulation provides similar results. The degradation is indeed lower than the experimentally measured one and the different samples trends are overlapped (Figure 59). The oxide profiles (Figure 58) are indeed identical, resulting in equal anodic dissolution reaction rates and equal ECSA trends.

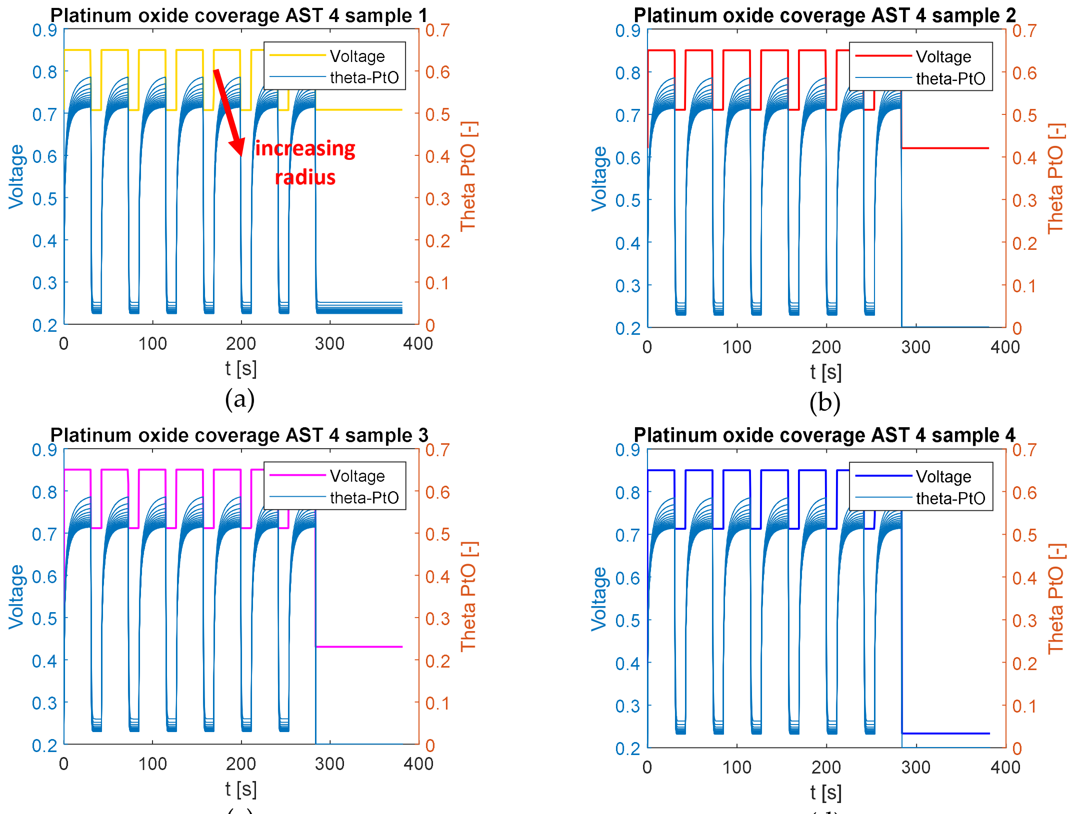

(a) (b) (c) (d)

Figure 58 - AST 4 base profile PtO oxide coverage for different particle groups with parameters SET0: (a) sample 1; (b) sample 2; (c) sample 3; (d) sample 4

These simulations lead to the conclusion that the model, at least with parameters SET 0, is not able to reproduce the experimental data. The oxide is indeed almost completely reduced at 0.7 V, which does not agree with the experimental data and leads to equal ECSA loss also for profiles with different low potential values.

Consequently, the parameters were varied trying to reproduce with the PtO the expected oxide profiles, increase the degradation and stress the difference between the different samples of the same AST without modifying the model structure.

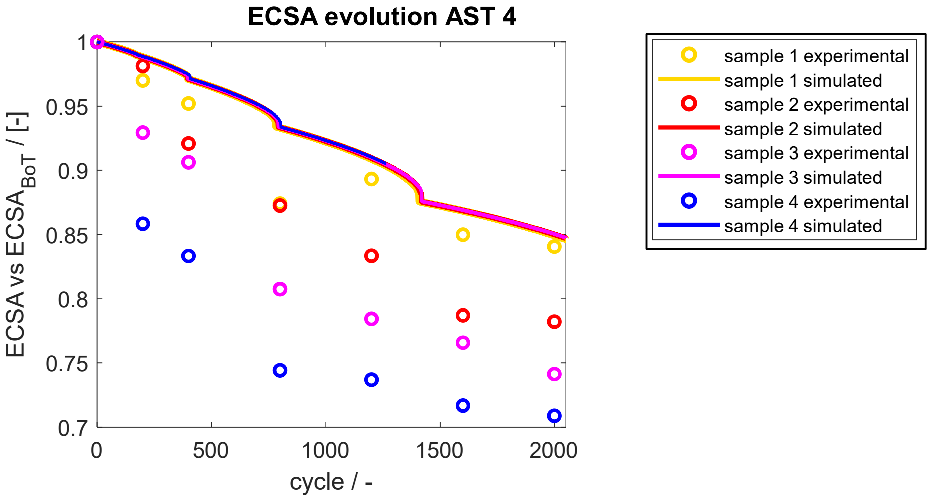

Figure 59 - ECSA evolution AST 4: experimental vs simulated data with parameters SET 0

[AST 4 sample 1: 0.85-0.7V+ holding at 0.7V; sample 2: 0.85-0.7V+ holding at 0.6 V; sample 3: 0.85-0.7V+ holding at 0.4V; sample 4: 0.85-0.7V+ holding at 0.2 V]

ASTs simulations with parameters SET 1.0 and 1.1

Firstly, the oxide parameters were modified, decreasing the equilibrium potential Φ_{ox}^{ref} (to shift the oxide reduction towards lower potentials) and consequently the kinetic constant k_{ox} to obtain similar oxidation reactions rates, that would otherwise increase lowering the equilibrium potential value. AST 3 was simulated with these parameters, which will be referred to as SET 1.0 (Table 16).

Symbol	Value SET 0	Value SET 1.0	Value SET 1.1	Unit
Φ_{ox}^{ref}	0,99	**0,9**	0,9	V
k_{ox}	8E-10	**9E-11**	9E-11	$mol\ cm^{-2}$
α_{a2}	0,35	0,35	0,35	-
α_{c2}	0,5	0,5	0,5	-
ω_{PtO}	26000	26000	26000	$J\ mol^{-1}$
k_{dis}^{ref}	1E-9	1E-9	**2E-9**	$mol\ cm^{-2}s^{-1}$
α_{a1}	0.5	0.5	0.5	-
α_{c1}	0.5	0.5	0.5	-

Table 16 - Parameters SETs

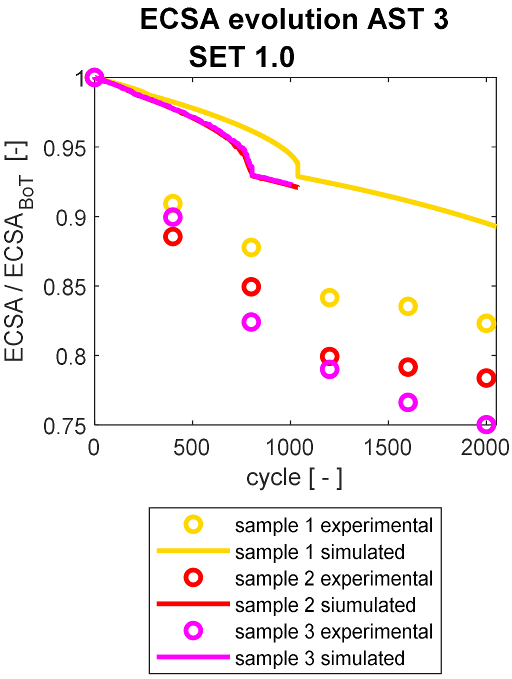

Figure 60 - ECSA evolution: AST 3 experimental vs simulated data with parameters SET 1.0

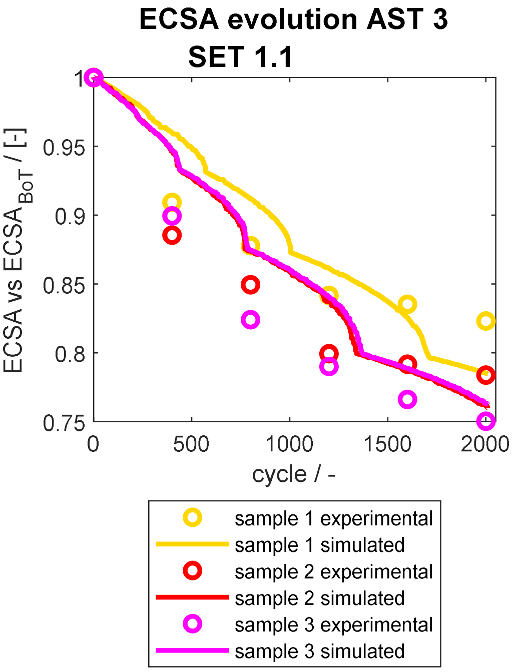

Figure 61 - ECSA evolution: AST 3 experimental vs simulated data with parameters SET 1.1

[AST 3 sample 1: 0.7-0.85V; sample 2: 0.6-0.85V; sample 3: 0.4-0.85V; NO SHORT STOP]

The obtained ECSA trends (Figure 60) are not anymore overlapped. The oxide profiles of sample 1 and 2 (Figure 62) are indeed different: at 0.7 V the oxide is only partially reduced, while going down to 0.6 V it is almost totally reduced. Consequently, anodic dissolution rate of samples 1 and 2 has different profiles and different effects on degradation. Sample 2 and 3 instead, still have similar base profile and consequently equal ECSA trends. The oxide profiles are thus more in agreement with the interpretation of experimental data previously described, but the degradation is still underestimated.

The anodic dissolution kinetic constant k_{di}^{ref} was thus slightly increased, the resulting parameters will be referred to as SET 1.1 (Table 16). AST 3 was then simulated with these parameters. The resulting ECSA trends (Figure 61) are closer to experimental data but there’s no difference between sample 2 and 3. The oxide profiles of these samples (which are equal to those shown in Figure 62 for parameter SET 1.0, as the oxide parameters are unchanged) are indeed slightly different, but the resulting anodic dissolution (Figure 63) are really similar, resulting in the same degradation.

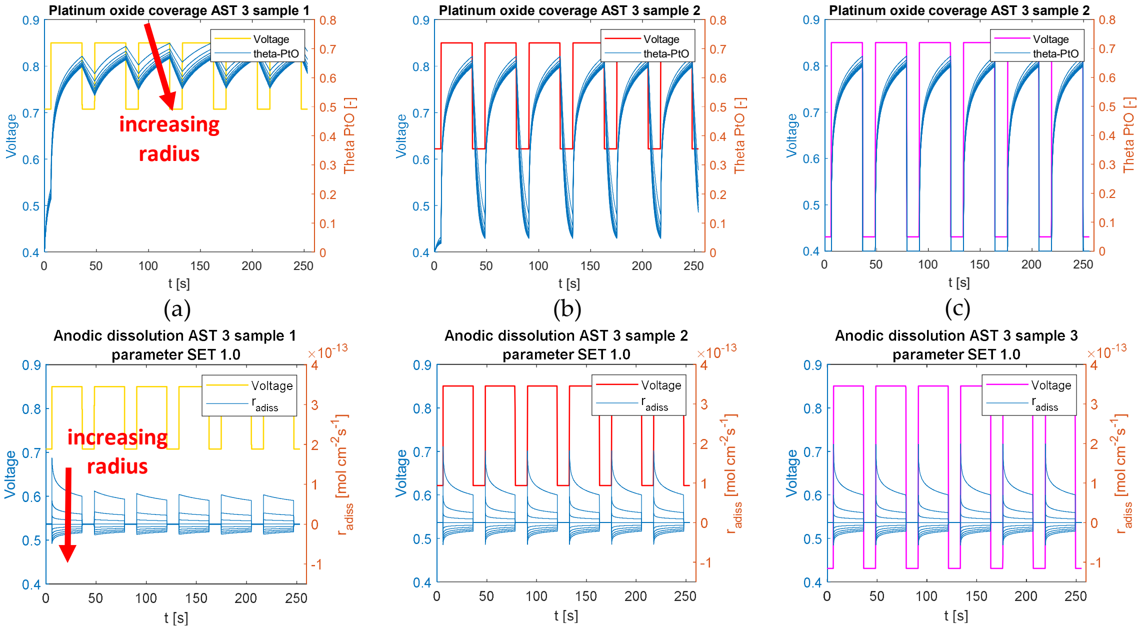

(a) (b) (c)

(d) (e) (f)

Figure 62 - AST 4 base profile for different particle groups with parameter SET 1.0: (a) sample 1 PtO oxide coverage (b) sample 2 PtO oxide coverage (c) sample 3 PtO oxide coverage (d) sample 1 anodic dissolution reaction rate (e) sample 2 anodic dissolution reaction rate (f) sample 1 anodic dissolution reaction rate

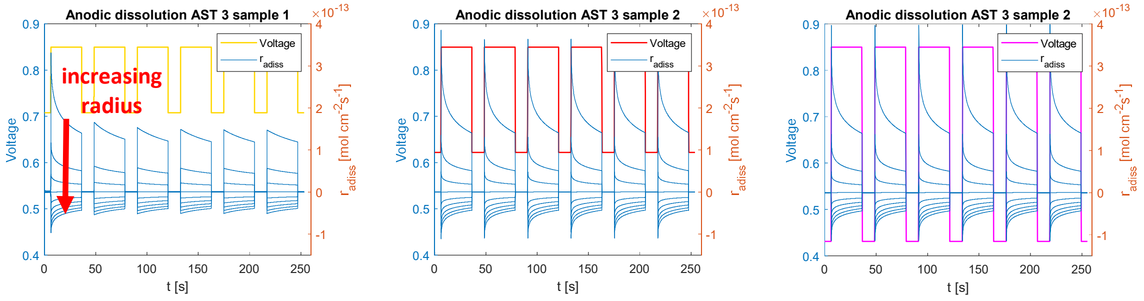

(a) (b) (c)

Figure 63 - AST 4 base profile with parameters SET 1.1: anodic dissolution reaction rates for different particle groups (a) sample 1 anodic dissolution reaction rate (b) sample 2 anodic dissolution reaction rate (c) sample 3 anodic dissolution reaction rate

Even changing the parameters, AST simulations still does not provide totally satisfying results. Moreover, with these parameters the model is not able anymore to reproduce the experimental data used to calibrate the model (as explained in 3.4).

The holding-LSV coverage values obtained with the different parameters SET are compared in Figure 64. With parameters SET 1.1 (Figure 64b), the coverage is overestimated, especially at low potential values.

Cyclic voltammetry simulated with the new parameters (Figure 65) also provide a worse approximation of the experimental one, as the oxide reduction peak is shifted toward lower potential values, around 0.55V, while in the literature [7][3], [7][3], as evinced by the recorded data of the present work, the PtO oxide is usually considered to be completely reduced for higher values (≥0.6V).

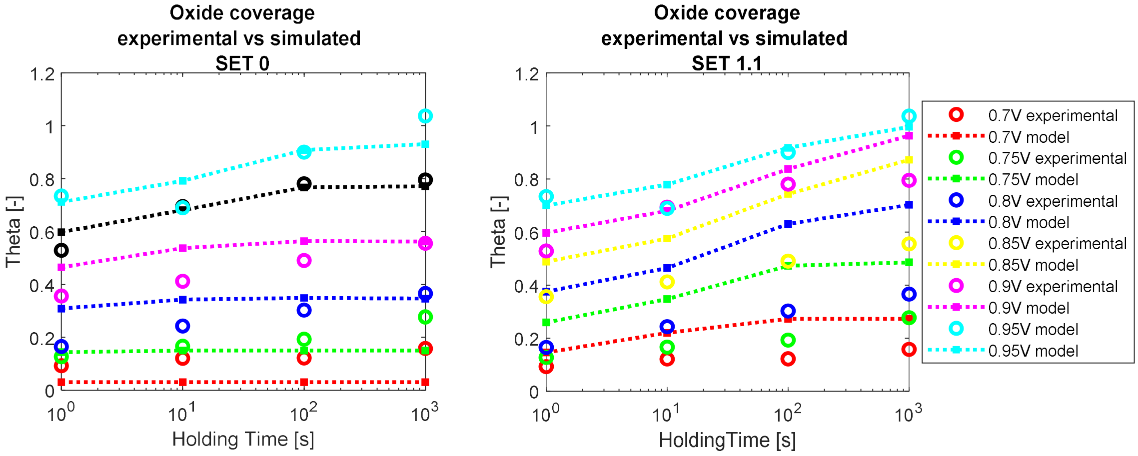

(a) (b)

Figure 64 - Oxide coverage: experimental VS simulated data:
(a) parameters SET 0; (b) parameters SET 1.1

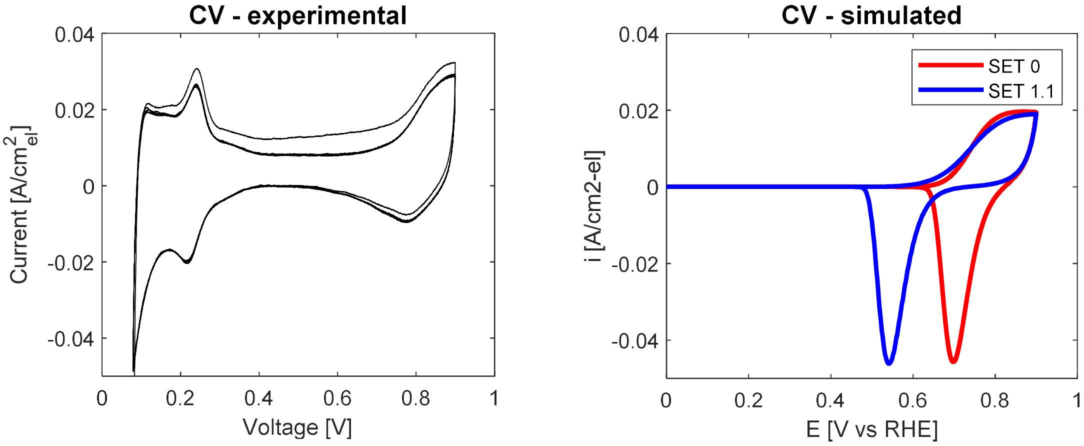

(a) (b)

Figure 65 – Cyclic voltammetry (a) experimental; (b) simulated

The model is thus not able to reproduce the experimental data, not even changing the parameters set. This suggests the need for a further development of the model, including a more complex oxidation and dissolution mechanism, which will be discussed in Chapter 5.

4.4. Conclusion

Several Accelerated Stress Tests (ASTs) were performed in hydrogen/air with different voltage profiles, under conditions that mimic realistic automotive low power operation. Figure 66 qualitatively summarize the results of the different ASTs in terms of ECSA loss.

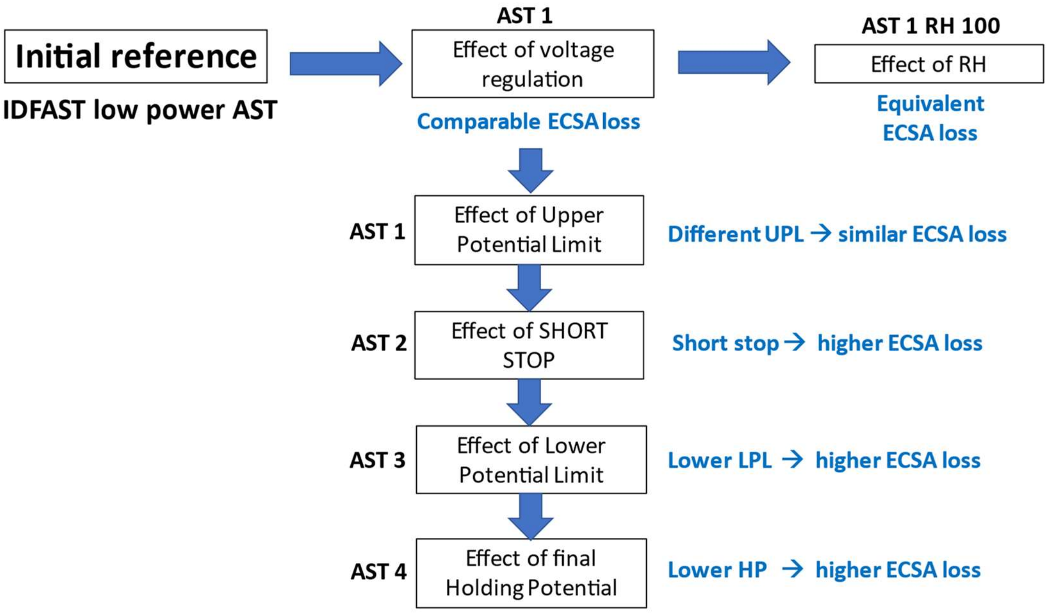

Figure 66 - ECSA loss experimental results: an overview

The degradation tests were designed starting from the IDFAST Low Power AST, based on a square wave current profile ranging between the current values which correspond to 0.85 V and 0.7 V at BOT, and including a short stop at the end of each AST cycle.

Firstly, voltage was imposed instead of current (ranging between 0.7 and 0.85 V), resulting in a comparable degrading effect. The potentiostatic mode was then preferred over the galvanostatic one as it is easier to be simulated with the model. Relative humidity was also increased with respect to the IDFAST low power AST, to check its effect on degradation, and really similar ECSA trends were obtained.

Secondly, the effect of a higher maximum potential (increased to 0.9 V) was investigated, resulting in a similar degrading effect, differently from what is typically reported in the literature [16][17][18]. The effect of the short stop was also studied: it emerged that a square wave potential profile ranging between 0.7 V and 0.85 V has a low impact on degradation, while a much stronger degradation is observed when short stops are introduced.

Finally, the effect of the minimum potential was investigated. It emerged that lower minimum potentials lead to stronger degradation, both when the potential is continuously reduced under 0.7 V and when it is only periodically reduced under this value at the end of each AST cycle.

Moreover, the current trends detected during the ageing tests suggested the presence of an oxide which needs very low voltage to be reduced (< 0.4 V).

The model in its first version is not able to reproduce the experimental results: simulated ECSA trends of different ASTs are similar, the ECSA loss is too low, and the degrading effect of short stop is not reproduced. Indeed, the PtO oxide is totally reduced at 0.7 V, resulting in similar oxide profiles for all the simulated voltage profiles, and consequently similar anodic dissolution rate and ECSA trends.

The degradation only increases when simulating the AST with higher UPL, which agrees with lot of the literature results but not with experimental data.

Therefore, parameters were varied trying to reproduce the expected oxide profiles, increase the degradation and stress the difference between the different potential profiles. To this aim, the oxidation equilibrium potential was reduced and also other parameters were changed, obtaining ECSA trends closer to experimental results. Nonetheless, with these parameters the model shows major deviations trying to reproduce the experimental data used to calibrate the model. In particular, the oxide reduction is shifted toward a lower potential value, which is different from the one experimentally observed and provided by the literature for the PtO oxide.

5 Model: a further development

In this chapter, a further developed version of the model will be described. As seen in section 0, the model in its first version is not able to reproduce the experimental data. A more complex model has been thus implemented, with different oxidation and dissolution mechanisms.

The accelerated stress tests were then simulated with the developed model, and a sensitivity analysis was performed to understand the effect of new reactions parameters and obtain a better reproduction of experimental results.

5.1. Need for a further model development: place exchange and cathodic dissolution

Place exchange and cathodic dissolution (explained in 1.2.1) were introduced in the model, as they can explain some of the experimental results.

The decreasing current trends observed in the AST cycles without short stops (Figure 39, Figure 45a, Figure 50a, Figure 51) can be attributed not just to one oxide but to the combination of two oxides: a simple one (PtO), which is reduced at higher potential values, and a more resistant one (the place-exchanged oxide), which is accumulated during the cycling and reduced only going to lower potential values.

The presence of a more resistant oxide could also justify the AST 4 current trends, which show, at the same potential, increasing current values for samples that reach lower potential values during the final holding (Table 14). This can be explained with the formation of a resistant oxide which is not completely reduced even for values as low as 0.4 V (hardly explained only by means of the PtO oxide).

This perspective also justifies the strong degrading effect of short stops, as well as the increasing degradation observed in AST 3 and AST 4 for samples reaching lower potential values. The resistant oxide is accumulated when the cell voltage is kept above 0.7 V and dissolved when going to lower potential values. For lower potential values a stronger dissolution takes place, cleaning the catalyst active area from oxides (this explains the different current values of AST 4 samples at the same potential) but also causing a stronger degradation.

Although in deaerated solutions the place exchange is usually considered relevant at potentials higher than 1.15 V, different values, as low as 0.75 V [10], have been reported and attributed to the presence of oxygen.

5.2. Model description

With respect to the model structure described in section 3.1, two more reactions are considered: place exchange (reaction (26)) and cathodic dissolution (reaction (28)).

$$\mathrm{PtO} \rightleftarrows \mathrm{OPt} \tag{26}$$

$$\mathrm{OPt} \rightarrow \mathrm{PtO_2} \tag{27}$$

$$\mathrm{PtO_2} + 2e^- + 4H^+ \rightarrow 2H_2O + Pt^{2+} \tag{28}$$

Place exchange is modelled as a reversible chemical reaction, not directly dependent on potential. The reaction rate expression (equation (29)) is adapted from Karan work [9]. Some terms are neglected, as in the original model a higher number of oxide species are considered.

$$r_{PE} = k_{PE}\vartheta_{PtO}(1-\vartheta_{OPt})\exp\left(-\omega_{PE} * \frac{\vartheta_{OPt}}{RT}\right) - k_{PE,r}\vartheta_{OPt} \tag{29}$$

Similarly to the PtO formation reaction rate (equation (10)), an exponential term depending on the OPt-OPt interaction energy ω_{PE} is present in the forward reaction rate, and the place-exchanged oxide formation is limited to one layer by the term $(1-\vartheta_{OPt})$.

Cathodic dissolution reaction rate (equation (30)) is adapted from Jahnke dissolution model [8]. In his work indeed, as described in 1.3, place exchange is not modelled, but indirectly considered with the cathodic dissolution, which is proportional to the PtO reduction reaction rate, and thus potential dependent.

The idea behind this semi-empirical modelling of the cathodic dissolution is that place-exchanged Pt-atoms can be considered as oxidized according to reaction (27). During decreasing potential sweeps the oxide is reduced and the place-exchanged oxide can dissolve directly in the electrolyte. In this sense, cathodic dissolution can be considered potential dependent. In other words, the Jahnke indirect formulation for PtO was adapted to the place-exchange OPt species, here included. Although the $\mathrm{PtO_2}$ oxide coverage is not calculated in the model, it can be considered equivalent the OPt oxide coverage. Indeed, at the potential conditions where place exchange takes place, the oxidation is strongly favoured, therefore reaction (27) is really fast.

$$r_{Cdiss}(r) = k_{Cdiss}\,\theta_{OPt}\exp\left(-\frac{\alpha_3 F}{RT}(\Phi - \Phi_{Cd})\right) \tag{30}$$

Anodic dissolution and oxidation reaction rates remain unchanged, while the chemical dissolution is eliminated and replaced with cathodic dissolution.

Finally, material balances are modified including the new reactions rates, and a new one for the place-exchanged oxide coverage is added, as shown below.

$$\varepsilon\frac{dc_{Pt^{2+}}}{dt} = 4\pi\sum_i {r_{Pt}^i}^2 n_{Pt}^i\left(r_{Adiss}^i + r_{Cdiss}^i\right) - \varepsilon\, q_{PtLoss} \tag{31}$$

$$\frac{d\theta_{PtO}^i}{dt} = \left(\frac{r_{Ox}^i - r_{PE}^i}{\Gamma_{max}}\right) - \left(\frac{2\theta_{PtO}^i}{r_{Pt}^i}\right)\frac{dr_{Pt}^i}{dt} \tag{32}$$

$$\frac{d\theta_{OPt}^i}{dt} = \left(\frac{r_{PE}^i - r_{Cdiss}^i}{\Gamma_{max}}\right) - \left(\frac{2\theta_{OPt}^i}{r_{Pt}^i}\right)\frac{dr_{Pt}^i}{dt} \tag{33}$$

$$\frac{dr_{Pt}^i}{dt} = -\frac{M_{Pt}}{\rho_{Pt}}\left(r_{Adiss}^i + r_{Cdiss}^i\right) \tag{34}$$

Place exchange and cathodic dissolution parameters were at first taken from Karan's and Jahnke's model, respectively.

The resulting parameters SET will be referred to as SET 2.0 (Table 17). The anodic dissolution and oxide parameters are the same of parameters SET 0.

Symbol	**Value SET 2.0**	**Unit**	
Φ_{ox}^{ref}	0,99	V	Fitted
k_{ox}	8E-10	$mol\ cm^{-2}$	Fitted
α_{a2}	0,35	-	[7]
α_{c2}	0,5	-	[7]
ω_{PtO}	26000	$J\ mol^{-1}$	Fitted
k_{dis}^{ref}	1E-9	$mol\ cm^{-2}s^{-1}$	Fitted
α_{a1}	0.5	-	Assumed
α_{c1}	0.5	-	Assumed
k_{PE}	$4.3 * 10^{-11}$	$mol\ cm^{-2}s^{-1}$	[9]
$k_{PE,r}$	$4.3 * 3 * 10^{-11}$	$mol\ cm^{-2}s^{-1}$	[9]
k_{Cdiss}	1E-13	$mol\ cm^{-2}s^{-1}$	[8]
α_{Cd}	0.5	-	Assumed
ω_{PE}	$1.3489\text{E} + 05$	$J\ mol^{-1}$	[9]
φ_{Cd}	0.75	V	[8]

Table 17 - parameters SET 2.0

5.3. Model calibration and simulation of experimental data

The model was calibrated on AST 4 experimental results, as they provide data for different potential profiles, allowing to calibrate the sensitivity of the model to different potential values.

A first attempt was made with parameters SET 2.0. The base cycle simulations of AST 4 at BoT are shown in Figure 67. The PtO is almost totally reduced during the cycling at 0.7 V, while the OPt is almost totally reduced only during the final holding. The cathodic reaction rate has really low values during the cycling, with a peak during the final holding, which is more pronounced for sample 4, gradually less marked for samples 3 and 2, and absent for sample 1. These features are in agreement with the experimental results analysis.

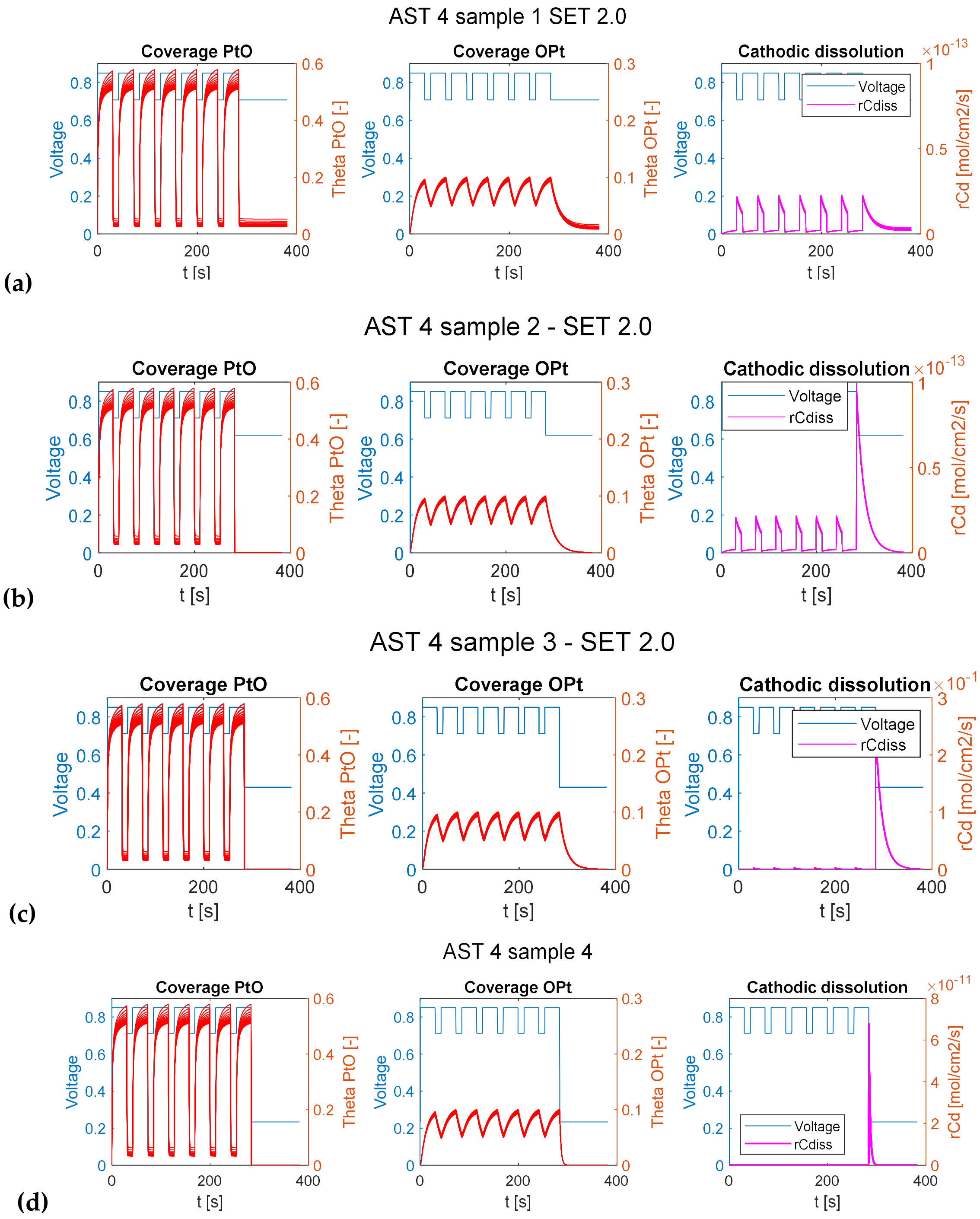

Figure 67 – AST 4 base profile for different particle groups simulated with parameters SET 2: oxide coverage, place exchange coverage and cathodic dissolution reaction rate (a) sample 1 (b) sample 2 (c) sample 3 (d) sample 4 *different y axis scale are used in the plots

The resulting ECSA trends (Figure 68) are still far from experimental results: sample 1 and sample 2 curves are really close and show a too weak degradation, while sample 3 is closer to experimental results.

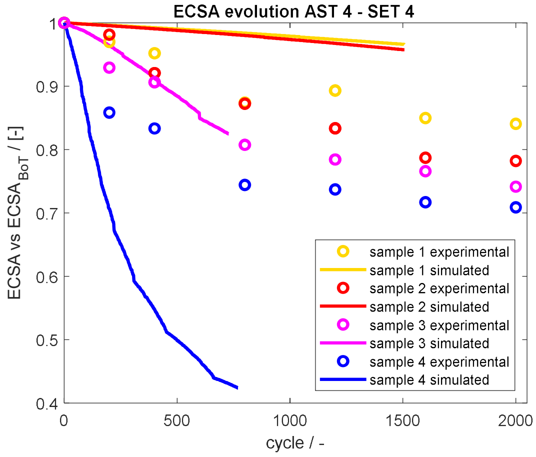

Figure 68 - ECSA evolution AST 4: experimental vs simulated data with parameters SET 2.0

Parameters when then varied. The kinetic constant of the backward place exchange $k_{PE,r}$ was then decreased to obtain an increasing OPt profile during the AST cycle, as suggested by the experimental observations. The obtained OPt profile for AST 4 sample 4 base cycle is shown in Figure 69.

The parameter α_3 was then decreased to obtain more similar degradation trends for the different samples, obtaining a new parameter SET, which will be referred to as SET 3.0 (Table 18).

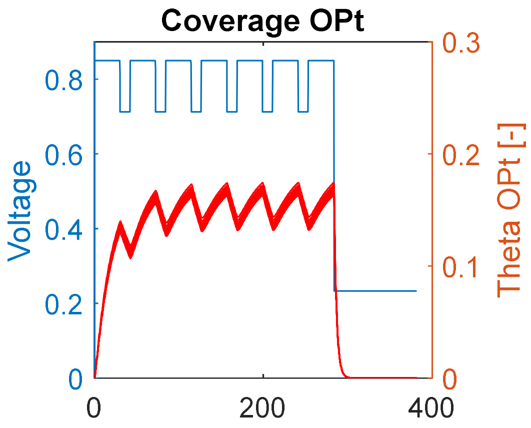

Figure 69 - OPt profile AST 4 sample 4 base cycle – SET 3.0

Symbol	Value SET 2.0	Value SET 3.0	Unit
k_{PE}	$4.3 * 10^{-11}$	$4.3 * 10^{-11}$	$mol\ cm^{-2}s^{-1}$
$k_{PE,r}$	$3 * 4.3 * 10^{-11}$	$4.3 * 10^{-11}$	$mol\ cm^{-2}s^{-1}$
k_{Cdiss}	1E-13	1E-13	$mol\ cm^{-2}s^{-1}$
α_{Cd}	0.5	0.4	-
ω_{PE}	134890	134890	$J\ mol^{-1}$
φ_{Cd}	0.75	0.75	V

Table 18 – Parameters SETS

The parameters effect was preliminarily evaluated by looking at the platinum dissolved in one AST cycle, analysing the different contribution given by the anodic dissolution, the cathodic dissolution during the cycling, and the cathodic dissolution during the final holding. The dissolved platinum was calculated by integrating reaction rates for each particle group and by summing them for the two considered reactions. These quantities are shown in Figure 70 for the four samples, identified by the final holding potential, as obtained with parameters SET 2.0 and 3.0.

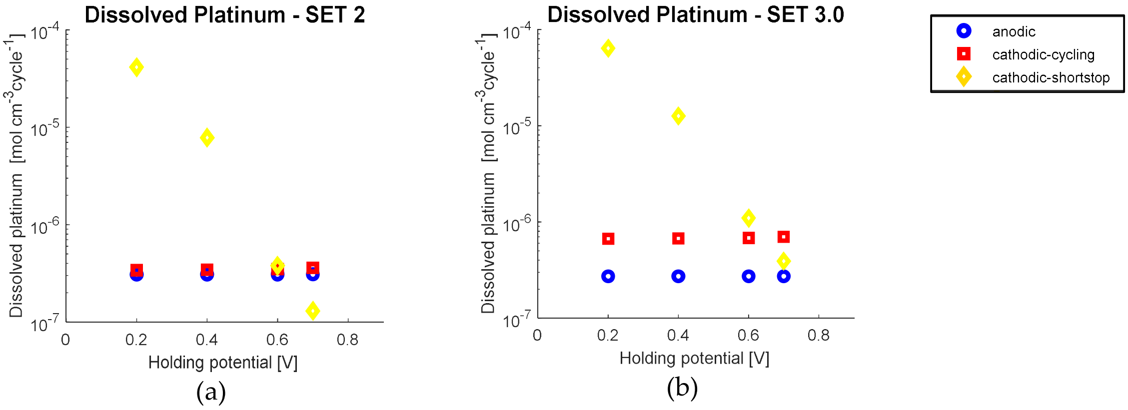

Figure 70 - Platinum dissolved during AST 4 base cycle: (a) parameters SET 2.0 (b) parameters SET 3.0

A sensitivity analysis was then performed varying α_3 and the kinetic constant k_{Cdiss}, as shown in Table 19.

	Value SET 3.0	**Value SET 3.1**	**Value SET 3.2**	**Value SET 3.3**	**Value SET 3.4**	**Value SET 3.5**	**Value SET 4**	**Unit**
k_{PE}	$4.3 * 10^{-11}$	$4.3 * 10^{-11}$	$4.3 * 10^{-11}$	$4.3 * 10^{-11}$	$4.3 * 10^{-11}$	$4.3 * 10^{-11}$	$4.3 * 10^{-11}$	$\frac{mol}{cm^2 s}$
$k_{PE,r}$	$4.3 * 10^{-11}$	$4.3 * 10^{-11}$	$4.3 * 10^{-11}$	$4.3 * 10^{-11}$	$4.3 * 10^{-11}$	$4.3 * 10^{-11}$	$4.3 * 10^{-11}$	$\frac{mol}{cm^2 s}$
k_{Cdiss}	1E-13	**3E-14**	**1E-14**	3E-14	3E-14	3E-14	**5E-14**	$\frac{mol}{cm^2 s}$
α_{Cd}	0.4	0.4	0.4	**0.3**	**0.5**	**0.2**	**0.25**	**-**
ω_{PE}	134890	134890	134890	134890	134890	134890	134890	$J\ mol^{-1}$
φ_{Cd}	0.75	0.75	0.75	0.75	0.75	0.75	0.75	V

Table 19 - parameters SETS tested in the sensitivity analysis

The dissolved platinum with the different parameters SETs tested in the sensitivity analysis is shown in Figure 71, and the obtained ECSA trends in Figure 72.

For increasing values of α_3, the effect of different holding potential values is strengthened, resulting in a more marked difference among dissolved platinum of different samples and consequently more distant ECSA curves.

For increasing value of k_{Cdiss} a higher degradation is obtained, with a stronger impact on samples 3 and 4. For these samples cathodic dissolution is expected to be more significant indeed.

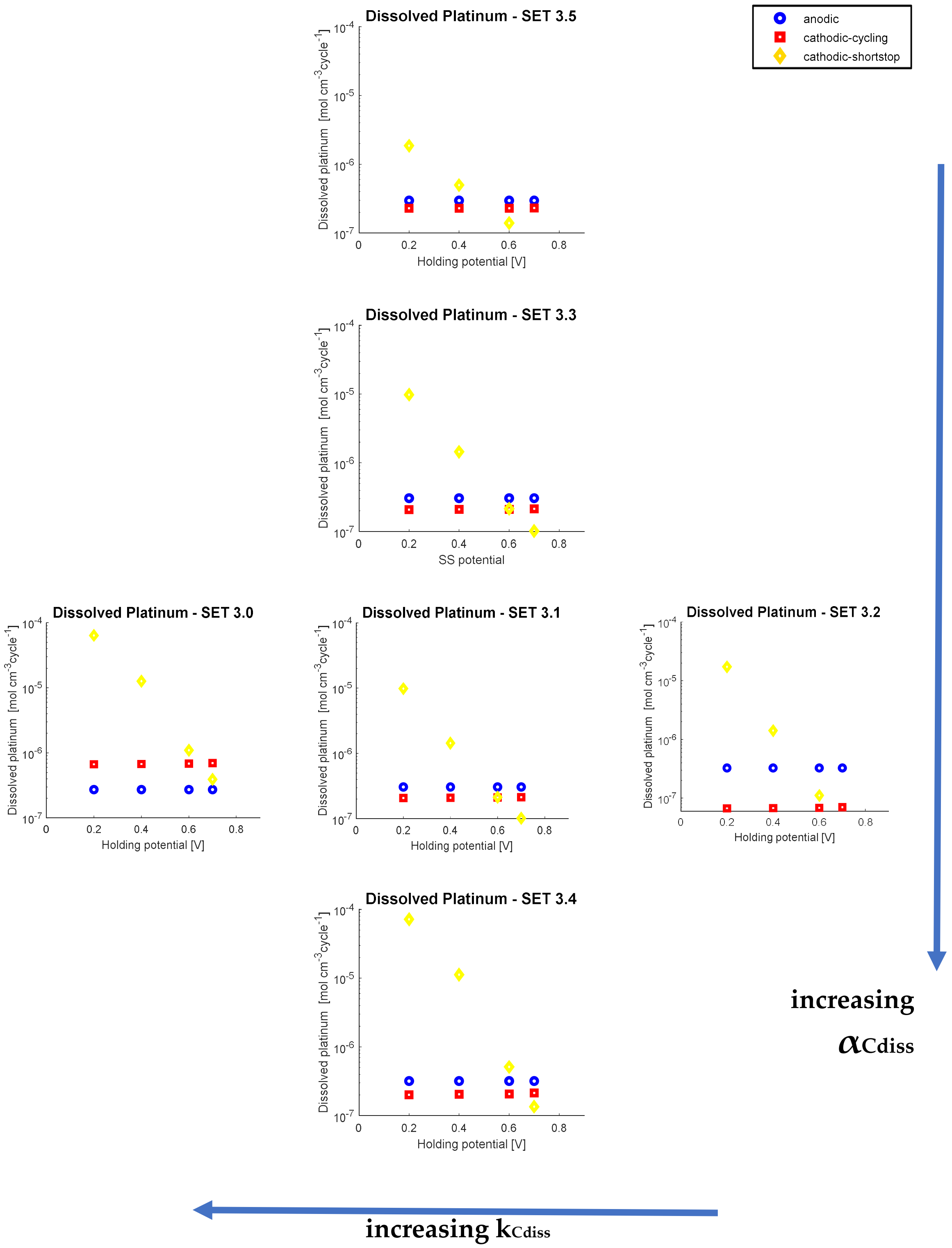

Figure 71 – Sensitivity analysis: Platinum dissolved during AST 4 base cycle simulated with different parameters SETS

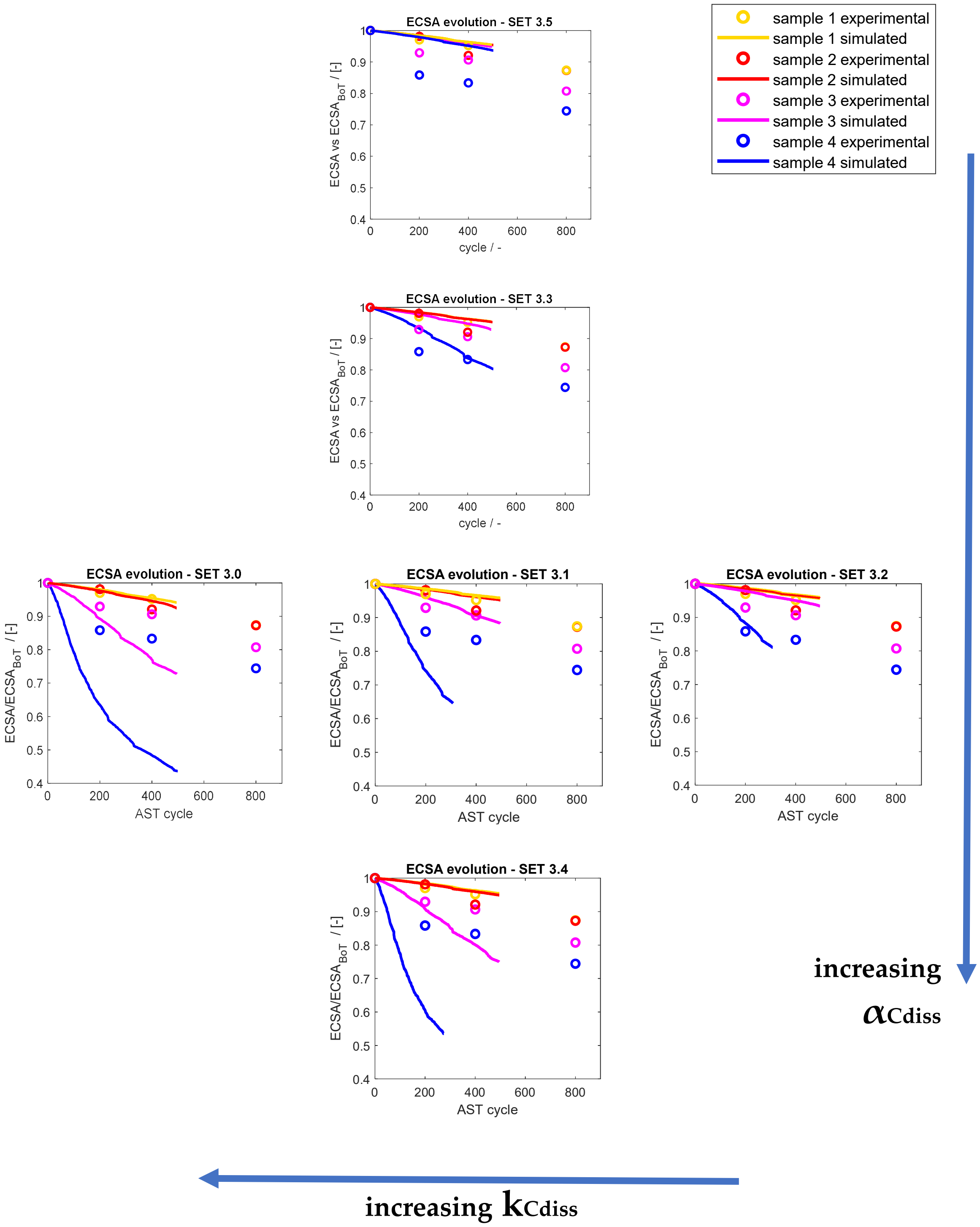

Figure 72 – Sensitivity analysis: AST 4 ECSA trends experimental vs simulated data with different parameters SETS

A new parameters set (SET 4 Table 19) was defined thanks to the sensitivity analysis, and AST 4 was simulated. The PtO base profile (Figure 75) remain unchanged, the OPt shows a slightly increasing trend during the cycling and is differently reduced in the four samples during the holding, although the difference is limited. Cathodic dissolution reaction rate has the same pattern obtained in the previous simulation (really low values during the cycling, with a peak during the final holding).

The dissolved platinum is shown in Figure 73, compared with the quantities obtained with the previous parameters (SET 2.0). With the new parametrization the dissolved platinum has more similar value among the different samples.

Consequently, the obtained ECSA trends (Figure 74) show a better correspondence with experimental results.

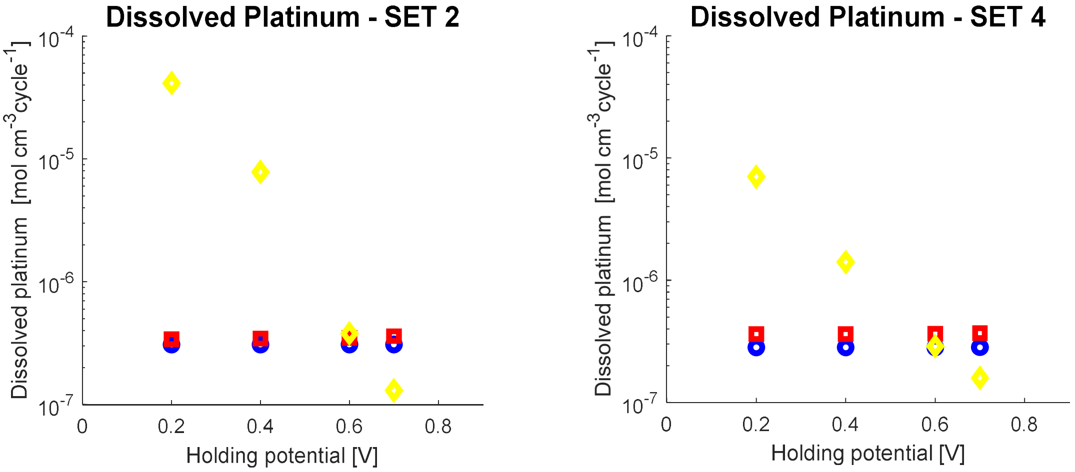

Figure 73 - Platinum dissolved during AST 4 base cycle simulated with parameters SET 2 and SET 4

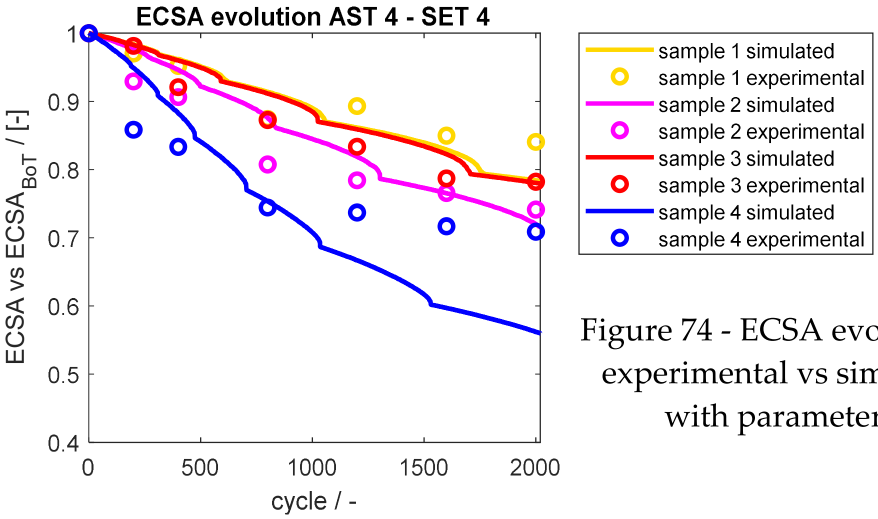

Figure 74 - ECSA evolution AST 4: experimental vs simulated data with parameters SET 4

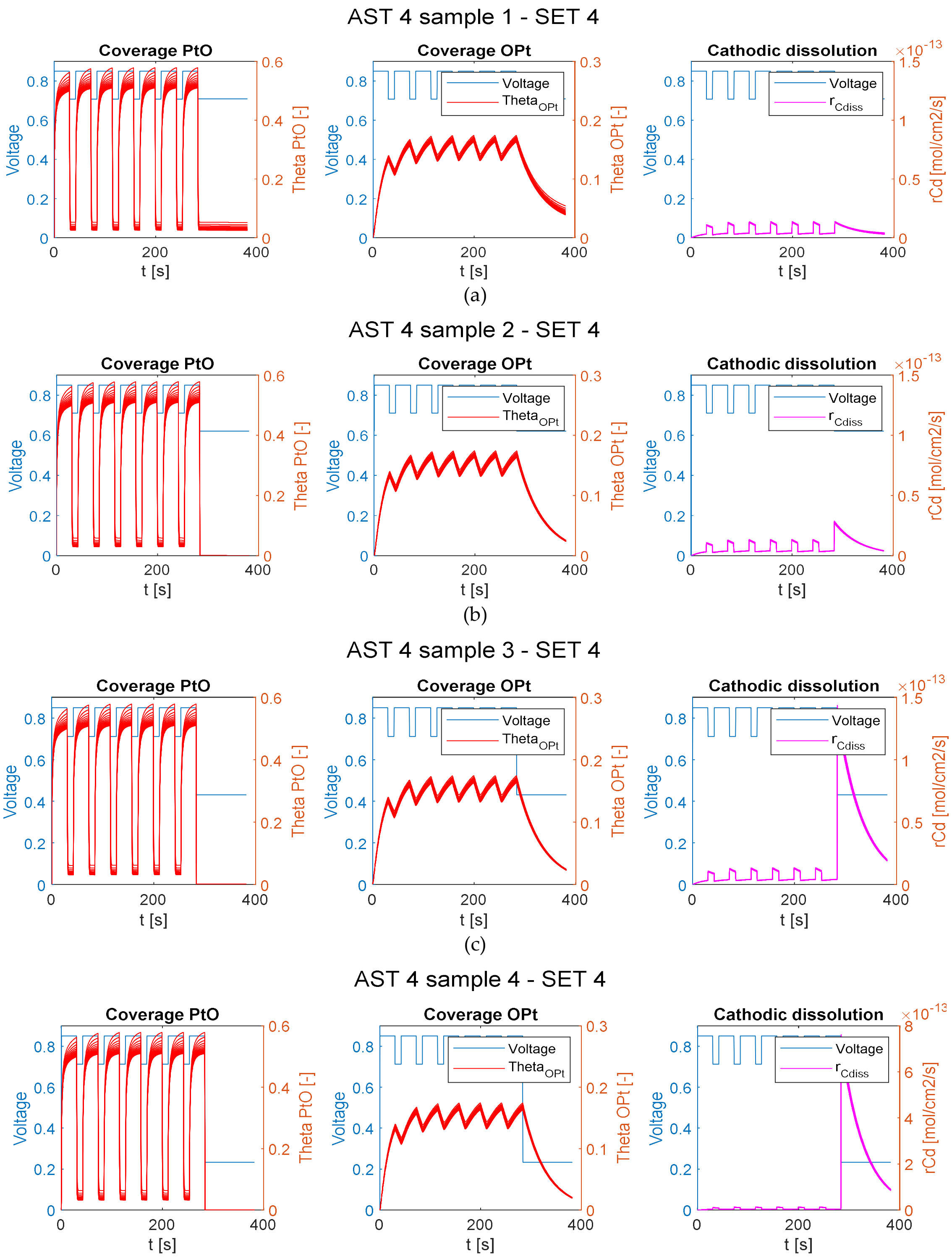

(a)

(b)

(c)

(d)

Figure 75 – AST 4 base profile for different particle groups simulated with parameters SET 4: oxide coverage, place exchange coverage and cathodic dissolution reaction rate (a) sample 1 (b) sample 2 (c) sample 3 (d) sample 4

*different y axis scale are used in the plots

AST 1 and AST 3 were also simulated with these parameters.

In AST 3 base cycle simulation (Figure 77), the place-exchanged oxide is only partially reduced during the cycling, also going down to 0.4 V (sample 3), in agreement with experimental results. It is worth underlining that in AST 4 sample 3 simulation, OPt is almost totally reduced during the final holding at the same potential (0.4 V). According to the model, the oxide is slowly reduced and the same potential value can induce different effect depending on the dwell time. A further experimental analysis would be necessary to indagate this hypothesis and check whether this model features matches with the real oxide behaviour.

The cathodic dissolution has low values for sample 1 and sample 2, having similar reaction rate profiles (Figure 77 a and b), while its impact is more significative for sample 3. This results in similar ECSA trends for the first two samples (Figure *76*). However, the overall ECSA trends match quite well with the experimental ones.

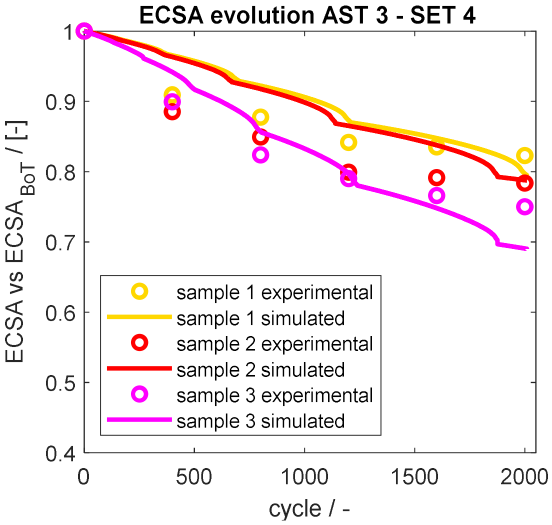

Figure *76* – ECSA evolution AST 3: experimental vs simulated data with parameters SET 4

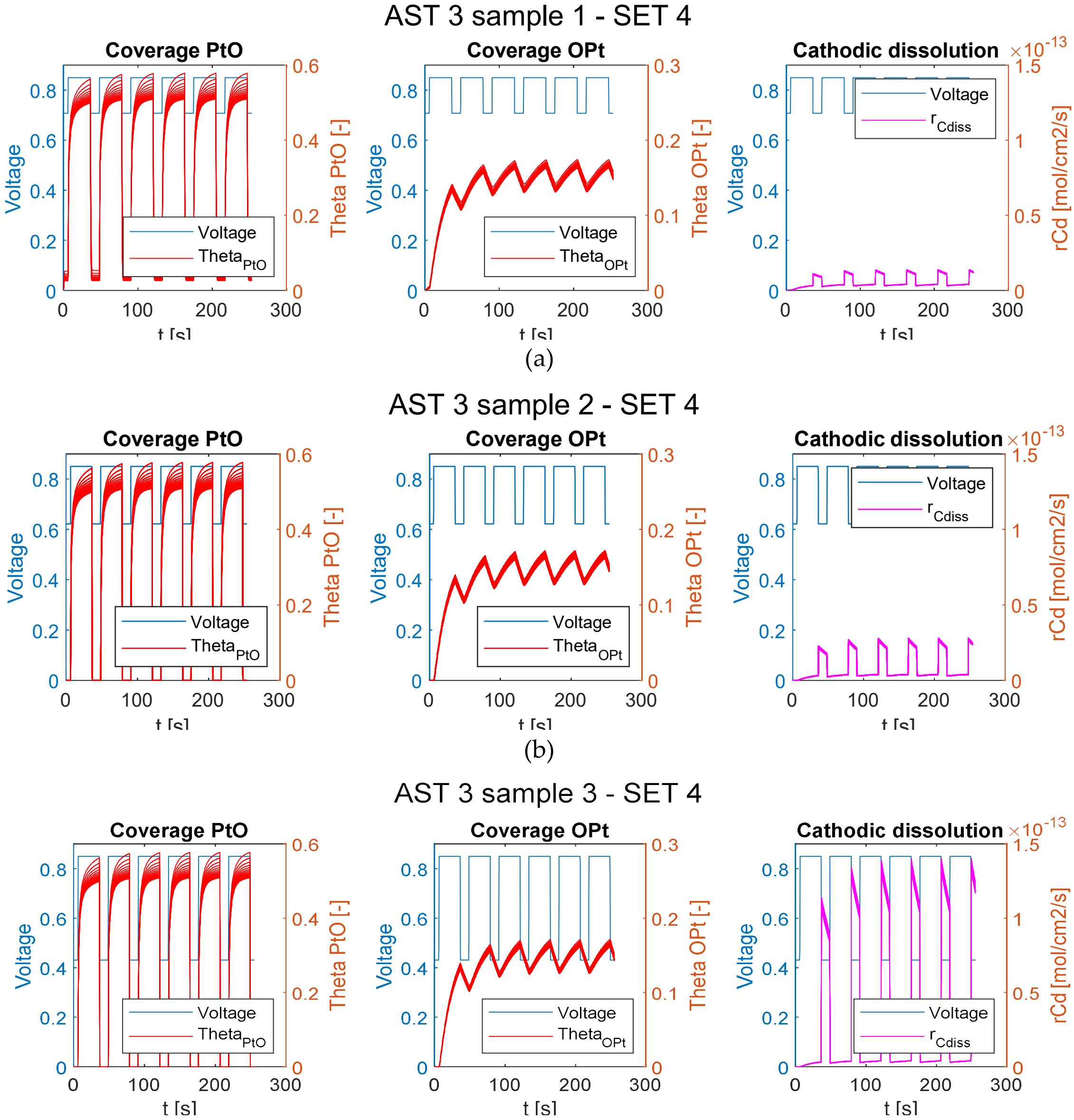

(a)

(b)

(c)

Figure 77 – AST 3 base profile for different particle groups simulated with parameters SET 4: oxide coverage, place exchange coverage and cathodic dissolution reaction rate (a) sample 1 (b) sample 2 (c) sample 3

*different y axis scale are used in the plots

AST 1 base cycle simulation is shown in Figure 78. PtO oxide coverage (Figure 78 a, b) reaches higher values for sample 2, which has a higher UPL (0.9 V). The anodic dissolution reaction rate is higher for sample 1. OPt shows a slightly increasing trend during the cycling and is reduced during the short stop, resulting in a strong cathodic dissolution peak. In the base profile of sample 2 the OPt reaches higher values, but the cathodic dissolution reaction rates are really similar.

The dissolved platinum due to anodic and cathodic dissolution is shown in Figure 79 for the two samples, identified by their UPL [sample 1 0.85 V, sample 2 0.9V]. Anodic dissolution has a higher impact on sample 1, while the cathodic dissolution, which is much higher is weakly influenced by the UPL. This results in similar ECSA trends for the two samples (Figure 80).

This result is different from the one obtained by simulating AST 4 with the model in its first version (Figure 54), where the two samples show significantly different ECSA trends. From this point of view, the last simulation better matches experimental results. It seems that UPL has a minor effect when cathodic dissolution has a prevailing role, while it is more significative when anodic dissolution is the predominant mechanism (as in the first version of the model).

This could explain the inconsistency of the experimental results with the literature with regard to the UPL effect. Indeed, the voltage profile previously used in the literature [16] to investigate the UPL effect are based on the DOE electrocatalyst AST described in section 3.5, whose voltage profile has really low dwell times (3 s) and does not include short stops. In these conditions, place exchange and cathodic dissolution are not enhanced, therefore the degradation is mainly due to anodic dissolution and a higher UPL has a stronger degrading effect. On the contrary, ASTs designed in this work have longer dwell times and short stops. These features, which better resemble what happens in real stacks, enhance place exchange and cathodic dissolution, and strongly reduce the effect of the UPL.

Anyway, both trends (Figure 80) show a higher degradation with respect to experimental results, evincing the necessity of a better calibration that could be based on a larger set of experimental data that will be taken in a future development of the work.

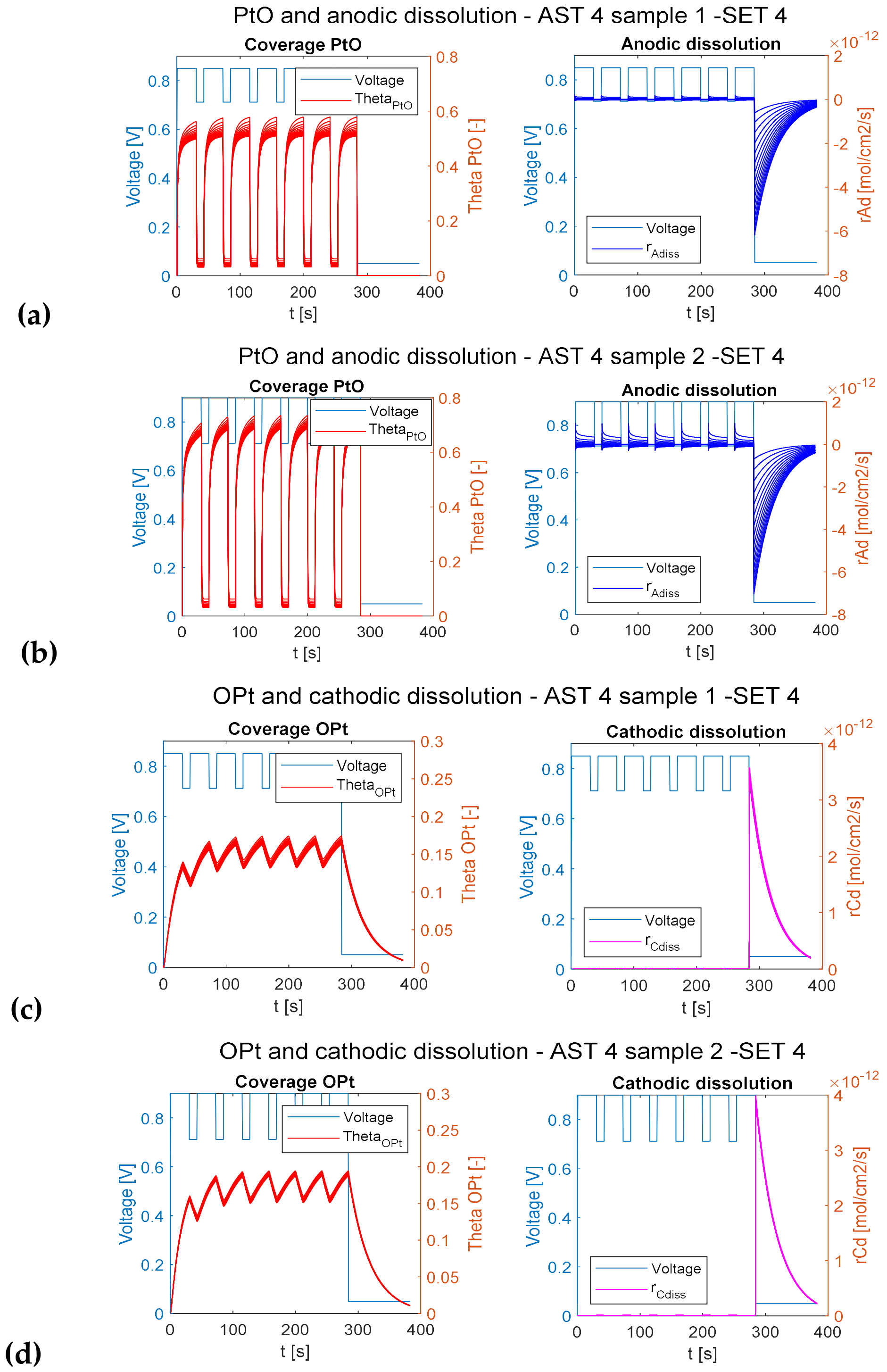

Figure 78 – AST 1 base profile for different particle groups simulated with SET 4:
(a) sample 1 PtO oxide coverage and anodic dissolution reaction rate
(b) sample 2 PtO oxide coverage and anodic dissolution reaction rate
(c) sample 1 OPt oxide coverage and cathodic dissolution reaction rate
(d) sample 2 OPt oxide coverage and cathodic dissolution reaction rate

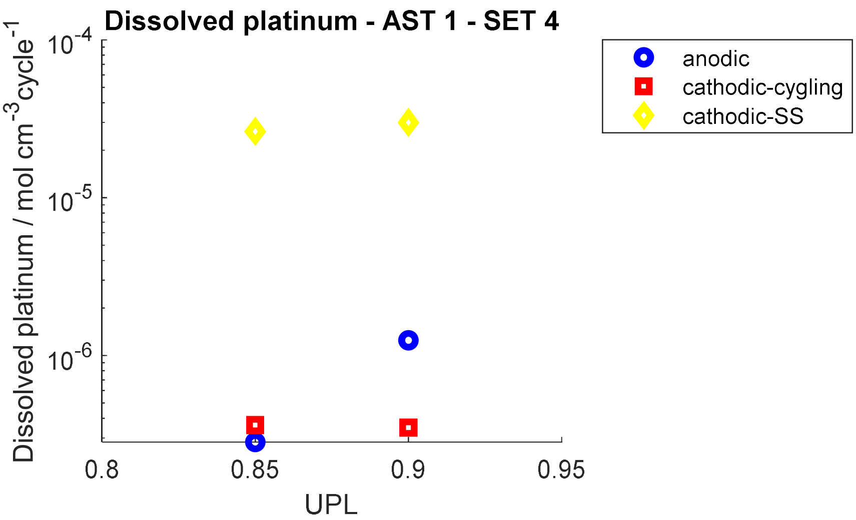

Figure 79 - Platinum dissolved during AST 1 base cycle simulated with parameters SET 4 [the two samples are identified by their UPL: sample 1 0.85 V, sample 2 0.9 V]

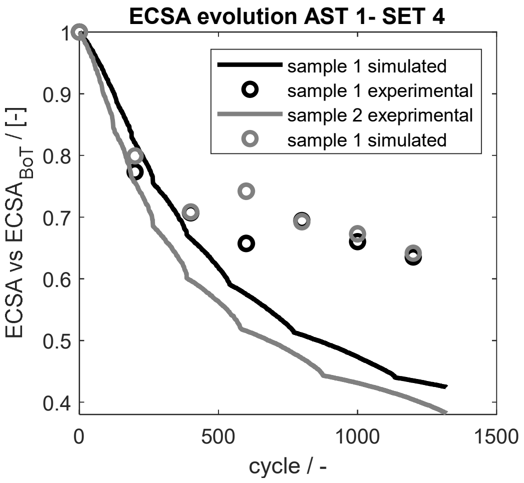

Figure 80 - ECSA evolution AST 1: experimental vs simulated data with parameters SET 4

With respect to previous attempts, AST 3 and AST 4 simulated ECSA trends show a better agreement with experimental results. AST 1 ECSA trends, although overestimating the degradation, are more similar which agrees with experimental results. This improved correspondence with experimental data suggests that cathodic dissolution have a prevailing effect in realistic degradation, which is reproduced with ASTs.

Nonetheless, the improvement in the model does not allow to exactly reproduce the actual effect of potential. Indeed, the potential value weakly affects the degradation in the range between 0.85 V and 0.6 V (resulting in similar trends for samples 1 and 2 of AST 3 and sample 1 and 2 of AST 4 respectively), while it has a gradually stronger impact going toward lower values. Approaching 0 V the potential effect is too strong with respect to experimental results of AST 1.

Moreover, the simulated ECSA are characterized by an almost linear evolution. Trends stabilize only when a really strong degradation takes place (i.e. in AST 1 simulation), while experimental results show a stabilization also for limited ECSA loss.

The model could be further improved by stressing the effect of particle size on the degradation with the introduction of a dependence of the cathodic dissolution on the particle radius. From a physical point of view this could be consistent with a structure dependent description of the cathodic dissolution, i.e. leading to irreversible place exchange on the edge sites of the nanoparticle.

This would result in a stronger initial degradation due to the strong dissolution of smaller particles and a progressive stabilization when the PRD is shifted toward higher radius.

AST Electrocatalyst simulation

Finally, electrocatalyst AST was simulated again with the developed model, also including place exchange and cathodic dissolution. The two ECSA trends (Figure 81) are quite similar, suggesting that cathodic dissolution has a limited impact on this voltage profile.

Indeed, AST electrocatalyst voltage profile does not enhance cathodic dissolution, as it is characterized by low dwell times (3 s), which do not promote place exchange, and the potential is never reduced below 0.6 V, which do not promote OPt dissolution. The OPt profile and the cathodic dissolution during the first 20 cycles are shown in Figure 82: the oxide grows slowly and stabilizes around a coverage of 0.14, lower than the one of AST 3 and AST 4 simulation (around 0.18). Most importantly, cathodic dissolution is really low: its value is comparable with those of AST 3 and AST 4 sample 1 simulations (Figure 75 and Figure 77).

The ASTs performed in the experimental analysis, on the contrary, are characterized by longer dwell times (12 s and 30), which better reproduce the real automotive operation, and by a wider potential range. With this type of voltage profiles, OPt coverage reaches higher values and the cathodic dissolution effect is more evident.

The model in its first version was indeed not able to reproduce the experimental results of these ASTs, while a better correspondence was obtained by considering also place exchange and cathodic dissolution.

These observations suggest that electrocatalyst AST is not a suitable test to investigate the cathodic dissolution role in real degradation. Different voltage profiles, with longer dwell times and periodic potential reduction are more appropriate.

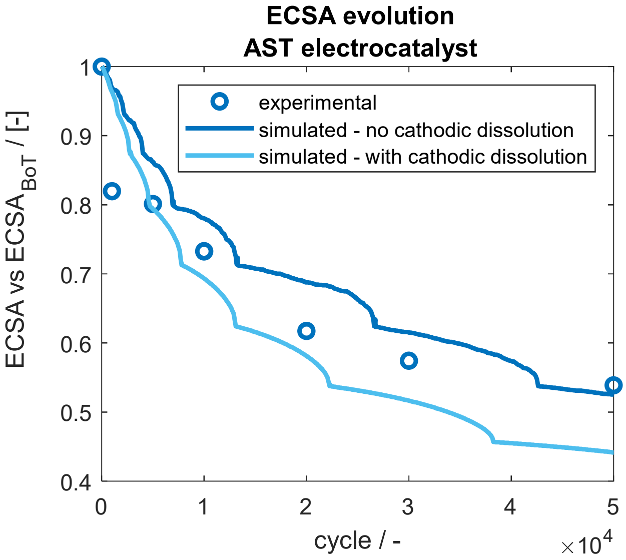

Figure 81 - ECSA evolution AST 1 experimental vs simulated data with SET 0 and SET 4

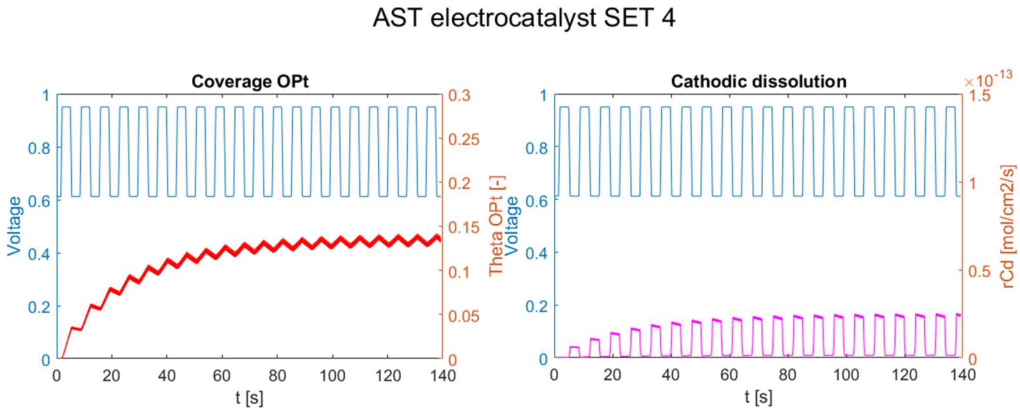

Figure 82 - AST electrocatalyst - OPt profile and cathodic dissolution in the first 20 cycles

5.4. Conclusion

Place exchange and cathodic dissolution allow to explain some of the experimental results. Current trends can be justified by the presence of place-exchanged oxides, more resistant than the PtO, which are accumulated during the cycling above 0.7 V and totally reduced only going to lower potential values. The strong degrading effect of the short stops, as well as the different degradation of AST 4 samples are also explained: OPt is accumulated during the cycling and totally dissolved when going to low potential values. For lower holding potential values a stronger dissolution takes place, causing a stronger degradation. From the experimental current trends, it emerges that the oxide is not completely reduced at 0.4 V. Considering the strong ageing effect associated to short stops, it can be hypothesized that the oxide is further reduced below 0.1 V.

Place exchange and cathodic dissolution reaction rate were taken from Karan's [9] and Jahnke's [8] model respectively, and the parameters were calibrated by means of a sensitivity analysis. The model is now able to reproduce the different effect due to different potential profiles: AST 3 and AST 4 simulated ECSA trends show a better agreement with experimental results. The shortstop effect is now reproduced, although it is overestimated: AST 1 simulation results in a higher degradation than the one experimentally observed. Moreover, the effect of the different maximum potential in AST 1 profiles is limited, in agreement with experimental results.

The electrocatalyst AST was simulated again with the developed model, resulting in an ECSA trend which is similar to the one previously obtained. This suggests that this type of AST is not suitable to investigate the cathodic dissolution role in real degradation.

6 Conclusion and future developments

A 0-D model has been developed to simulate platinum dissolution in normal operating conditions, given different voltage profiles. The model in its first version includes only one oxide (PtO) and one dissolution reaction (i.e. anodic dissolution). Parameters were calibrated on experimental data.

An experimental analysis was made, by performing several ASTs in hydrogen/air with different potential profiles. It emerged that a square wave potential profile ranging between 0.7 V and 0.85 V has a low impact on degradation (17% ECSA loss after 1500 equivalent operating hours), while a stronger degradation is obtained when decreasing the minimum potential value. A preliminary analysis elucidated the minor role of maximum potential (when minimum value is kept higher than 0.7 V), and a limited impact when applying a potentiostatic profile instead of a galvanostatic one. Also the variation of the relative humidity (at values > 60%) did not result in significantly different losses. The strongest degradation was observed when alternating a square wave potential profile ranging between 0.7 V and 0.85 V with periodic potential reductions to nearly 0 V, resembling a short stop. The ECSA trend drops below 80% during the first 150 equivalent operating hours, and then stabilizes around 65%.

The currents trends detected during the ageing tests suggest the presence of an oxide which is not completely reduced at 0.7 V but only going toward lower potential values. It can be hypothesized that the oxide is further reduced with the short stops when the electrode potential goes down below 0.1 V.

The model in its first version is not able to reproduce the experimental results. Indeed, with one oxide (PtO) which is totally reduced at 0.7 V it is not possible to reproduce the oxide profiles which would justify the observed current trends, since the oxygen reduction reaction taking place in the electrode is expected proportional to the available Pt surface area (i.e. not covered by oxides). The ECSA trends obtained by simulating the different ASTs potential profiles are almost identical: indeed, anodic dissolution is promoted at high potential thus it becomes relevant at voltage > 0.7 V. The degrading effect of short stop is not reproduced at all.

The model was thus improved by adding the place exchange mechanism and the cathodic dissolution reaction, which could provide a better explanation of experimental results. Some parameters of these reactions were taken from the literature, while others were calibrated on experimental data by means of a sensitivity analysis.

The model in its second version is able to reproduce the different ECSA loss that is observed by changing the lower potential values, indicating that the cathodic dissolution mechanism that was hypothesized is consistent with the observed degradation rate and further understanding of this mechanism is needed. The shortstop effect is also reproduced, although it is overestimated.

Considering the experimental observations, together with the analysis performed with the aid of the model, it seems that the formation of a more resistant oxide (modelled with place exchange) and the cathodic dissolution play an important role in degradation in realistic operating conditions (i.e. under hydrogen/air operation and sufficiently long holding times at high voltage). This effect cannot be observed by performing the standard D.o.E. electrocatalyst AST, as it has a potential profile which does not enhance cathodic dissolution (i.e. short holding times and more frequent potential transient, at potentials > 0.6 V).

Further improvement could be implemented in the model, i.e. a radius-dependent formulation of cathodic dissolution which could explain the stabilization of ECSA trends. Indeed, it could be reasonably assumed that size and geometry of the particles impact on the dissolution rate, making larger particles less prone.

List of figures

List of tables

Acronyms

AST	Accelerated Stress Test
BOT	Beginning Of Test
CCM	Catalyst Coated Membrane
CL	Catalyst layer
CV	Cyclic Voltammetry
DOE	U.S. Department of energy
ECSA	ElectroChemical Surface Area
EIS	Electochemical Impedance Spectroscopy
GDL	Gas Diffusion Layer
HFR	High Frequency Resistance
HOR	Hydrogen Oxidation Reaction
HP	Holding Potential
IDFAST	Investigations on Degradation mechanisms and Definition of protocols for PEM Fuel cells Accelerated Stress Testing
LPL	Lower Potential Limit
LSV	Linear Sweep Voltammetry
MEA	Membrane Electrode Assembly
OCV	Open Circuit Voltage
ORR	Oxygen Reduction Reaction

PEMFC	Polimer Electrolyte Membrane Fuel Cell
PRD	Particle Radius Distribution
RCL	Catalyst Layer Resistance
RH	Relative humidity
TEM	Transmission Electron Microscopy
UPL	Upper Potential Limit

Nomenclature

a_w	Water activity
$c_{H^+,ref}$	Platinum reference concentration
c_{H^+}	Hydrogen concentration
$c_{Pt^{2+},ref}$	Hydrogen reference concentration
$c_{Pt^{2+}}$	Platinum concentration
D_{diff}	Diffusion coefficient
D_o	Reference diffusion coefficient
EW	Ionomer equivalent weight
F	Faraday constant
h_{CL}	Catalyst layer thickness
k_{Adis}	Anodic dissolution kinetic constant
k_{chem}	Chemical dissolution kinetic constant
k_{dis}^{ref}	Reference anodic dissolution kinetic constant
k_{ox}	Oxidation kinetic constant
$k_{PE,r}$	Backward place exchange kinetic constant
k_{PE}	Place exchange kinetic constant
L_x	Diffusion length
M_{H_2O}	Water molecular weight
M_{Pt}	Platinum molecular weight

M_{PtO}	Platinum molecular weight
n	Number of electrons
n_{Pt}^{i}	Particles number
q_{Ptloss}	Platinum diffusive flux
r_{Adis}	Anodic dissolution reaction rate
r_{Cdis}	Cathodic dissolution reaction rate
r_{chem}	Chemical dissolution reaction rate
r	Particle radius
R	Gas constant
RH	Relative humidity
RH_0	Reference relative humidity
r_{Ox}	Oxidation reaction rate
r_{PE}	Place exchange reaction rate
T_0	Reference temperature
T	Temperature
α	transfer coefficient
Γ_{max}	Moles of active sites per unit of platinum area
$\Delta\mu_{Pt}$	Platinum chemical potential
$\Delta\mu_{PtO}$	Platinum oxide chemical potential
$\Delta\mu_{PtO}^{ref}$	Platinum oxide reference chemical potential

θ_{PtO}	Oxide coverage
θ_{OPt}	Place-exchanged oxide coverage
ε	Electrode porosity
ϑ	Fitting parameter RH
λ	amount of water molecules per acid group
$\rho_{\mathrm{H_2O}}$	Water density
ρ_{Nafion}	Nafion density
ρ_{Pt}	Platinum density
ρ_{PtO}	Platinum oxide density
σ_{Pt}	Platinum surface tension
σ_{PtO}	Platinum oxide surface tension
Φ	Potential
Φ_{Cd}	Cathodic dissolution reference potential
Φ_{dis}	Oxidation equilibrium potential
Φ_{dis}	Anodic dissolution equilibrium potential
$\Phi_{\mathrm{diss}}^{\mathrm{ref}}$	Reference anodic dissolution equilibrium potential
$\Phi_{\mathrm{ox}}^{\mathrm{ref}}$	Reference oxidation equilibrium potential
ω_{PE}	OPt-OPt interaction energy
ω_{PtO}	PtO-PtO interaction energy

Bibliography

[1] “index @ www.id-fast.eu.” .

[2] E. Padgett and S. Satyapal, “DOE Hydrogen Program Record,” no. Dm, pp. 1–6, 2021.

[3] H. A. Baroody, E. Kjeang, J. E. Soc, H. A. Baroody, and E. Kjeang, “Predicting Platinum Dissolution and Performance Degradation under Drive Cycle Operation of Polymer Electrolyte Fuel Cells Predicting Platinum Dissolution and Performance Degradation under Drive Cycle Operation of Polymer Electrolyte Fuel Cells,” 2021.

[4] A. A. Topalov, S. Cherevko, A. R. Zeradjanin, J. C. Meier, I. Katsounaros, and K. J. J. Mayrhofer, “Towards a comprehensive understanding of platinum dissolution in acidic media,” *Chem. Sci.*, vol. 5, no. 2, pp. 631–638, 2014.

[5] R. K. Ahluwalia *et al.*, “Potential Dependence of Pt and Co Dissolution from Platinum-Cobalt Alloy PEFC Catalysts Using Time-Resolved Measurements JES F OCUS I SSUE ON P ROTON E XCHANGE M EMBRANE F UEL C ELL (PEMFC) D URABILITY Potential Dependence of Pt and Co Dissolution from ,” 2018.

[6] R. M. Darling and J. P. Meyers, “Kinetic Model of Platinum Dissolution in PEMFCs,” *J. Electrochem. Soc.*, vol. 150, no. 11, p. A1523, 2003.

[7] P. Schneider, C. Sadeler, A.-C. Scherzer, N. Zamel, and D. Gerteisen, “Fast and Reliable State-of-Health Model of a PEM Cathode Catalyst Layer,” *J. Electrochem. Soc.*, vol. 166, no. 4, pp. F322–F333, 2019.

[8] T. Jahnke, A. Baricci, C. Rabissi, and A. Casalegno, “ Erratum: Physical Modeling of Catalyst Degradation in Low Temperature Fuel Cells: Platinum Oxidation, Dissolution, Particle Growth and Platinum Band Formation [J. Electrochem. Soc. , 167 , 013523 (2020)] ,” *J. Electrochem. Soc.*, vol. 167, no. 14, p. 149001, 2020.

[9] B. Jayasankar and K. Karan, “O2 electrochemistry on Pt: A unified multi-step model for oxygen reduction and oxide growth,” *Electrochim. Acta*, vol. 273, pp. 367–378, 2018.

[10] A. Kongkanand and J. M. Ziegelbauer, “Surface Platinum Electrooxidation in the Presence of Oxygen,” 2012.

[11] D. Mora, “Design and validation of new Accelerated Stress Tests for the experimental analysis of hydrogen PEM fuel cell degradation under real world automotive operation,” 2022.

[12] Kevin .R. Cooper, “Fuel Cell Magazine |,” pp. 1–2, 2008.

[13] M. Zhiani, S. Majidi, V. B. Silva, and H. Gharibi, “Comparison of the performance and EIS (electrochemical impedance spectroscopy) response of an activated PEMFC (proton exchange membrane fuel cell) under low and high thermal and pressure stresses,” *Energy*, vol. 97, pp. 560–567, 2016.

[14] R. Vetter and J. O. Schumacher, “Free open reference implementation of a two-phase PEM fuel cell,” *Comput. Phys. Commun.*, vol. 234, pp. 223–234, 2019.

[15] T. F. Cells, F. Cell, T. Office, F. Cells, T. Office, and T. F. Cells, “3.4 Fuel Cells,” vol. 2015, pp. 1–58, 2016.

[16] A. Kneer and N. Wagner, “A Semi-Empirical Catalyst Degradation Model Based on Voltage Cycling under Automotive Operating Conditions in PEM Fuel Cells,” *J. Electrochem. Soc.*, vol. 166, no. 2, pp. F120–F127, 2019.

[17] K. Shinohara, A. Ohma, A. Iiyama, T. Yoshida, and A. Daimaru, “Membrane and Catalyst Performance Targets for Automotive Fuel Cells by FCCJ Membrane, Catalyst, MEA WG,” *ECS Meet. Abstr.*, vol. MA2011-02, no. 16, pp. 1103–1103, 2011.

[18] P. Zihrul, I. Hartung, S. Kirsch, G. Huebner, F. Hasché, and H. A. Gasteiger, “ Voltage Cycling Induced Losses in Electrochemically Active Surface Area and in H 2 /Air-Performance of PEM Fuel Cells ,” *J. Electrochem. Soc.*, vol. 163, no. 6, pp. F492–F498, 2016.

Acknowledgments

This work has been developed in the framework of the European ID-FAST project, which has received funding from the Fuel Cells and Hydrogen 2 Joint Undertaking under the European Union’s Horizon 2020 research and innovation program (grant agreement No. 779565).